EIC Detector R&D Progress Report

The EIC Tracking and PID Consortium
(eRD6 Consortium)

March 6, 2021

The eRD6 Consortium

Project ID: eRD6

Project Name: Tracking & PID detector R&D towards an EIC detector

Period Reported: from July 2020 to March 2021

Brookhaven National Lab (BNL): Craig Woody

Florida Institute of Technology (Florida Tech): Marcus Hohlmann

INFN Trieste: Silvia Dalla Torre

CEA Saclay: Francesco Bossù, Maxence Vandenbroucke

Stony Brook University (SBU): Klaus Dehmelt, Thomas Hemmick

Temple University (TU): Matt Posik, Bernd Surrow

University of Virginia (UVa): Kondo Gnanvo, Nilanga Liyanage

Vanderbilt University: Julia Velkovska, Vicki Greene, Sourav Tarafdar

Yale University: Richard Majka*, Nikolai Smirnov

Project Members:

BNL: B. Azmoun, A. Kiselev, J. Kuczewski, M. L. Purschke, C. Woody

Fl. Tech: J. Collins, J. Hadley, M. Hohlmann, M. Lavinsky

INFN Trieste: S. Dalla Torre, S. Levorato, F. Tessarotto

CEA Saclay: Stephane Aune, Francesco Bossù, Aude Glaenzer, Maxence Revolle, Franck Sabatié, Maxence Vandenbroucke

SBU: K. Dehmelt, A. Deshpande. P. Garg, T. K. Hemmick, S. Park, V. Zakharov, A. Zhang

TU: N. Lukow, M. Posik, A. Quintero, B. Surrow

UVa: K. Gnanvo, N. Liyanage

Yale University: R. Majka*, N. Smirnov

Vanderbilt University: Julia Velkovska, Sourav Tarafdar, Vicki Greene

* deceased

Contact Person: Kondo Gnanvo; kgnanvo@virginia.edu

Contents

1 Introduction **7**

1.1 Brief overview of eRD6 project histories . . . 7

1.2 eRD6 Contribution to EIC Yellow Report Effort . . . 7

1.3 Summary Page: Barrel Tracker with TPC . . . 8

1.3.1 Accomplishments to date . . . 8

1.3.2 Technological readiness . . . 8

1.3.3 Work remaining for a TDR . . . 9

1.3.4 Cost estimate and timeline . . . 9

1.4 Summary Page: Barrel Tracker with Cylindrical Micromegas . . . 10

1.5 Summary Page: Fast Tracking Layer with Cylindrical μRWELL . . . 11

1.6 Summary Page: Endcap Trackers with MPGDs . . . 12

1.7 Summary Page: Development of MPGDs for High Momentum Hadron PID . . . 13

1.7.1 Development of MPGD sensors of single photons . . . 13

1.7.2 New Photocathode Materials for gaseous detector . . . 13

1.8 Summary Page: New Radiator Materials for PID . . . 15

1.9 Summary Page: Large Mirror Development . . . 15

2 Barrel Tracker with TPC **16**

2.1 What was planned for this period? . . . 16

2.1.1 TPC studies at Brookhaven National Lab and Yale Univ. . . . 16

2.1.2 TPC studies at Stony Brook . . . 16

2.1.3 TPC studies at Vanderbilt U. . . . 16

2.2 What was achieved? . . . 17

2.2.1 TPC studies at Brookhaven National Lab and Yale Univ. . . . 17

2.2.2 TPC studies at Stony Brook . . . 25

2.2.3 TPC studies at Vanderbilt U. . . . 26

2.3 What was not achieved, why not and what will be done to correct? . . . 28

2.3.1 TPC studies at Brookhaven National Lab and Yale Univ. . . . 28

2.3.2 TPC studies at Stony Brook . . . 28

2.4 What is planned for the next funding cycle and beyond? . . . 28

2.4.1 TPC studies at Brookhaven National Lab and Yale Univ. . . . 28

2.4.2 TPC studies at Stony Brook . . . 28

2.4.3 TPC studies at Vanderbilt U. 29

3 Full Barrel Tracker with Multiple Cylindrical Micromegas 29

3.1 What was planned for this period? 29

3.2 What was achieved? 29

3.3 What was not achieved, why not and what will be done to correct? 31

3.4 What is planned for the next funding cycle and beyond? 31

4 Fast Tracking Layer in Barrel Region with Cylindrical μRWELL 31

4.1 What was planned for this period? 31

4.1.1 Cylindrical μRWELL studies at Florida Tech 31

4.1.2 Cylindrical μRWELL studies at TU 32

4.1.3 Cylindrical μRWELL studies at UVa 32

4.2 What was achieved? 33

4.2.1 Cylindrical μRWELL studies at Florida Tech 33

4.2.2 Cylindrical μRWELL studies at TU 36

4.2.3 Cylindrical μRWELL studies at UVa 37

4.3 What was not achieved, why not and what will be done to correct? 43

4.3.1 Cylindrical μRWELL studies at Florida Tech 43

4.3.2 Cylindrical μRWELL studies at TU 43

4.3.3 Cylindrical μRWELL studies at UVa 44

4.4 What is planned for the next funding cycle and beyond? 44

4.4.1 Cylindrical μRWELL studies at Florida Tech 44

4.4.2 Cylindrical μRWELL studies at TU 44

4.4.3 Cylindrical μRWELL studies at UVa 45

5 End Cap Trackers with GEMs 45

5.1 What was planned for this period? 45

5.1.1 Florida Tech Large Carbon Fiber GEM Prototype with zigzag readout 45

5.1.2 UVa Large GEM Prototype with 2D U-V readout 45

5.2 What was achieved? 45

5.2.1 Florida Tech Large Carbon Fiber GEM Prototype with zigzag readout 45

5.2.2 Florida Tech and TU Simulation of Forward Tracking 48

5.2.3 UVa Large GEM Prototype with 2D U-V readout 50

5.3 What was not achieved, why not and what will be done to correct? 50

5.3.1 Florida Tech Large Carbon Fiber GEM Prototype with zigzag readout 50
5.3.2 UVa Large GEM Prototype with 2D U-V readout 50
5.4 What is planned for the next funding cycle and beyond? 50
5.4.1 Florida Tech Large Carbon Fiber GEM Prototype with zigzag readout 50
5.4.2 UVa Large GEM Prototype with 2D U-V readout 51

6 Developments for high momentum hadron identification at EIC 51
6.1 What was planned for this period? 51
6.1.1 MPGD sensors of single photons at INFN Trieste 51
6.1.2 New Photocathode Materials development at INFN Trieste 52
6.1.3 Large mirrors development at Stony Brook 52
6.1.4 New Radiator Studies at Stony Brook 52
6.2 What was achieved? 52
6.2.1 MPGD sensors of single photons at INFN Trieste 52
6.2.2 New Photocathode Materials development at INFN Trieste 53
6.2.3 Large mirrors development at Stony Brook 58
6.2.4 New Radiator Studies at Stony Brook 60
6.3 What was not achieved, why not and what will be done to correct? 60
6.3.1 MPGD sensors of single photons at INFN Trieste 60
6.3.2 New Photocathode Materials development at INFN Trieste 60
6.3.3 Large mirrors development at Stony Brook 60
6.3.4 New Radiator Studies at Stony Brook 60
6.4 What is planned for the next funding cycle and beyond? 60
6.4.1 MPGD sensors of single photons at INFN Trieste 60
6.4.2 New Photocathode Materials development at INFN Trieste 61
6.4.3 Large mirrors development at SBU 61
6.4.4 New Radiator Studies at Stony Brook 61

7 Critical Issues: Impact of COVID-19 pandemic 61
7.1 Brookhaven National Lab 61
7.1.1 How did the COVID-19 pandemic affect progress of your project? 61
7.1.2 How much of your FY20 funding could not be spent due to the closing of facilities? . . 61
7.1.3 Do you have running costs that are needed even if R&D efforts have paused? 61
7.2 Florida Tech 62
7.2.1 How did the COVID-19 pandemic affect progress of your project? 62

7.2.2 How much of your FY20 funding could not be spent due to the closing of facilities? . . 62
7.2.3 Do you have running costs that are needed even if R&D efforts have paused? 62
7.3 INFN Trieste 62
7.3.1 How did the COVID-19 pandemic affect progress of your project? 62
7.4 Stony Brook University 62
7.4.1 How did the COVID-19 pandemic affect progress of your project? 62
7.4.2 How much of your FY20 funding could not be spent due to the closing of facilities? . . 63
7.4.3 Do you have running costs that are needed even if R&D efforts have paused? 63
7.5 Temple University 63
7.5.1 How did the COVID-19 pandemic affect progress of your project? 63
7.5.2 Non-COVID related issues 63
7.6 University of Virginia 63
7.6.1 How did the COVID-19 pandemic affect progress of your project? 63
7.7 Vanderbilt University 64
7.7.1 How did the COVID-19 pandemic affect progress of your project? 64
7.8 Yale University 64
7.8.1 How did the COVID-19 pandemic affect progress of your project? 64

8 Manpower **64**
8.1 Brookhaven National Lab 64
8.2 Florida Tech 65
8.3 INFN Trieste 65
8.4 CEA-Saclay 65
8.5 Stony Brook University 66
8.6 Temple University 66
8.7 University of Virginia 66
8.8 Vanderbilt University 66
8.9 Yale University 66

9 External Funding **67**
9.1 Brookhaven National Lab 67
9.2 Florida Tech 67
9.3 INFN Trieste 67
9.4 Stony Brook University 67
9.5 Temple University 67

9.6 University of Virginia 67
9.7 Vanderbilt University 67

10 List of all EIC publications from the eRD6 Consortium **68**

Appendices **72**

A Appendix: MPGD sensors of single photons **72**
A.1 The principle and architecture of the MPGD sensors of single photons and the related R&D . 72
A.2 The developments of new photocathode materials suitable for gaseous photon detectors . . . 74

B Appendix: UVa **77**
B.1 Performance of the large-pad capacitive-sharing readout in beam tests 77
B.2 Development of capacitive-sharing large-pad anode readout 83
B.3 Minimization of capacitance noise and cross talk 84

1 Introduction

1.1 Brief overview of eRD6 project histories

The overall main focus of the R&D conducted by the eRD6 consortium has been the development of micro-pattern gas detectors (MPGD's) such as GEM, THGEMs, Micromegas, μRWELL, for tracking and particle identification at a future EIC. While each institution has been focusing on specific technical aspects of the R&D, much synergy has been produced with several collaborative efforts created over the years. For central tracking, BNL, Stony Brook and Yale have been mounting a long-term investigation of GEM-based TPCs readout structure, while Florida Tech, Temple U., and UVa have closely collaborated on the design, production, and testing of large GEM detector for the forward tracker. They jointly designed GEM foils for the EIC forward GEM Tracker prototypes and they have conducted combined beam tests at Fermilab. The latter three groups more recently teamed up to study the potential for a fast central tracker based on μRWELL detector technology and are collaborating to build the first fully operational cylindrical μRWELL prototype ever built worldwide. The team at CEA Saclay also recently join eRD6 consortium to explore the possibility for Micromegas technology to be proposed as a main EIC central tracker. The PID effort within eRD6 is spearheaded and is continued by Stony Brook U. and INFN Trieste with a focus on MPGD-based photon detection and the development of optical elements for high momentum RICH applications. The entire group meets bi-weekly to discuss progress and problems and to coordinate efforts. In addition, a smaller subgroup meets regularly on simulation efforts.

1.2 eRD6 Contribution to EIC Yellow Report Effort

The eRD6 consortium is playing an important role in the elaboration of the EIC Yellow Report (YR) document with contributions to several YR Working Groups (WGs), in particular Tracking and PID WGs. The developments performed within eRD6 activities are injected as input material in the relevant WGs, often accompanied by a dedicated effort to shape the information in a form adequate for the Yellow Report initiative. This core effort is accompanied by some specific personal contributions by eRD6 members:

- **Silvia Dalla Torre from INFN Trieste** is one of the conveners of the YR Detector Working Group (YR-DWG) overlooking the broad discussions related to the various EIC detector options under consideration including the detector integration and the complementarity aspects of different detector options. Her role as convener is complemented by her contribution to the discussions in WGs: PID, DAQ and electronics, integration and central magnet.
- **Kondo Gnanvo from University of Virginia** is one of conveners of the Tracking WG, one of the subgroups of the YR-DWG. He is specifically looking at all the aspect of gaseous detectors options including MPGDs technologies for EIC central tracking detector which include both the barrel and both end cap trackers.
- **Thomas Hemmick from Stony Brook University** is one of the conveners of the PID WG, one of the subgroups of the YR-DWG. He is dedicating specific effort to the comparative analysis of the several technologies proposed in order to perform PID from the low momenta ($\sim$1 GeV/c) up to the high ones ($\sim$50 GeV/c).
- **Alexander Kiselev from Brookhaven National** Lab is one of the conveners of the integration and central magnet WG, one of the subgroups of the YR-DWG. Among other efforts, he has built a software tool for fast modelling and generation of EIC Central Detector templates.
- **Matt Posik from Temple University** is the liaison between eRD6 groups and the YR WGs including physics working group (PWG), detector working group (DWG) and software group (SWG).

1.3 Summary Page: Barrel Tracker with TPC

A Time Projection Chamber (TPC) is one of the preferred detector options for central tracking and PID in an EIC detector due to its low mass, precision tracking, pattern recognition, and particle identification capabilities. We support building a TPC with roughly a 1 m drift length in both the hadron and electron-going directions that utilizes a thin field cage and a low mass endcap readout plane, equipped with a high resolution MPGD detector for collecting, amplifying, and reading out the collected drift charge.

1.3.1 Accomplishments to date

The following is a list of TPC-related R&D items we have investigated over the last decade in connection with the eRD6 consortium:

1. Gas characterization measurements: drift velocity, transverse diffusion, absolute gain, attachment, IBF, energy resolution
2. Readout plane optimization: the development of zigzag interleaved readouts for enhanced charge sharing to reduce channel count while maintaining excellent position resolution and uniformity of response (a first iteration of this process was already done for the sPHENIX TPC)
3. Recent developments of a 2D interleaved readout may allow for the possibility to enhance charge sharing (and in turn improve the position resolution) in a direction orthogonal to the pad rows
4. Bipolar gating grid studies: a passive gating grid option that avoids disrupting data taking in a high rate environment
5. Investigations into various MPGD-based gain elements: 4GEM, Micromegas, μRWELL, and Micromegas + 2GEM
6. Construction of a "mini-TPC" prototype and a TPC prototype with a larger cylindrical field cage enabled developments in track reconstruction using test beam measurements of the position resolution, angular resolution, N_{eff}, and transverse diffusion in a candidate gas
7. Development of laser-based calibration schemes for a TPC: line laser tracks and rapid (15kHz) generation of reference clusters from an array of strip photocathodes deposited onto field cage cathode
8. Tested streaming DAQ candidate: SAMPA front end electronics were used to read out two different prototype TPC detectors in both a lab setting and at a test beam. We also tested the DREAM front end electronics where steaming is possible, but at a relatively low rate.

1.3.2 Technological readiness

In addition to the various R&D items listed above, several members of our consortium are directly involved in the effort to build the sPHENIX TPC for measuring collisions at RHIC. Many important aspects of assembling this TPC that have been learned can be used to construct a TPC at EIC. They include the following and provide an indication of the technological readiness for this detector:

1. The development of techniques to minimize space charge, including an understanding for making an appropriate gas choice, the employment of a bipolar gating grid, and operating a 4GEM readout with an optimized field configuration to minimize IBF have been demonstrated.
2. We are in the process of developing methods for a superior dE/dx measurement, including employing a cluster counting technique (in addition to using a truncated Landau mean) and choosing a working gas with a large total ionization yield to secondary ionization yield ratio (n_T/n_p) for reducing the high energy Landau tails.

3. We have in place well thought out and proven manufacturing/assembly techniques for building the TPC support structure, GEM assembly (and QA), thin field cage and cathode assembly, and have gained engineering expertise for identifying critical infrastructure and installation requirements.

4. We have in place a good model for the full electronics chain for the DAQ system.

5. We have in place methods and simulation tools to correct for space charge distortions, including a space charge model in the TPC. The role of an outer tracking layer to aid the TPC in these corrections is also well defined, and we have implemented a laser-based calibration system that can serve as a model for a future, similar system.

1.3.3 Work remaining for a TDR

The work remaining to generate a TDR for a new TPC at EIC is extensive and goes beyond the purview of our group. However, based on our experience, the work to be done includes, but is not limited to the following:

1. Further optimization studies: IBF vs energy resolution; choice of optimal working gas for dE/dx; final design of anode pad plane; determination of optimal running parameters like the drift velocity and gain; determination of the front end electronics requirements like the shaping time and dynamic range

2. Development of an endcap design with less material compared to the sPHENIX TPC

3. Determination of what acceptance and resolution is sufficient at the EIC, including the number of pad rows the spatial resolution, and how these interplay with other tracking detectors (e.g., silicon vertex) and their impact on the overall dimensions of the detector

4. Scaling current sPHENIX data taking rate capability to better match EIC collision rate

1.3.4 Cost estimate and timeline

Because the design of a full TPC at EIC is beyond the purview of our group, it would be impractical at this time to provide an estimate of the cost and a timeline for the completion of this project. However, based on our experience in developing the design for the sPHENIX TPC, we estimate that in order to complete a TPC design for EIC that would be ready for a TDR, this would take on the order of two years (including prototyping) and cost between $200K - $300K.

1.4 Summary Page: Barrel Tracker with Cylindrical Micromegas

In the central pseudorapidity region of an EIC detector, the silicon vertex detector can be complemented by a low material budget MPGD tracker instead of a TPC. The goal is to study the feasibility and the impact on tracking performance of several concentric layers of Micromegas tiles.

Accomplishments to date

The performance of a Micromegas tracker solution has been tested with full Geant4 simulations of the EIC central barrel detector where the TPC has been substituted with a set of Micromegas layers. Each layer consists of 50 cm wide curved detector elements (tiles), long enough to cover the range $|\eta| < 1$. Each tile has a 2D readout and the spatial resolutions both in the z and the $r \cdot \varphi$ directions are assumed to be 150 μm. The detailed implementation in simulation of each tile is based on the technology developed for the CLAS12 barrel Micromegas tracker: the material budget in the active area of each detector is about $\sim 0.3\%$ X/X_0.

Several configurations of five and six layers have been simulated. Results included in the Yellow Report show, both in terms of material budget and tracking performance, that a Micromegas tracker is within the requirements and it is competitive with the nominal TPC implementation.

Studies on how to reduce even further the material budget have started. We plan to focus on how to simplify production and installation. A PCB-less planar design is being investigated as the potential solution for the basic tile of a modular tracker.

Technological readiness

The 1D readout curved Micromegas technology has been successfully installed in the CLAS12 experiment. Also with a 2D readout, this solution will meet the requirements in terms of material budget.

Work remaining for a TDR

- **Curved Micromegas:** test the 2D readout, possibly with zigzag readout patterns, to confirm the production feasibility and the spatial resolution for the resistive technology; design a light support structure for the whole tracker.
- **Very low material budget planar Micromegas:** implement the list of materials in simulation; study the optimal configuration for a full tracker based on a modular design; build and test a demonstrator prototype.

Cost estimate and timeline

For the low material budget Micromegas a small scale demonstrator will be build this year. For the 2D readout, studies on the readout pattern and the resistive material will be carried out in order to optimise the spatial resolution: a small batch of readout prototypes should be foreseen. Tests with cosmic rays will be performed at Saclay. Travel money for beam tests should be foreseen.

1.5 Summary Page: Fast Tracking Layer with Cylindrical μRWELL

In the central detector region, we envision implementing at least one thin (few cm in radius) cylindrical μRWELL layer just outside the main tracker volume. This layer will provide fast timing information for vertex identification and it will also seed particle identification by providing precise track impact points and directional information for particles that impinge on a PID detector, e.g. a DIRC, located directly behind this μRWELL layer.

Accomplishments to date: The impact of a cylindrical μRWELL layer on the reconstructed angular resolution of tracks was studied within the EicRoot simulation framework. The cylindrical layers were placed in the central region ($|\eta| < 1$) at various radial positions. We found significant improvement in the angular track resolution when layers were placed radially in front and behind a DIRC (see previous eRD6 reports).

With these encouraging results from the initial simulation, we began designing a prototype concept. We are working with CERN to produce a low-mass version of the composite μRWELL foil with reduced thickness of the PCB substrate and the readout layer. In parallel we are working on the mechanical support structure for a cylindrical μRWELL detector. We have successfully designed and constructed a small mechanical mock-up of the detector using Kapton foils and a 3D-printed support structure.

Technological readiness: Planar μRWELL detectors have been demonstrated by others and by our consortium to be a viable MPGD with good performance characteristics for tracking applications. A fully functional cylindrical μRWELL detector is yet to be demonstrated.

Work remaining for a TDR: A small functional cylindrical μRWELL prototype ($\sim$ 20 cm diameter and $\sim$ 55 cm length) needs to be built and tested in beam. The detector will be operated in μTPC mode to provide tracklet information. It will need to be assessed for mechanical stability and tracking performance. The mechanical design of this prototype and its support structure is underway within eRD6 via the R&D on the mechanical mock-up.

Cost estimate and timeline for small functional cylindrical prototype with μRWELL layer: Up to the TDR, we estimate the core cost for procuring active detector components (foils), mechanics, electronics, and for production of the prototype to be \$25k. Performance tests in a beam will require an extra \$15k for travel between institutions and to Fermilab. Personnel costs (graduate students) are estimated at \$50k per year. The total estimated cost is \$140k over two years. With proper funding this development phase is expected to be completed in two years, including test beam effort and analysis of results (assuming no delays related to COVID-19).

1.6 Summary Page: Endcap Trackers with MPGDs

Large-area planar MPGD trackers can be used in the forward and backward endcap regions to provide global tracking as well as local positional information for a PID detector located behind the forward tracker, such as a RICH detector. The candidate technologies under consideration by our consortium for this application are Triple-GEMs and μRWELL detectors.

Accomplishments to date: Large-area ($\sim$1 m long) GEM foils and mounting frames have been designed specifically for use in an EIC detector and with minimization of material in the active area in mind. These foils and frames were used to construct two large-area and low-mass Triple-GEM prototype detectors. Each prototype uses a distinct assembly and readout technique. One prototype detector was tested successfully in a proton beam at Fermilab. The other one is being refurbished to improve mechanical stability of the frames. Small-area ($\sim$ 100 cm^2) generic μRWELL detectors were also successfully built and tested in the same beam.

Technological readiness

- **GEM**: GEMs represent mature technology whose performance and limitations are well known. Large-area Triple-GEM detectors are being used in a number of large nuclear and particle physics experiments.
- **μRWELL**: μRWELLs are a more recent MPGD technology and have been demonstrated to be a viable tracking option.

Work remaining for a TDR:

- **GEM**: A final technical design has to be produced following guidance from the prototyping and simulation results and validated in a beam test.
- **μRWELL**: Jefferson Lab has recently dedicated R&D efforts towards developing large-area μRWELLs for use in their future experiments. One of our consortium members (UVa) is directly participating in that effort.
- **Low-mass μRWELL Foil**: The material budget of the current standard μRWELLs available from CERN needs to be reduced in order to better fit within the EIC material budget, in particular in the backward direction where the material budget is critical for electron tracking. This involves reducing the thickness of the flexible PCB that the μRWELL is mounted on and making a transition from readout board to readout foils. We are working with CERN to produce such a low-mass μRWELL foil.

Cost estimate and timeline: For the Triple-GEM prototypes, no additional funds are needed beyond what has already been funded. It is expected that the large-area μRWELL R&D at Jefferson Lab will be completed within a year. We will be following that R&D development closely and decide at the time of its completion if further R&D is needed for an application of planar μRWELL detectors in an EIC detector.

1.7 Summary Page: Development of MPGDs for High Momentum Hadron PID

MPGDs-based single photon detectors are developed for Cherenkov imaging applications, using as starting point the hybrid MPGDs in use since 2016 in COMPASS RICH [1]. In the EIC context, the typical collider-type setup imposes a compact design of the RICH for High Momentum Hadron PID. When gaseous photon detectors are used, a compact RICH can be obtained using the windowless approach [2] with the radiator gas also used as the gaseous detector gas. It is so possible to detect very far UV photons (∼120nm), where the photon yield is more abundant and, therefore, the radiator can be short $\mathcal{O}$(1 m). The R&D is performed along two development lines, whose status is separately discussed in the following.

1.7.1 Development of MPGD sensors of single photons

Development Goal - The hybrid MPGDs of single photons have to be upgraded in order to meet the needs of a compact RICH. The main development lines are the miniaturization of the read-out pads required because of the short lever arm and the validation of the read-out with the VMM3 front-end chip for the specific application of single photon detection. VMM3 is expected to provide very low noise figures also for detectors with non-negligible capacitance and its architecture is adequate for data acquisition based on streaming read-out models.

Accomplishments to Date - A first version prototype with miniaturized pad-size was realized and characterized, also in test beam. The second version is under construction. Preparatory activity in order to read-out the second prototype with VMM3 front-end has been performed. This includes the procurement of the electronics boards and preliminary exercises to read-out the front-end chip. The progress of this activity has been heavily penalized by the restrictions imposed by the pandemic emergency.

Technological Readiness - The prototype has been demonstrated in a test beam environment.

Work remaining for a TDR - The completion of the R&D development, expected in 24 months and, in parallel, a complete simulation of a gaseous RICH making use of these detectors.

Cost estimate and timelines - The planned activity can be completed within 12 months if no further delay is imposed by the persisting limitations related to the pandemic emergency. No further financial resources are needed for next year as part of the already allocated resources could not be used due to the pandemic emergency. On the contrary, standard level of financial support is needed for the last year of the activity corresponding to about 40k$.

1.7.2 New Photocathode Materials for gaseous detector

Development Goal - So far, CsI is the only photoconverter successfully used in gaseous detectors. It is fragile due to its chemical reactivity to water vapor and because the bombardment of the ions created in in the multiplication process degrades the Quantum Efficiency (QE). The proposed novel photoconverter by Hydrogenated NanoDiamond (H-ND) powder [3] is expected to be more robust, as confirmed by the initial studies. The development aims at establishing the use of photoconverters by H-ND in gaseous detectors and determine the key parameter of ND powders to obtain maximum and reproducible QE.

Accomplishments to Date - The assessment of the compatibility of the novel photoconverter with gaseous detectors is well advanced. The identification of the key parameters for high and reproducible quantum efficiency of the ND powder is at an initial stage.

Technological Readiness - Prototypes have been demonstrated in laboratory environment.

Work remaining for a TDR - This being a highly innovative development, it requires another three or fours year for completion. If successful, it will represent an upgrade of the MPGD sensors of single photons. Therefore, this option can appear in a TDR only as potential improvement of a baseline design with CsI.

Cost estimate and timelines - Support at the level of 30k$/y is needed during the completion period: about 100 k$ in total.

1.8 Summary Page: New Radiator Materials for PID

The investigation towards new radiator materials for PID belongs into the category of blue skies research and can therefore not be addressed in the context of this summary.

1.9 Summary Page: Large Mirror Development

The installation of the PVD equipment has been finalized, the commissioning of the device has been established and the remaining task is to gain experience with the PVD process for certain applications. It can be concluded that the PVD device is ready for use.

2 Barrel Tracker with TPC

2.1 What was planned for this period?

2.1.1 TPC studies at Brookhaven National Lab and Yale Univ.

The goals for this funding cycle are listed below:

- We planned to test and install a newly designed zigzag PCB into our mini-TPC prototype to measure tracks produced by our TPC laser system and compare to measured cosmic tracks. In parallel, we planned to have identical zigzag PCBs outfitted with Micromegas and μRWELL gain elements to be installed onto the TPC prototype at a later date for similar tests. We also planned to read out the TPC with DREAM or SAMPA front end electronics.
- We planned to use our high intensity x-ray scanner to test the new TPC readout board coupled to a 4-GEM, independent from the TPC field cage, to provide a baseline measure of performance. At the same time we planned to complete the development of a software plug-in to fully incorporate the DREAM hardware with our RCDAQ DAQ software.
- While testing MPGD detectors in our x-ray scanner, it was determined that the range of 3 and 5 keV photoelectrons from x-ray conversions in the working gas significantly broadens the measured residual distributions compared to results from a high energy particle beam. As a result, we sought to generate a more confined cluster of charge in the working gas, by exposing our detectors to the lowest available energy x-rays, with relatively short ranges.
- We proposed to characterize various interesting TPC gas candidates by comparing relevant performance criteria. These studies may include gas gain measurements, attachment, drift velocity, charge spread measurements, and IBF measurements.
- We planned to design and test several novel MPGD-style interleaved r/o anode designs adapted for a photosensitive LAPPD detector. Once we've completed the assembly of the detector apparatus, the immediate plan was to measure the position resolution using these LAPPD readout using a laser beam focused to a small spot on the photocathode. (Note that this project, while not part of our original plan for R&D on TPCs, its development was closely related and was essentially supported entirely by our LDRD in MPGD for EIC.)

2.1.2 TPC studies at Stony Brook

Planned efforts at SBU were to continue the investigation of IBF blocking structures to be used in an MPGD-based readout structure for a TPC. In particular, the concept of a passive gating grid is in the focus of our investigations.

2.1.3 TPC studies at Vanderbilt U.

Vanderbilt University joined 4 months ago to erD6 effort. During this period we had planned to :

- **MPGD R&D bench set up and study basic characteristics of MPGD detector :** Setting up MPGD R&D bench capable of measuring various characteristic of different variants of MPGDs like effective gain, energy resolution, time resolution, spatial resolution, IBF. Plan was also to do effective gain scanning and IBF suppression using multi-layer GEM detector for different kinds of Ar based gas mixture.

- **Simulation studies :** The simulation studies were focused on performing Finite Element Method coupled with Garfield++ for characterizing basic performance of GEMs and micromegas under different gases and voltage configurations.

2.2 What was achieved?

2.2.1 TPC studies at Brookhaven National Lab and Yale Univ.

High Spatial Resolution Measurements with X-ray Scanner: The following is an update on the continued development of our high flux, narrow beam (25 μm $\times$ 25 μm) x-ray scanner, for the purpose of characterizing readout planes for MPGD-based detectors. We have made a significant improvement in the ability of the scanner to measure position resolutions on par with results from a test beam. Last we reported observing 78 μm by exposing a 4-GEM detector equipped with a COMPASS style, x, y-straight strip readout to a highly collimated beam of 8 keV x-rays. (It turns out, however, that the x-ray potential was set such that the x-ray energy corresponded to a maximum of about 12 keV, meaning the majority of generated x-rays was actually significantly smaller than 8 keV.) The disagreement of this number with the measured resolution of 55 μm using a particle beam was attributed to the relatively large range of secondary photoelectrons from x-ray conversions in the detector working gas. As a point of reference, 5.89 keV x-rays from an Fe^{55} source produce $\sim$ 3 keV photoelectrons with a range of about 100 μm in Ar, whereas $\sim$1 keV photoelectrons have a range of tens of microns and would contribute significantly less to the overall centroid residual width.

In order to establish a more point-like charge reference, we have since explored the possibility to reduce the photoelectron range by reducing the x-ray energy. Reducing the potential on the x-ray tube to about 10 kV effectively eliminates the $\sim$8 keV K-alpha and $\sim$9 keV K-beta peak from the Cu target and generates a low energy Bremsstrahlung spectrum corresponding to a significantly reduced average photoelectron energy. The effect on the measured resolution is summarized in Fig.'s 1 and 2, for a 4-GEM detector mounted to a straight strip readout with 400 μm pitch. As seen in the left plot of Fig. 2, the measured resolution suffers substantially for larger x-ray energies, likely corresponding to the Cu emission lines, which dominate the x-ray spectrum. (NB: the 8 keV line is about 6 times more intense than the 9 keV line.) Additionally, the extrapolated resolution for an average photoelectron energy approaching a few keV (corresponding to a HV tube setting of about 1V and a max Bremsstrahlung energy of about 5 keV) is in the 50 - 60 μm range, the expected resolution measured in a particle beam. One can also see in the right plot of the same figure that the expected differential non-linearity for this COMPASS-style readout is quite small, as expected.

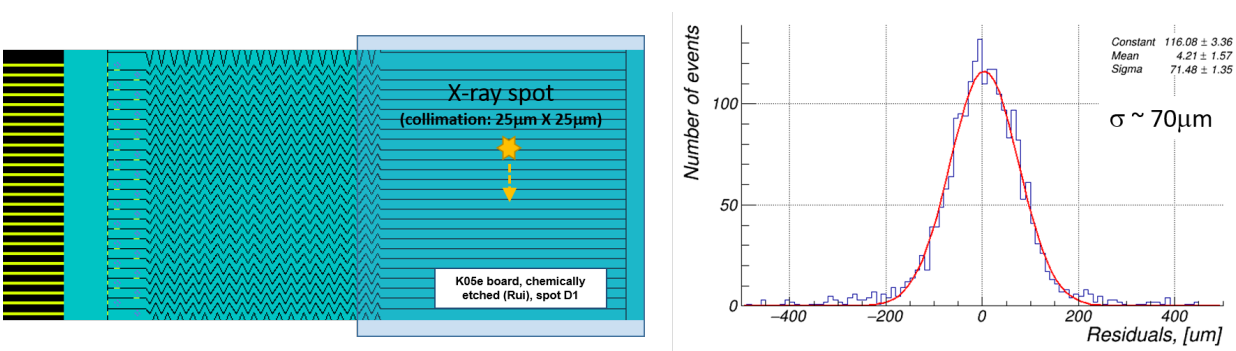

Figure 1: Position residual distribution of a 4-GEM detector read out with a 400 μm straight strip pad plane exposed to a low energy x-ray beam. The residual distribution is a convolution of the $\sim$ 25 μm collimator (width), the detector intrinsic resolution (perhaps 40+ μm) and the x-ray secondary electron range (which is likely the dominant component). For this measurement the x-ray tube potential was set to $\sim$ 8.5 kV.

Reducing the x-ray tube potential expectedly comes at the cost of a severely reduced trigger rate. At full energy, the x-ray detection rate for the collimated beam is tens of kHz, but is less than 10 Hz at the smallest

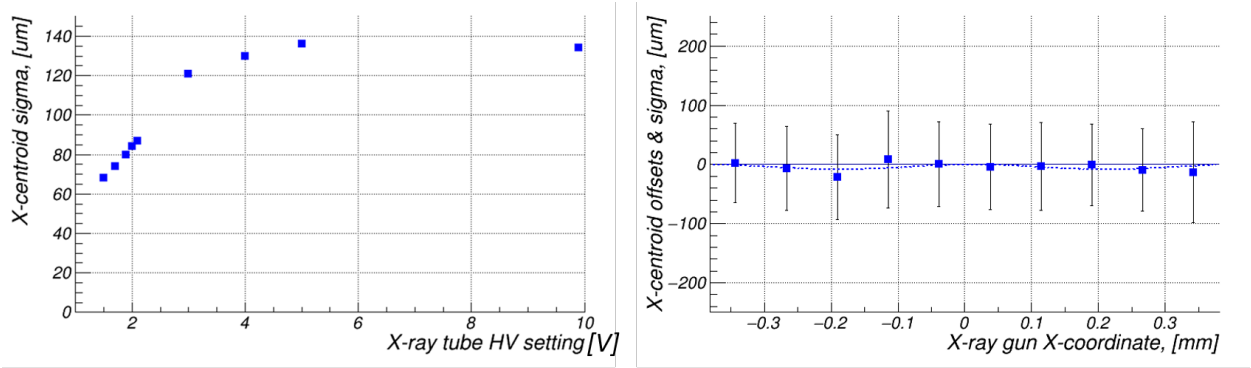

Figure 2: Left: X-ray tube potential (10 V = 50 kV) Vs measured position resolution from a 4GEM with same straight strip readout. Right: Centroid mean and measured resolution (error bars) Vs x-ray tube position.

energies. The absorption edge in Ar is largely responsible for the reduced rate at just below 3 keV, however as the mass attenuation cross section drops to 1-2 keV, absorption in the gas is fully restored. One possible solution to maximize the effective rate of the low energy x-rays is to operate the x-ray tube at a potential just below the excitation energy of the Cu K-alpha peak. This maximizes the output from the low energy Bremsstrahlung spectrum, then an offline cut may be applied to eliminate the higher energy x-rays. Due to the GEM gain fluctuations, such a cut would not be be very efficient, but at least provides a means to alter the ratio of high and low energy x-rays included in the data analysis.

Zigzag-based Readouts for a TPC: As described in the last report, we have designed and ordered from the CERN PCB shop an optimized zigzag PCB readout for our 10 cm drift mini-TPC prototype (see Fig. 4a. The board consist of a 10 cm $\times$ 10 cm active area filled with 500 2 mm $\times$ 10 mm zigzag shaped anode pads. We have since received three identical PCBs, each of which was tested for shorts and electrical continuity. One PCB was mounted to a 4-GEM and QA tested with an Fe^{55} source. This PCB is slated to be installed in our mini-TPC prototype for various TPC R&D studies and will be used to confirm the resolution performance with cosmic tracks.

Two of the three PCBs were sent back to CERN to be converted to a μRWELL detector and bulked with a Micromegas detector. Once received, the converted PCBs will be tested in our x-ray scanner to get a baseline measure of performance and will eventually be installed into the mini-TPC prototype to continue the TPC R&D program.

Progress with Mini-TPC prototype: We have made good progress with outfitting our mini-TPC prototype with a source of diffuse light to illuminate an array of straight-strip photocathodes on the field cage cathode plate. Liberated electrons from the strip photocathodes provide a reference signal for the purpose of calibrating the TPC response in the presence of distortions due to mechanical imperfections or the accumulation of space charge in the drift volume. The implementation of this scheme in this prototype detector is for the purpose of demonstrating a proof of principle for this calibration concept. In a real TPC, signals from such an array of photocathodes, pulsed at a very high rate, in principle can provide a repeatable and stable reference on an event by event basis.

Laser light coupled into a fiber optical cable is routed to the interior of the TPC vessel and escapes from the fiber exit aperture to produce a source of diffuse light, as shown in Fig. 3. The output tip of the fiber is sculpted for the purpose of de-focusing the light beyond the cone angle from the fiber's numerical aperture. By applying a rounded surface on the fiber core, light escaping from the fiber is able to fill most of the field cage cathode containing the photocathode strips, as shown in Fig. 4. Though the light also illuminates the surrounding copper-clad field cage and cathode top-plate, the quantum efficiency ratio at the laser wavelength of 266nm is about 200:1 for Al and Cu, respectively.

In this design, the laser light is able to be directed upward to generate laser tracks in the field cage or

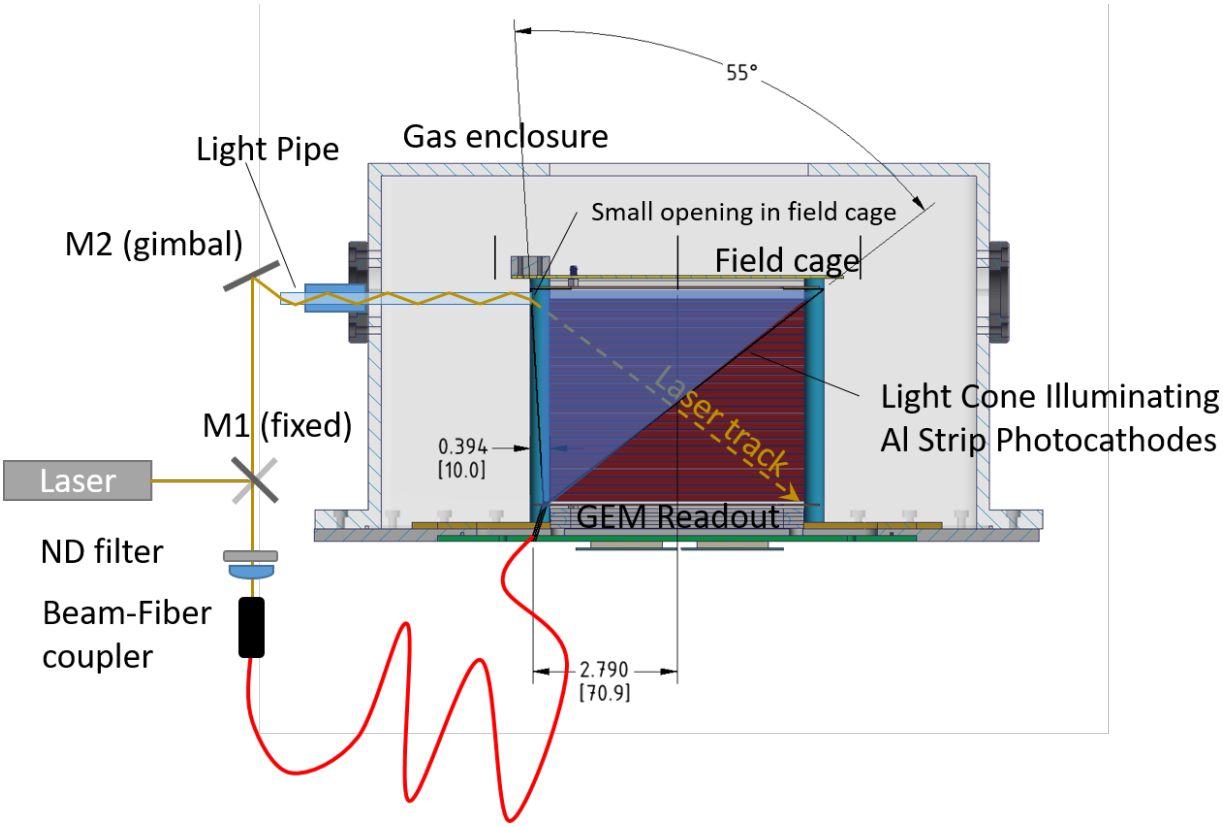

Figure 3: Sketch of the mini-TPC prototype, showing light from a fiber optical cable illuminating the cathode plate of the field cage. Additionally, the external laser beam may be redirected upward to generate steerable laser tracks within the drift cage volume.

downward to generate diffuse light for the field cage cathode. This prototype is thus capable of measuring cosmic tracks, laser tracks, or a well defined array of electron clusters drifting across the full drift volume, all in a lab setting.

Straight Strip Vs Zigzag readout: We have completed the data analysis from our March 2019 beam test at Fermilab regarding the comparison of straight-strip and zigzag shaped charge collection anodes for MPGDs and have recently submitted a new draft manuscript to IEEE TNS summarizing these results [4]. Some highlights from this analysis are presented here.

The segmentation of the readout plane for MPGD-based detectors can play a critical role for the detector performance, especially for the spatial and angular resolution and should be seriously considered for a future TPC. To improve the resolution, a typical strategy is to simply reduce the pitch of the anodes, but this comes at the cost of greater instrumentation. As an alternative, highly interleaved anode patterns, such as zigzags offer relatively coarse segmentation, while preserving performance [5] [6]. By optimizing the three main operant geometric parameters of the zigzag (including the pitch, the periodicity of the zigzag, and the degree of interleaving, here referred to as the "stretch" parameter), charge sharing among neighboring pads or strips may be finely tuned for specific avalanche schemes.

Fig. 5 shows the raw detector response for both a straight strip and zigzag patterned readout over a range of pitch values for a 4-GEM detector. Similarly, Fig. 7 compares the resolution as a function of the pitch for various zigzag parameters in a GEM, Micromegas, and μRWELL detector. In all cases, the position resolution is comparable below a pitch of 1mm, but the resolution quickly degrades for straight strips at larger pitch. This is mainly due to poor charge sharing, where the majority of charge is collected by a single pad. An equally beneficial feature of zigzags is the ability to maintain a highly uniform and linear response

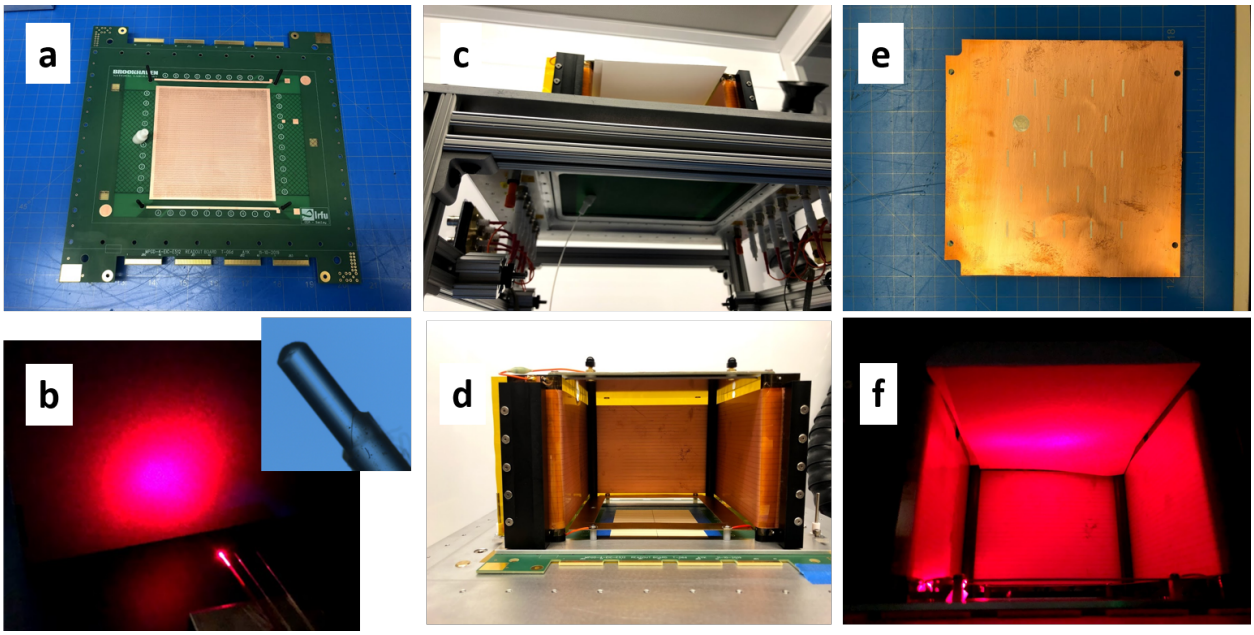

Figure 4: a) New TPC zigzag PCB with fiber feed-through; b) diffuse output from sculpted fiber tip; c) fiber passing through fiber feed-through; d) field cage test fit with PCB underneath; e) array of photocathode strips on field cage cathode; f) cathode illuminated with laser light via fiber optical cable.

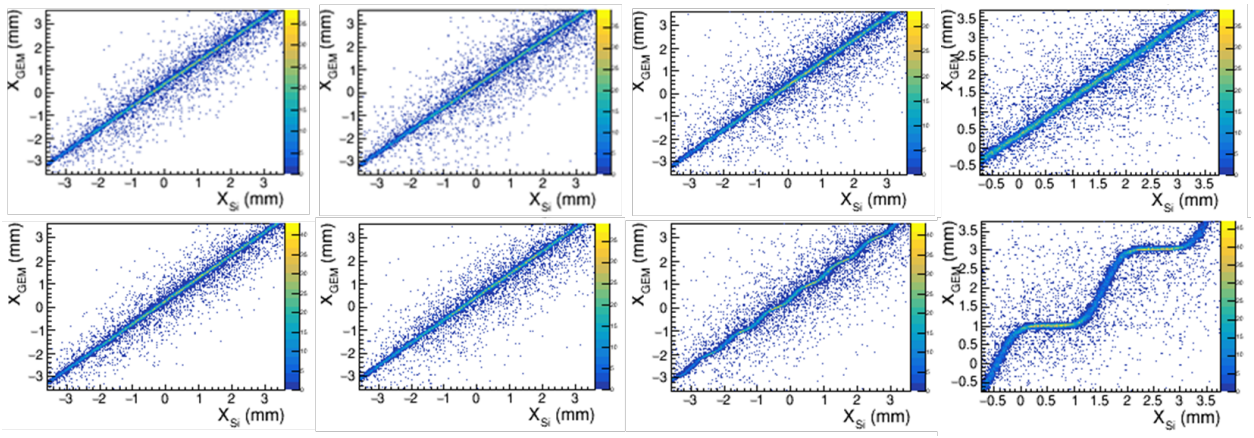

Figure 5: Correlation between the track position as measured with a high resolution Si telescope and the reconstructed position as measured in a 4-GEM detector for both a zigzag (top row) and straight strip readout (bottom row). The pitch in each column corresponds to 0.4 mm, 0.67 mm, 1.0 mm, and 2.0 mm respectively.

across the full detector acceptance. The "out of the box" detector response of optimized zigzag anodes is shown in Fig. 7, which includes a purely Gaussian raw residual distribution, without the need for pad response functions, as in the case of straight strips. Ultimately, in situations where the detector occupancy is fairly low and a relatively coarse readout segmentation is acceptable, zigzag shaped charge collection anodes provide a very efficient means of encoding high resolution positional information, with values remaining below 65 μm for a pitch as large as 3.3 mm as indicated in the right-hand plot.

2D Zigzag Readouts: We have also taken x-ray data with a newly procured readout PCB with a 2D zigzag-like pattern, described in earlier reports and seen in Fig. 8. The PCB consists of several 2D charge sharing pad and strip patterns with various geometric parameters, along with several straight strip and

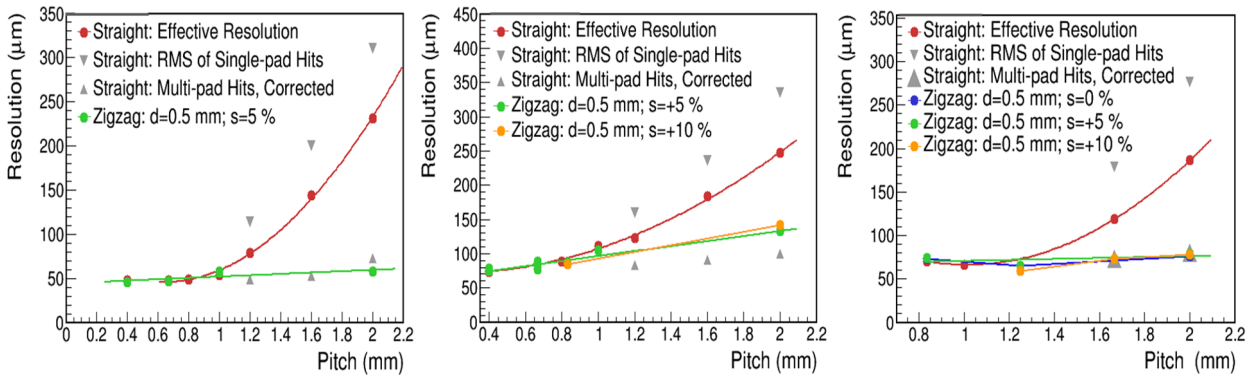

Figure 6: Position resolution vs. pitch for straight strip and zigzag shaped anodes in GEM, Micromegas and μRWELL detectors respectively, measured in a 120 GeV proton beam. The resolution is shown for a zigzag period (d) of 0.5 mm and various stretch parameters (s). The resolution for straight strips is corrected using pad response functions, however the raw resolutions are quoted for the zigzags. The resolution for the straight strips is broken down into regions of the readout dominated by single and multi-pad clusters (grey points), where the red points denote the weighted average.

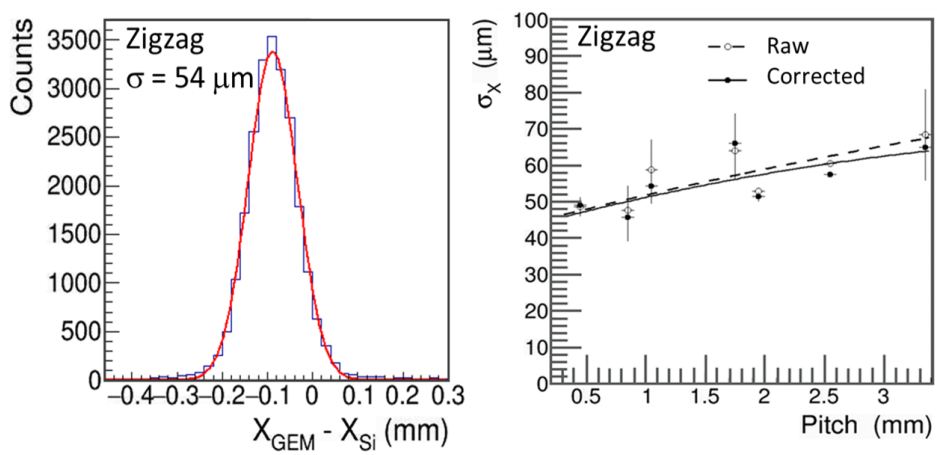

Figure 7: Raw residual distribution for zigzag anodes with pitch = 2 mm, period = 0.4 mm, and stretch = 0 % and a plot of the position resolution vs. pitch in the case of a 4-GEM detector, respectively.

square-pixelated patterns meant for comparison. This PCB is realized on a double-sided kapton sheet, making the fabrication and design of the PCB relatively straight forward and the PCB itself highly versatile for many applications.

Results for a 2D zigzag pattern with 1.5mm pitch and a 0 % stretch parameter is shown in the same figure. The resolution and the deviation of the centroid mean from a linear response is shown in the plots to the right and reveal a position resolution of about 70 μm on average and a maximum deviation from a linear response of about 50 μm. It must be noted that no optimization for the zigzag parameters has been done here and in principle both the resolution and uniformity of response may be improved upon. These tests were meant simply as a demonstration of the concept for a 2 dimensional readout using zigzag-like shaped anodes on a single sense plane.

In the meantime, we have also completed a DREAM plugin driver so that the DREAM DAQ hardware can be run with our default DAQ software, RCDAQ. This makes all of the analysis tools developed for RCDAQ now available to analyze DREAM data.

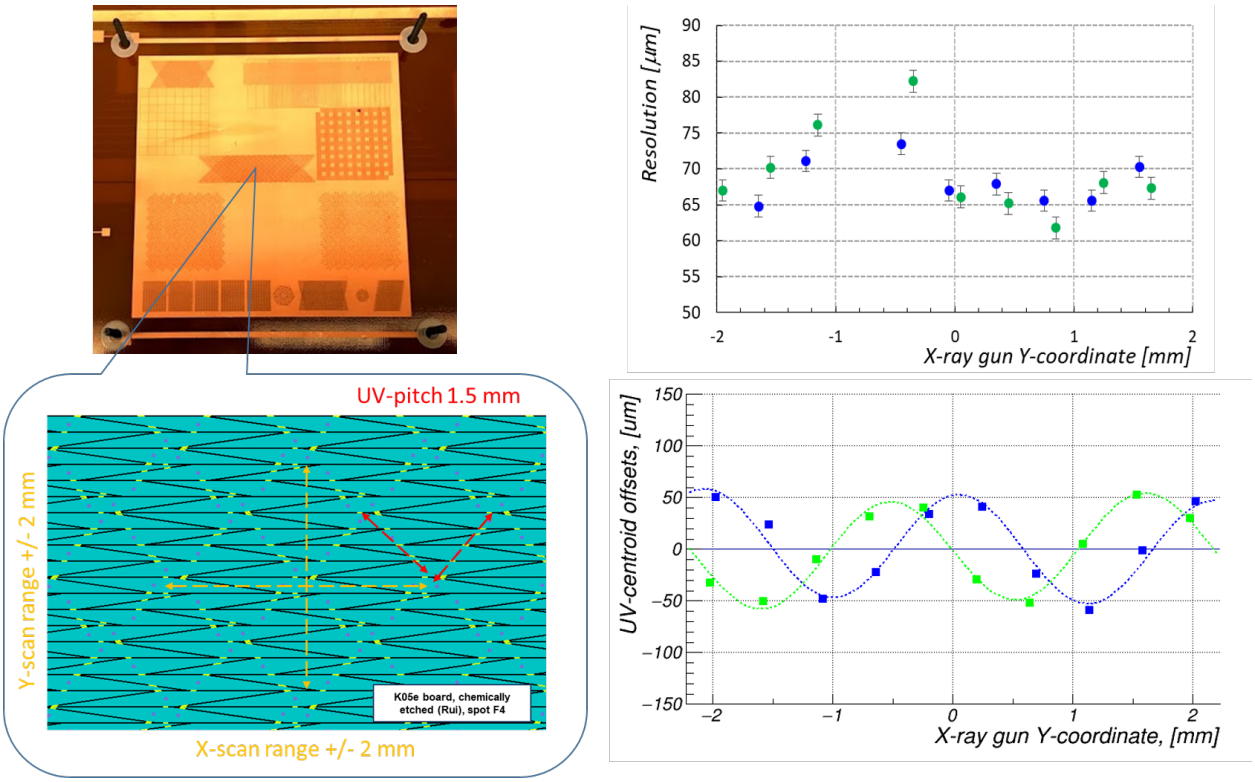

Figure 8: Picture of 2D zigzag PCB and the Gerber file layout of the anode pads, showing vias (blue circles) electrically connecting neighboring diamond-shaped pads together, as indicated by the underlying yellow traces, in two orthogonal directions, U and V. To the right, plots of the position resolution and centroid mean for the U and V-directions (green and blue data points, respectively) is shown for a scan along the Y-coordinate direction of the x-ray tube motor.

Progress on Gain Element and Gas Mixture Studies for a TPC at EIC: We have continued our investigation of two candidate MPGD-based gain elements and a range of gas mixtures for a high rate TPC readout at EIC. Since space charge in the drift volume is the most detrimental aspect of operating the TPC, we have concentrated on ways of minimizing IBF, while maintaining good energy resolution, an equally critical feature. In addition to these, the electron drift velocity, ion mobility, transverse diffusion, and the gas gain are specifications that must also meet certain criteria. Ne mixed with a small percentage of CF_4 and CH_4 is generally satisfactory, however there are certain important aspects to consider. CH_4 at a 10% level is desirable because it is known to be an effective "cool" gas component and falls below flammability levels. The optimal percentage of CF_4, on the other hand, is not immediately clear. Higher concentrations of CF_4 require a higher potential to be applied across the gain element to keep the gain constant. At the same time, this impacts the flow of charge through the gain structure, which changes the IBF and energy resolution characteristics, as seen in Fig. 9 for a 4-GEM and a 2-GEM + Micromegas (MMG) readout over a range of mixing ratios.

For each mixture, the gain was fixed at 2100 - 2200, but the optimal CF_4 concentration is different for the two gain options. For the 2-GEM + MMG option, 10% CF_4 was found to be optimal, whereas 35 - 40% performs best in the case of a 4-GEM. It is also important to note that both gain structures passed the same stability test when exposed to a high flux of x-rays. In the case of the MMG, in particular, there was a very low probability of sparking. Additionally, with the application of a resistive layer on the readout plane, the drop in the high voltage and the resulting drop in gain and the recovery time were found to be within tolerable levels.

Application of MPGD-style Interleaved Readouts for LAPPDs: Large Area Picosencond Pho-

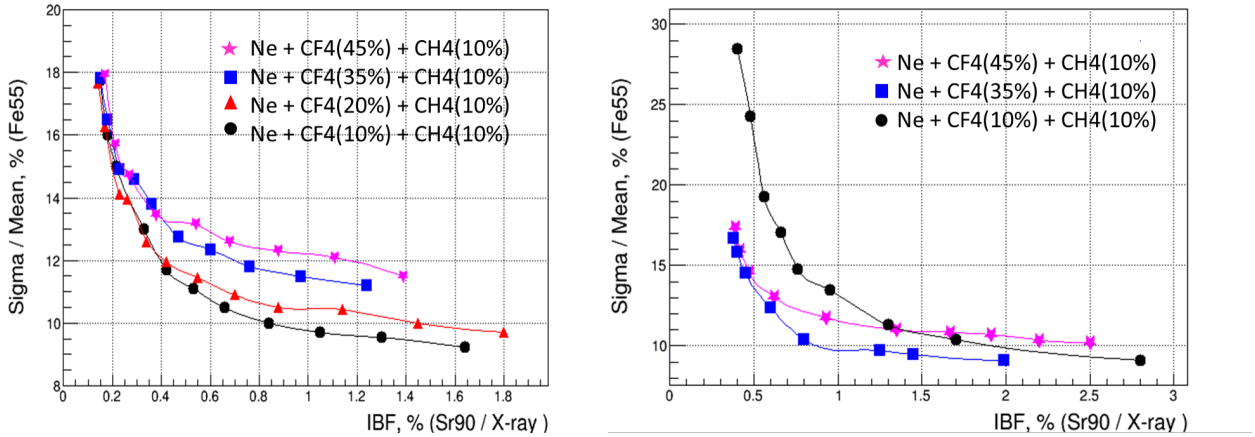

Figure 9: IBF vs Energy Resolution for different mixing ratios. Left: MMG + 2GEM detector ($E_{drift} = 0.4kV/cm$ Gain ~2200). Right: 4-GEM detector (ALICE TPC upgrade style; $E_{drift} = 0.4kV/cm$, Gain ~ 2100).

todetctors (LAPPDs) are low profile (~2 cm thick), vacuum sealed, microchannel plate-photomultiplier based detectors with an active area of up to 20 cm × 20 cm. They offer excellent timing resolution (10 - 20 ps), a multi-alkali transmissive photocathode with high quantum efficiency (25 % at 365 nm), high gain ($\sim 10^7$), and intrinsically carry high resolution positional information. These devices are nicely suited for high performance ToF and RICH applications for PID and may also be used to extract high resolution space points from energetic particles generating Cherenkov radiation in the entrance window.

We propose to couple an LAPPD module (or "tile") to a modular-RICH (mRICH) detector to establish a high performance, compact PID detector. At the same time, the collection of the small cluster of Cherenkov photons generated in the 5mm thick quartz LAPPD window allows for a high resolution position measurement. To accomplish this, we also propose to read out the sensor with an interleaved anode pattern, similar in concept to ones we have developed for MPGDs, which effectively enhances charge sharing and delivers a resolution significantly better than the *pitch* / $\sqrt{12}$. By doing so, significantly fewer readout channels are required, which considerably reduces the overall detector cost.

The "Gen-II" version of the LAPPD we envision using has an internal back-plane consisting of a resistive ground plane that collect the multiplied electron signal. The collected charge is subsequently spread through this layer and induces charge onto the readout pads of an external PCB, mechanically pressed against the outer surface of the borosilicate bottom panel of the tile.

Our initial goal is to measure the position resolution capabilities of the LAPPD coupled to an interleaved readout board. The apparatus is shown in Fig. 10, which includes the tile mounted to an external PCB with interleaved anodes. The setup also includes 420 nm laser light from a picosecond laser coupled into a fiber optical cable. Upon exiting the fiber, the laser light is focused by an aspheric, 20 mm focal length lens to produce a roughly 20 - 25 μm diameter beam spot on the LAPPD photocathode. The residuals from the reconstructed position of the beam spot will ultimately reveal the position resolution of the detector.

We have completed the assembly of the detector apparatus, including mounting the readout PCB to the LAPPD tile, installing the detector to a stand and into an enclosure to limit exposure of the photocathode to ambient light, and have organized the various optical elements onto an XYZ stage for the purpose of scanning the laser reference point onto different areas of the photocathode. A DAQ system composed of 256 channels of DRS4-based front end electronics (CAEN model: V1742 digitizers), with 5GHz digitization over 1024 samples has also been implemented within our RCDAQ DAQ software framework. Some initial results, showing signals recorded from a set of pads is shown below in Fig. 11 .

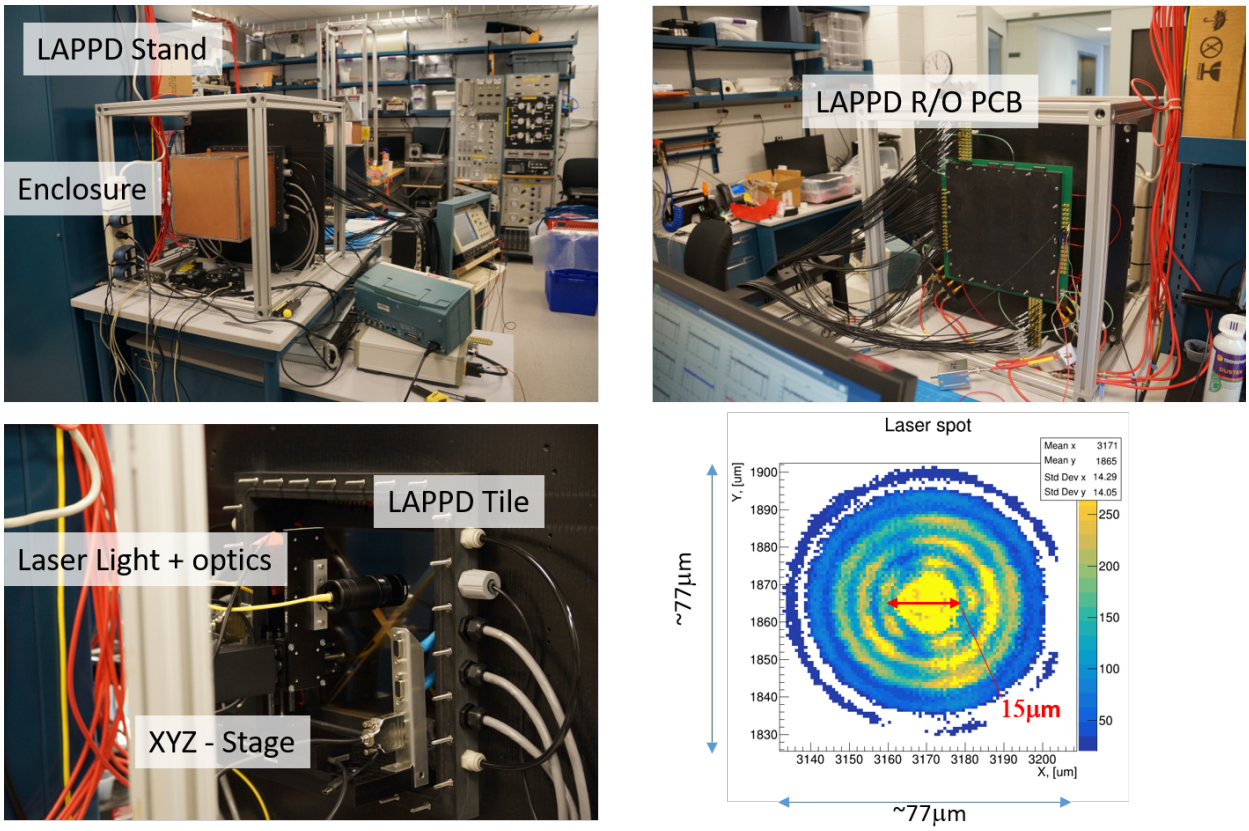

Figure 10: The LAPPD setup, including the mounting fixture, enclosure, optical components, and a reconstructed image of the focused beam spot using a 3.2 μm pixel CMOS camera.

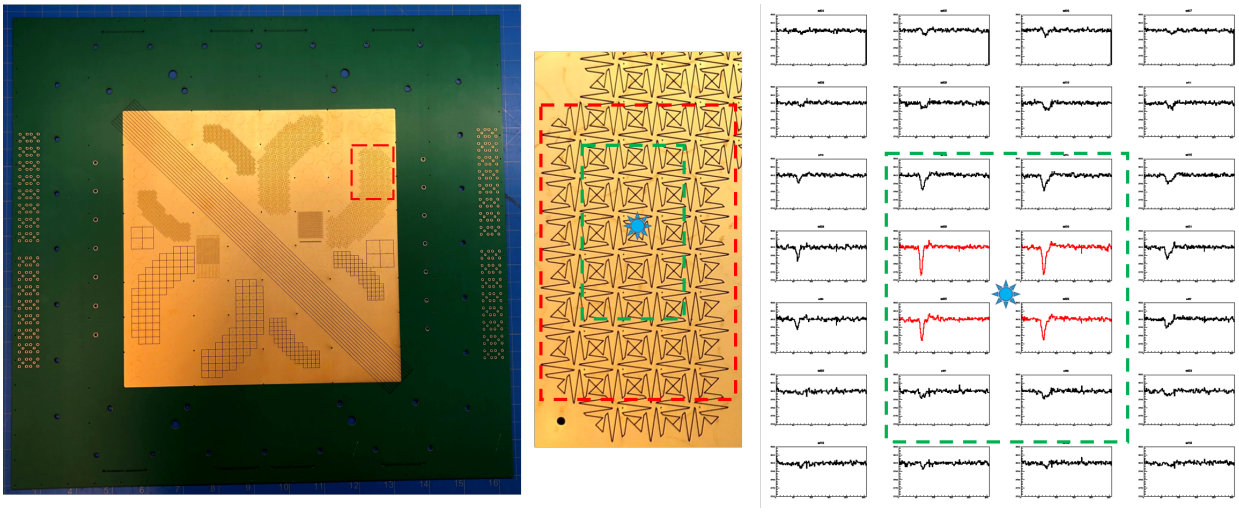

Figure 11: LAPPD readout PCB with pixelated and interleaved anodes. A subset of interleaved anodes is shown along with the corresponding digitized signals.

2.2.2 TPC studies at Stony Brook

Based on the simulation inputs [7], we developed a bipolar gating grid that we are planning to test in a strong magnetic field at the Argonne National Laboratory magnet facility. ANL provides an MRI magnet that can deliver fields up to B = 5 Tesla. In order to perform this test, we will have to include a wire plane on top of a four GEM stack in the prototype setup for a TPC.
Since it will not be convenient to open the TPC for swapping different configurations during the test, we have designed a PCB based pad plane to attach the wires and provide them with appropriate potentials via a routing scheme. Fig. 12, left, shows a schematic of the wire plane's active area matched to the as built GEM module design. Four different configurations (as shown in the color scheme) are implemented on the grid that can be tested simultaneously. The TPC prototype has its module arranged in a polar co-ordinate

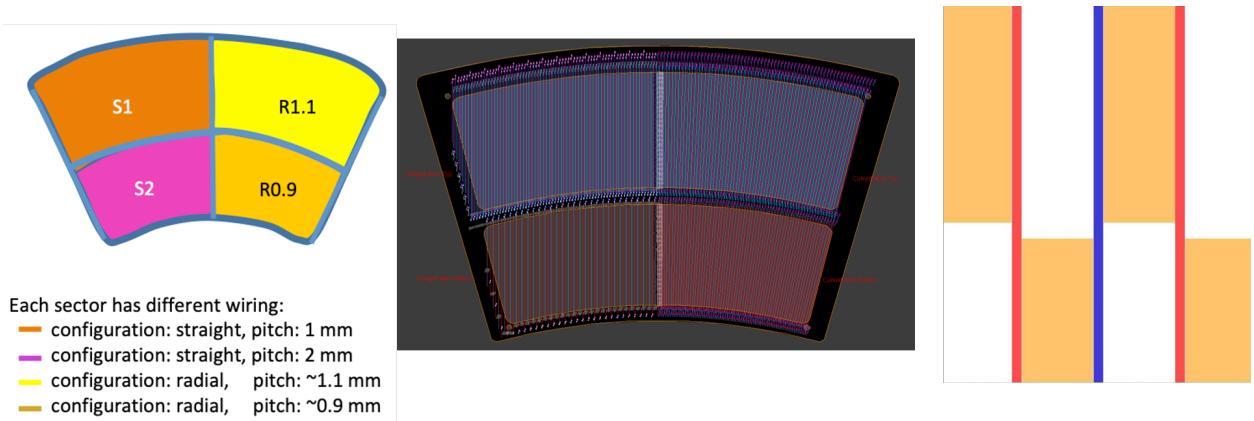

Figure 12: Left: Schematic of the wire plane active area. Middle: PCB for the mesh in the Eagle design automation program. Right: Zoom-in of the pad scheme.

system, which might pose a constraint for gating operation; the wires need to be parallel to each other for static gating operation. Therefore, we also want to investigate how much fanning out can be tolerated for such operation, along with different pitches for parallel wires in Cartesian coordinates.
Fig. 12, middle, shows a PCB design for wire planes from the Eagle electronic design automation program. The frame will be coupled with the TPC prototype.
One of the features of our designed board is the placement of connecting pads where the wires are soldered and glued (for mechanical strength). As can be seen in Fig. 12, right, the edge of such pads will serve for the purpose of alignment as $\sim 50\,\mu m$ wires are difficult to wind with precision.
We have ordered a set of PCB structures that accommodate the gating grid and are producing the final connections. As soon as the ANL magnet facility will we opening we will perform the tests. One of the structures can be seen in Fig. 13. The structures are presently in a processing unit that will stretch and bond the needed wires to the frame. The frame will eventually be attached to a quadruple-GEM module and inserted in a TPC prototype (see Fig. 14) which will be used in the ANL high-magnetic field facility.

Figure 13: Wire frame for the bi-polar passive gating grid structure. The frame is being equipped with the wires as described in the text.

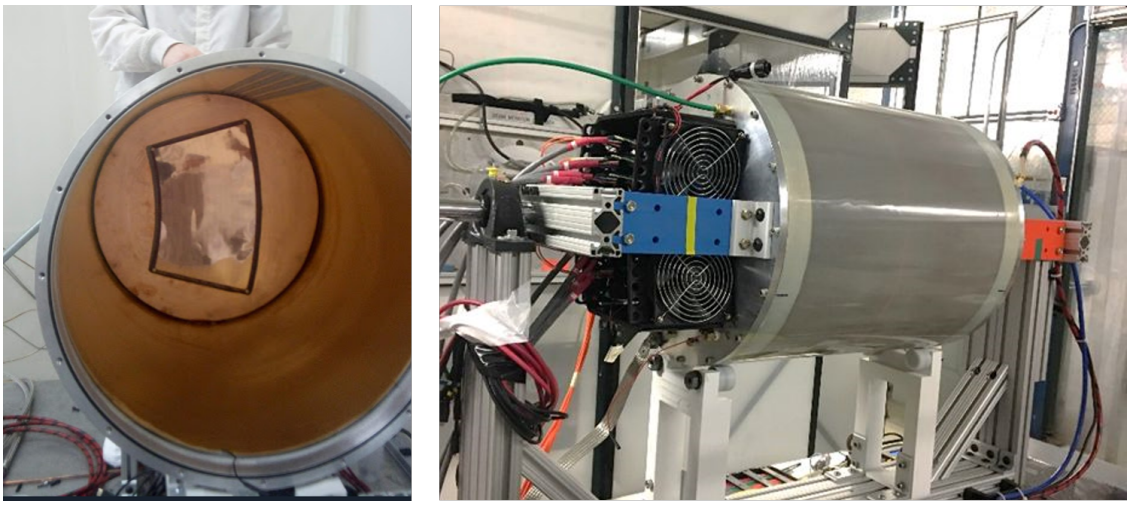

Figure 14: The TPC prototype for the sPHENIX TPC project. Left: view into the field-cage from the cathode side with a readout module at the anode side. Right: fully assembled TPC-prototype for the test-beam campaign.

2.2.3 TPC studies at Vanderbilt U.

MPGD R&D bench set up and study basic characteristics of MPGD detector : Fully equipped test bench for MPGD R$D was assembled capable for effective gain, IBF, energy resolution measurement for two to three different gas mixtures. Fig. 15 shows the MPGD R&D set up at VU for MPGD. Few basic studies on effective gain scanning and IBF blocking was done using standard 10X10 cm^2 active area quadruple GEM detector. The left hand side of fig. 16 shows the effective gain for quad GEM detector for different potential difference across each GEM while the right hand side of fig. 16 shows IBF for variable gap field configuration while keeping the effective gain of the quad gem detector constant. The results shows that one can reduce IBF by manipulating the field configurations across different gap regions of multilayered GEM detector.

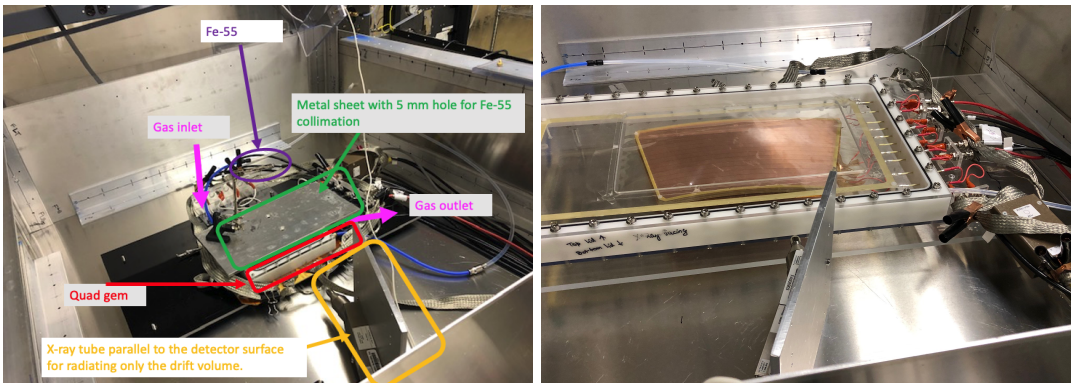

Figure 15: MPGD R&D set up at VU. **Left:** with standard 10X10 cm^2 active area quadruple GEM detector **Right:** With large GEM variable pitch and hole orientation quadruple GEM detector

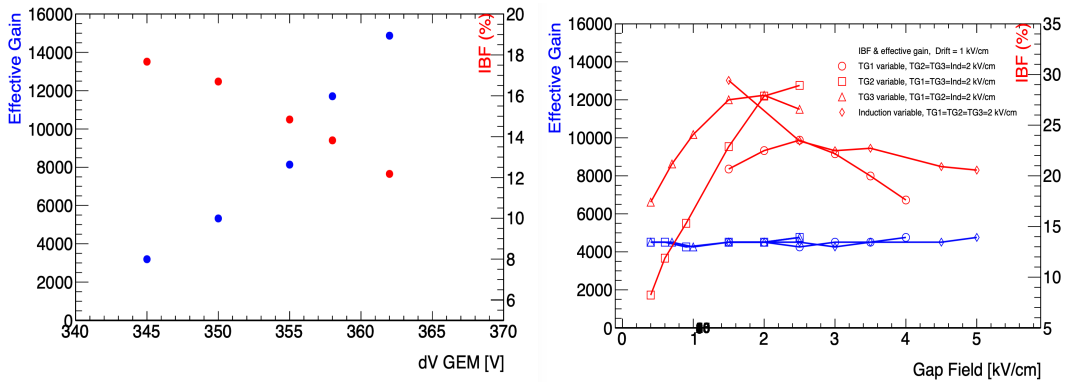

Figure 16: **Left:** IBF and effective gain for different voltages across each GEM in Quad GEM detector in $ArCO_2$-70:30 gas mixture using standard pitch (140 μm) GEMs. **Right**: IBF for different gap fields for the same quad GEM detector while keeping effective gain constant for all measurements.

Simulation studies : During this period simulation chain involving Finite Element Method and Garfield++ was set up for triple GEM and micromegas. Comparison of results for effective gain and IBF from simulation and experiment at Vanderbilt MPGD lab was done for triple GEM detector. Fig. 17 shows simulation results for triple gem detector. Similar simulation studies are ongoing for micromegas and also implementation of readout board of different strip pattern in collaboration with BNL and Yale University.

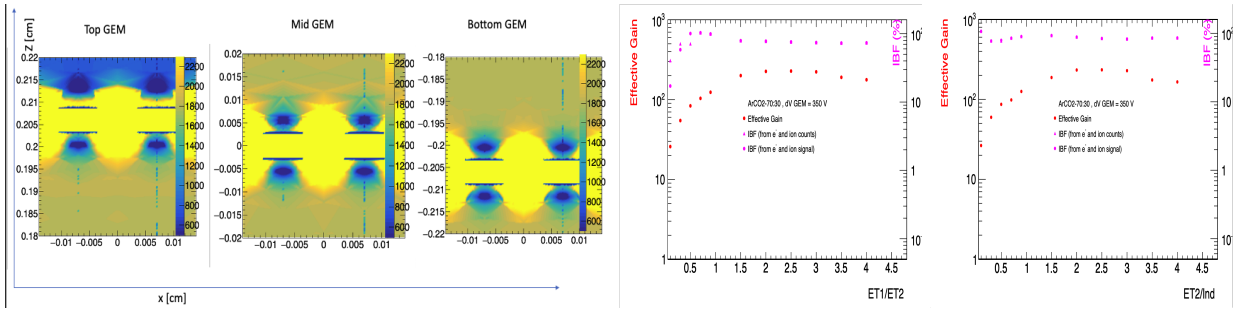

Figure 17: Simulation studies of triple GEM detector using Finite Element Method and Garfield++. Left panel shows one of the field configuration for different layers of triple GEM detector from Finite Element Method. Central and Right panel shows IBF and effective gain for triple GEM detector for different ratios of transfer and induction field

2.3 What was not achieved, why not and what will be done to correct?

2.3.1 TPC studies at Brookhaven National Lab and Yale Univ.

The R&D items that we were not bale to achieve are listed below:

1. We have not yet installed our new TPC zigzag PCB into our mini-TPC prototype for testing because there was a delay in preparing and testing the PCB. In addition, unforeseen modifications needed to be made to the mini-TPC vessel. We are now in a position to resume the assembly and should have the measurement completed over the coming months.
2. We have not yet tested the same zigzag TPC PCB outfitted with a Micromegas and μRWELL detector in our x-ray scanner since there was a delay in QA testing the boards before they were to be sent to CERN for processing. We expect to receive these boards by the end of March and can begin the planned measurements shortly thereafter.

2.3.2 TPC studies at Stony Brook

Ideally, we wanted to test the gating grid in hand at the high magnet facility at Argonne National Lab (ANL). However, due to the restrictions because of the pandemic situation our goal of getting to ANL has not been reached yet. We anticipate the opening of the lab to visitors over the coming months and will perform the tests immediately. We are in contact with the the responsible persons of the magnet facility at ANL.

2.4 What is planned for the next funding cycle and beyond?

2.4.1 TPC studies at Brookhaven National Lab and Yale Univ.

Our proposed R&D activity for the next funding cycle is as follows:

1. We plan to install our new zigzag TPC PCB coupled to a 4-GEM in our mini-TPC prototype to measure tracks produced by our TPC laser system and will compare these results to measured cosmic tracks. Time permitting, we also plan to test identical zigzag PCBs outfitted with Micromegas and μRWELL gain elements, as well as hybrid gain structures, namely 2GEM + MMG, and 2GEM + μRWELL in the TPC prototype.
2. We plan to use our high intensity, high resolution x-ray scanner to test each of the aforementioned gain structures, independent from the TPC field cage, to provide a baseline measure of performance.
3. We plan to continue characterizing the performance of various candidate TPC gas mixtures in the TPC prototype using a hybrid MPGD gain element.
4. We plan to continue investigating the performance of LAPPD detectors coupled to MPGD-style interleaved readout boards for use in various PID applications. In particular, we are interested in extracting high resolution position information from localized Cherenkov photons generated in the LAPPD window because this will endow this detector with high resolution tracking capabilities, providing some independence from other tracking systems.

2.4.2 TPC studies at Stony Brook

Depending on the outcome of the gating structure in the magnet setup we are planning to study optimization procedures for the device. In addition, we will be preparing for a coupled setup with a Micromegas/2-GEM

(MM2G) amplification device which was one of the suggestions from the last ACM meeting in July 2020. It is anticipated that the combination of a passive gating device coupled to a MM2G will provide the ultimate weapon to combat IBF in a TPC.

2.4.3 TPC studies at Vanderbilt U.

Vanderbilt University is planned to do experimental study of the effect of space charge on GEM , micromega , combination of GEMs and micromega energy resolution for different gas mixtures. Also study of MPGD based detector response under 0.8 T magnetic field will be done. Set up for using MPGDs in magnetic field is currently undergoing. Simulation study of different readout geometry will also be done with collaboration of BNL and Yale University under the Finite Element Method and Garfield++ simulation framework. Full Geant 4 simulation in Fun4All framework for EIC in both central and forward rapidity regions will be performed which will focus on tracking performance of different MPGD based detectors.

3 Full Barrel Tracker with Multiple Cylindrical Micromegas

3.1 What was planned for this period?

In the central barrel of an EIC detector, the vertexing detector can be complemented by a low material budget MPGD tracker instead of a TPC. CEA Saclay's goal is to study the feasibility and the impact of several concentric cylindrical layers of Micromegas tiles for the EIC detector.

Starting from the curved Micromegas technology that has been successfully deployed for the central tracker of the CLAS12 experiment at JLab, we planned to implement a detailed description of 2D readout Micromegas tiles in the fun4All framework. Using full Geant4 simulations, it was planned to study the tracking performance of different number and several arrangements of Micromegas layers.

We also planned to bulk a Micromegas on top of a large-pad capacitance-sharing readout board (see Sec. 4.1.3) and test its performance with a muon telescope.

3.2 What was achieved?

The performance of a Micromegas tracker solution has been tested with a full Geant4 simulation (using fun4All) of the reference EIC detector where the TPC has been substituted with a set of Micromegas layers. The silicon vertex tracker (SVT) consists of five layers of 10-μm resolution pixel detectors, based on the technology developed for the ALICE-ITS3 at CERN.

Each layer of the Micromegas tracker consists of 50 cm wide curved detector elements (tiles), long enough to cover the range $|\eta| < 1$. Each detector element is considered to have a 2D readout and the spatial resolutions both in the z and the $r \cdot \varphi$ directions are assumed to be 150 μm. The detailed implementation in simulation of each tile is based on the technology developed for the CLAS12 barrel Micromegas tracker: the material budget in the active area of each detector is about $\sim$0.3% X/X_0. The tiles in each layer are separated by a gap of about 2 cm of printed circuit board with a copper layer that mimics the routing of the readout lines back to the end caps.

Figure 18 shows a possible configuration of the MPGD tracker with six layers: two layers are placed at a radial distance from the beam pipe of about 50 cm and four layers are placed at about 80 cm. Several configurations have been investigated: one configuration with six layers equally spaced at regular radial intervals, one with three pairs of layers (inner, middle and outer pairs) and a configuration with two layers in the middle and four layers in the outer part of the barrel. Table 1 shows the radial position of the layers for the last two configurations.

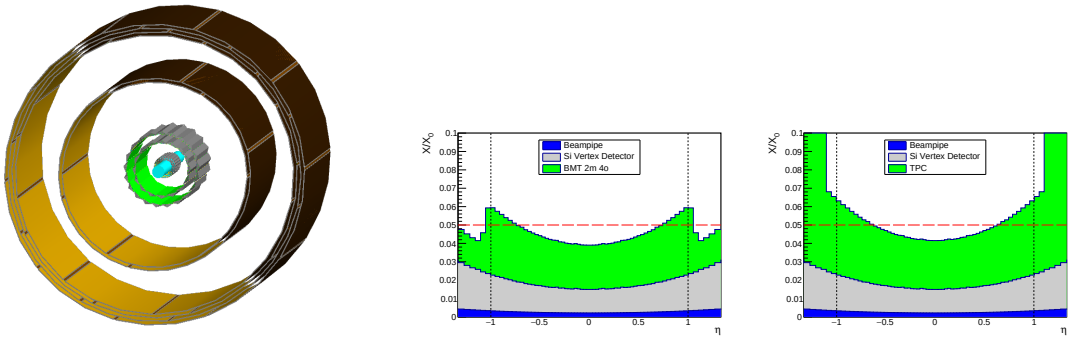

Figure 18: (left) A possible configuration of the cylindrical Micromegas tracker with two pairs of layers at mid way between the SVT and the four outer detector layers. The material budget of the hybrid detector with MPGD layers (center) is comparable with the one of the TPC solution (right). In the stack plots, the contribution of the beam pipe in blue, in gray the one of the silicon vertex detector and in green the MPGD tracker (or TPC) contribution.

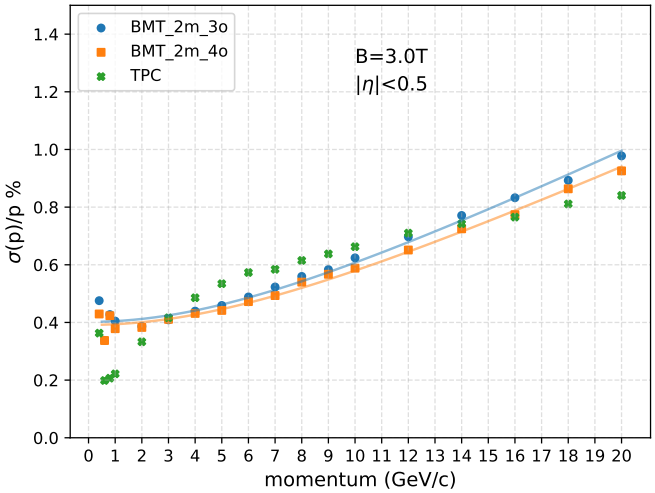

Figure 19: Relative transverse momentum resolutions of two hybrid detector configurations with Micromegas cylindrical layers compared to the configuration with the TPC. The configuration "2m_4o" is depicted in Figure 18. The "2m_3o" only has three layers in the outer region.

Studies of the relative momentum resolution have been performed by simulating five thousand π^- per momentum bin in the range $|\eta| < 0.5$ with a solenoid magnetic field of 3 T. The results for the configurations with two middle layers and three or four layers in the outer region are shown in Figure 19 together with resolutions obtained with the baseline hybrid TPC detector.

The hybrid detectors studied (TPC and BMT) show similar relative momentum resolutions overall, with the hybrid TPC solution performing better at very low momenta and at higher momenta, while the hybrid BMT solution being better in the momentum range $3 < p < 12$ GeV/c. In particular, both detectors will meet the requirements in momentum resolution, set by the physics needs, of $\sigma(p)/p = 0.05\% + 1\% \cdot p$.

Layer	Radial position
0 inner	198 mm
1 inner	217 mm
2 middle	477 mm
3 middle	496 mm
4 outer	719 mm
5 outer	736 mm
6 outer	756 mm
7 outer	775 mm

Table 1: Radial position of Micromegas tracker layers used in the hybrid detector simulation

3.3 What was not achieved, why not and what will be done to correct?

The study of the capacitance sharing large pad readout with a Micromegas has not started yet. We have to finalize the funding assignment to CEA Saclay and in the meanwhile we will pre-order a couple of PCBs from CERN.

3.4 What is planned for the next funding cycle and beyond?

Although the current technology of curved Micromegas meets the requirements for physics, we aim at investigating a detector solution that reduces even further the material budget and, at the same time, simplify the production chain (possibly reducing also the costs). This R&D will focus on a modular detector design based on flat tile. Such a solution will allow:

- the reduction of the thickness of the materials in the active region: due to mechanical stability, curved detectors can only be made out of FR4 of $\sim 200\mu$m, while in a flat geometry the mechanical load is taken care of by the support structure, allowing for the use of thinner materials;
- the simplification of the production: curved detectors impose the use of specific sizes and tools for each curvature radius, thus making the production line more complicated and more expensive;
- a higher production rate: excessive large area detectors require numerous tooling to handle and control the mechanical precision, while a small size modular detector can be produced faster and with simpler quality assurance tools.

We plan to integrate this concept in the full Geant4 simulation to study its performance and to understand the impact of the structure on the total material budget. We plan to build a small prototype as a demonstrator.

In parallel, we plan to optimise the readout patterns and the resistive material of the Micromegas to meet the required spatial resolution in both directions.

4 Fast Tracking Layer in Barrel Region with Cylindrical μRWELL

4.1 What was planned for this period?

4.1.1 Cylindrical μRWELL studies at Florida Tech

The Florida Tech group is focusing on developing the mechanics for the first functional cylindrical μRWELL prototype. Sealing the gas volume will be one of the critical technical issues to be addressed. The work

with our mechanical mock-up initially showed that it is difficult to assemble the detector with the O-rings in place. We planned to investigate this further as well as what the most reliable way is for splicing the edges of the foils together to form continuous leak-tight cylinders. We planned to review the design and investigate the optimal material choice for the end-rings in light of the required precision. Given the simulation results on the material estimate for the current mock-up, we wanted to attempt to reduce material in the end-rings. The suspension of the cylindrical structure with nylon rods was to be tested with respect to its long-term stability.

Following a recommendation from the last review meeting with the Advisory Committee in July 2020, we also planned to focus on a detailed quality control study of the mechanical mock-up.

4.1.2 Cylindrical μRWELL studies at TU

For this cycle we had planned to:

1. **Build 10 cm $\times$ 10 cm planar μRWELL μTPC prototype:** Build and characterize a 10 cm $\times$ 10 cm planar μRWELL operating in μTPC mode without implementing a TPC field cage. This detector would be characterized in the TU detector lab using current electronics and DAQ, as well as a future beam test.
2. **MPGD Simulation:** Continue building off our work done for the EIC Yellow Report, implementing gas tracking into an EIC detector for realistic simulations. This includes forward/backward planar trackers (see Sec. 5.2.2) and cylindrical central tracking layers which reflect ongoing designs and material budgets.
3. **Cylindrical μRWELL prototype:** Collaborating with FIT and UVa colleagues in designing, constructing and testing a cylindrical μRWELL prototype detector (see Sec. 4.1.3).

4.1.3 Cylindrical μRWELL studies at UVa

For this cycle, we planned to:

SRS-VMM readout electronics: Set up the SRS-VMM readout electronics and associated DAQ and decoding software and test the system with GEM and μRWELL prototypes.

Characterization of μRWELL prototype with X-Y strips: Characterize the prototype in the x-ray at UVa and in beam test at JLab and FNAL to finalize spatial resolution and response uniformity studies.

Development of High-Resolution Capacitive-Sharing Anode Readout for MPGD detectors: Finalize the performances studies of the triple-GEM with large-pad prototype described in appendix B.2 and develop a μRWELL detector prototype with similar large-pad readout PCB. We have also identified two areas where further R&D are required to fully validate the concept.

- **Proof of concept of capacitive-sharing readout with μRWELLs:** μRWELL amplification structure is quite different from GEMs. A dedicated R&D is required to demonstrate that the concept work equally with μRWELL and optimize of the readout design to μRWELL technology.
- **Minimisation of the capacitance noise and cross-talks:** Investigate new ideas to minimize the capacitance induced noise and cross talk effect of large pads. Study different pad geometries and patterns as indicated on the sketch of Fig. 65 in the appendix B.3.

Design and construction of a small size cylindrical μRWELL prototype: Join effort with the Florida Tech. and Temple U. colleagues to build and characterize a fully functional small prototype cylindrical μRWELL detector. In this project, the UVa group will be in charge of the overall design of the μRWELL amplification layer, the drift cathode foil as well as readout plane. With Florida Tech taking responsibility of the mechanical support structure and Temple U. the readout electronics. the readout plane for this prototype is anticipated to be based on the capacitive-sharing readout concept described in appendix B.2 with a pad size somewhere between 1 to 2 cm^2 with a fall back option being the U-V strip readout developed and tested with UVa planar large GEM. We envisioned to complete the designing phase and fabrication of the μRWELL parts by spring 2021 and then followed up by the assembly into detector and preliminary tests jointly performed by the 3 institutes in the second half of FY21.

4.2 What was achieved?

4.2.1 Cylindrical μRWELL studies at Florida Tech

Mechanical Mock-up for a Cylindrical μRWELL Detector: We have further developed the mechanics for a cylindrical μRWELL detector using the mock-up introduced in the last report. We continue using a 10 mil (250 μm) Cirlex Kapton foil that wraps around the innermost 3D-printed frames to simulate the μRWELL foil. The frames in the three-piece endring assembly have radial holes, which can be used for compressing the endring assembly with closing screws, as well as embedded nylon nuts to hold axial threaded nylon rods which in turn are used to mount the mock-up. The other ends of these low-mass nylon rods are inserted through holes into a plexiglass "endplate." We then cap the endplate with nuts to fix the rods in place and apply axial tension as desired to hold the mock-up (Fig. 20).

In this latest iteration, a few new elements have been incorporated into the mock-up. Metal wires have been added which allow hanging the mock-up from a central bar above the mock-up as an alternative low-mass mounting method. The wires wrap around the extended barrel of the inner frames, which is primarily intended to serve as the base for mounting the readout electronics (Fig. 21 left). No tension in the Z-direction can be applied in this configuration, but it significantly reduces material and can make the plexiglass endplates obsolete. We now use a 5 mil (125 μm) Kapton foil on the outside of the model to stand in for the drift foil because the previous 2 mil (50 μm) version tended to crease under axial tension (see last report). This thicker foil now produces a smooth outer cylinder as desired. To form the cylinder, the two foil ends are spliced together by overlapping them for 1-1.5 cm and simply attaching them to each other with 2 mil adhesive Kapton tape. The outer 3D-printed closing frame in the endring assembly has been replaced by a metal strap which can be tightened using a worm drive (Fig. 21 left). The variable circumference of this metal strap alleviates previous concerns with the diameter of the outer frame being too small to properly fit around the rest of the mock-up. The outer metal strap also provides near-even tightening around the circumference, which helps with uniformly compressing the embedded outer O-ring for sealing the gas volume. However, we observe that at the position of the worm drive the strap does rise up somewhat from being flush against the surface to support the drive (Fig. 21 center). While this appears to be an attractive solution for fixing the outer ring in place from a mechanical point of view, it adds material to the budget. Also, fixing the inner frame and the middle frame together in place still needs optimization.

Quality Control of the Mechanical Mock-up: To quantify the conformity of the "drift" foil cylinder to the design parameters, i.e. how closely its cross section matches a circle, we use a plexiglass plate with a circular cut-out that matches as closely as possible to the measured average circumference of the foil. This serves as a reference template for a "perfect circle." The plate is cut precisely with a laser cutter and the hole has a diameter of 19.84 cm. The reference plate is then installed within the slots of 80/20 bars and moved along the axial Z-direction of the mock-up, which allows us to measure the gaps between the foil and the inner surface of the plexiglass hole at different Z-positions. We take measurements every 10 degrees in azimuth around the circle for two different axial Z-positions, i.e. at one of the ends of the mock-up and in its center. The gap sizes are measured for two configurations; one with and one without tension applied with

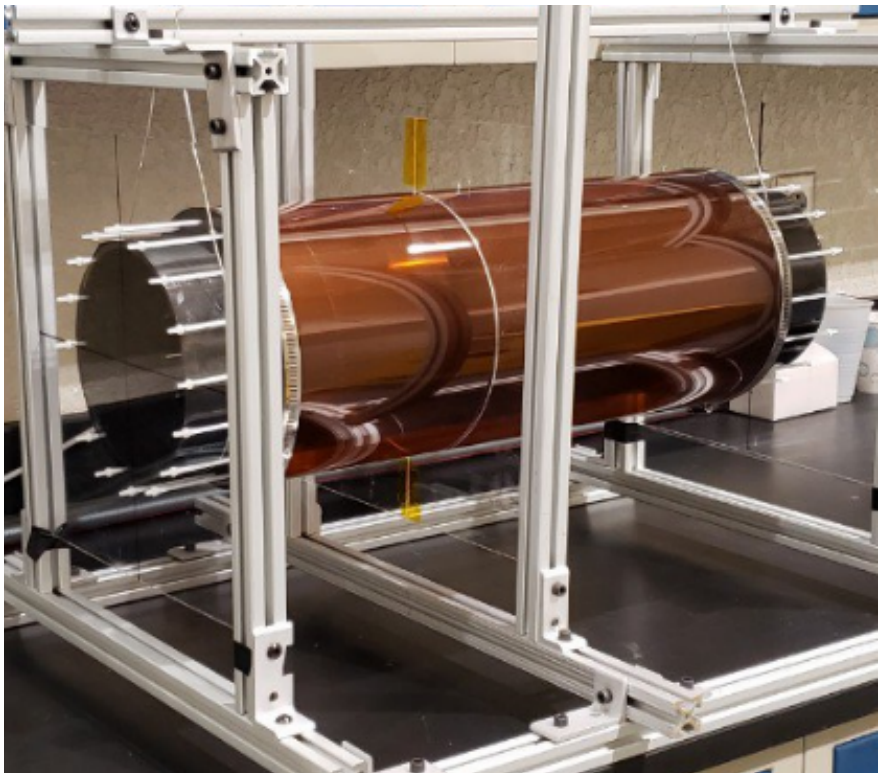

Figure 20: Current configuration of the mechanical mock-up for a cylindrical μRWELL detector, with an additional auxiliary "scanning" plexiglass plate installed near the center for quality control measurements.

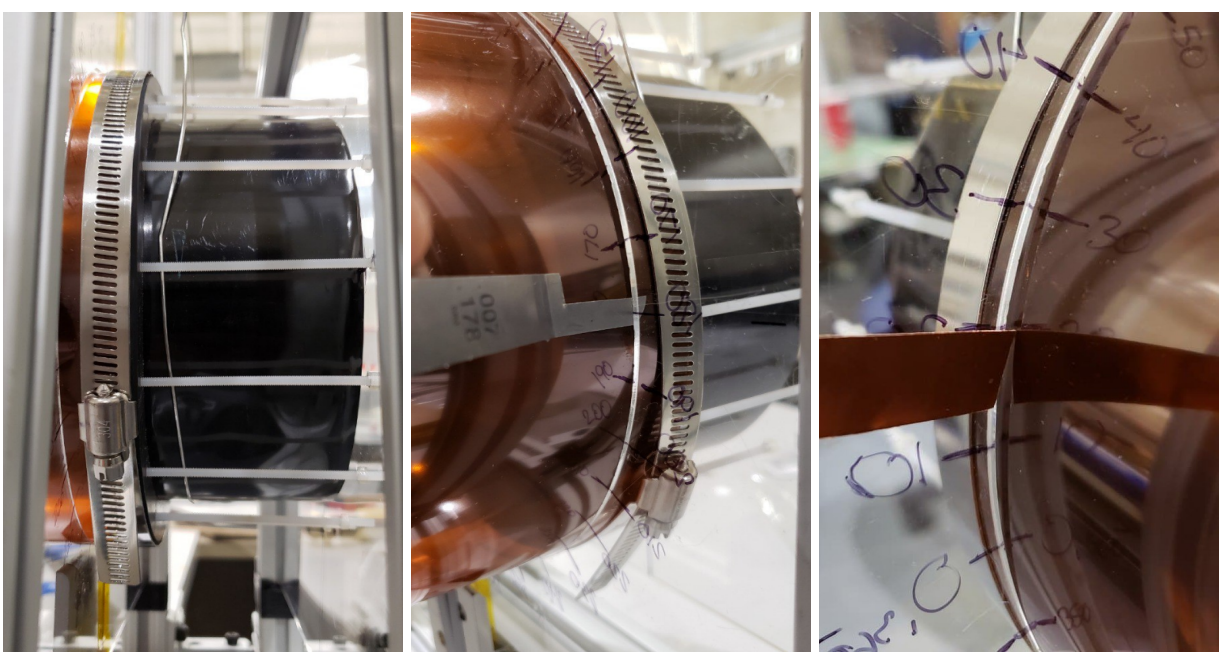

Figure 21: Left: Metal strap with worm gear used as a new closing mechanism for the endring assembly. Center: Modified feeler gauge used for measuring very narrow gaps. Right: Copper tab marked off for measuring larger gaps where use of the feeler gauges was not practical.

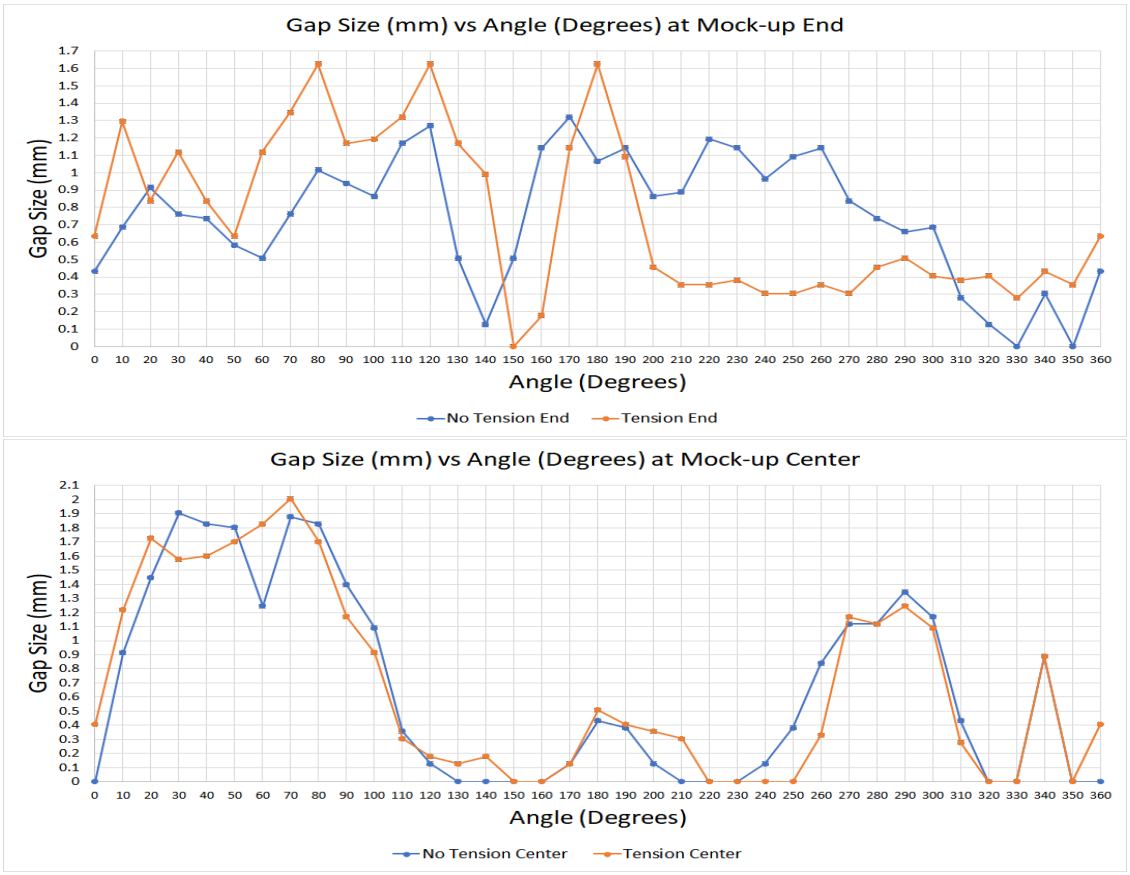

Figure 22: Preliminary results from measurements of gap sizes between outer drift foil and circular plexiglass template vs. azimuthal angle. The zero-degree position here corresponds to the right direction in the vertical plane as seen from one of the cylinder ends. Cylinder top and bottom are at 90° and 270°, respectively. Top: Gap sizes at one cylinder end, with (orange) and without (blue) tension. Bottom: Gap sizes at cylinder center, with (orange) and without (blue) tension. Note: Error bars are present in the plots, but not visible because the uncertainties of 0.013 mm in gap size and 0.5^o in angle are smaller than the marker sizes.

the nylon rods. For the configuration with tension, the closing nuts are rotated fully three times for each nut on both sides of the mock-up (Fig. 20). To measure the gap size, a combination of feeler gauges (modified to increase precision in measurement) and copper tabs (where a mark is placed at the gap width and then measured with calipers) is used (Fig. 21 center and right).

As can be seen in the plots in Fig. 22, the cylinder is not perfectly round. The gap sizes range from 0-2 mm. As the cylinder has a diameter of 198 mm, this represents a max. distortion on the order of 1%. The distortions at the end and in the center are markedly different. At the end, the shape is presumably dominated by the shape of the endring assembly, whereas in the center gravitational sagging plays a stronger role. We note that the 3D-printed frames have some intrinsic distortions in roundness due to material shrinkage after printing. We attempted to correct this by machining the parts, but these still contribute to some degree to the measured cylinder distortions. We find that the largest gaps occur near the top and bottom in the cylinder center. This indicates an elliptical cross section shape with the long axis near the horizontal and the short axis near the vertical direction. Based on these measurements, we see that applying tension does change the shape, but not dramatically. Tension appears to affect the shape more at the end than in the center.

We briefly discuss distortions at some specific angular positions. The seam joining the two ends of the "drift" foil is located near 340°, where a small spike in gap size is visible in the data. As one would expect, this

point, where the two ends of the foil overlap, causes a non-uniformity in the roundness of the mock-up; however, it is not particularly larger than the other non-uniformities around the cylinder. We conclude that the splicing does not present a major problem. The worm drive of the metal strap on the tested end is located at 150°. The worm drive is 3 cm in length and covers 17° in azimuth. Interestingly, the measured gap sizes are fairly small at that position, which suggests that the drive does not unduely distort the frame.

Impact Estimate and Conclusion: The observed variation in radial cylinder size along the azimuth impacts the size of the drift gap, which in this mock-up is on the average 15.8 mm as given by the thickness of the middle spacer ring in the endring assembly. This means that we observe a max. variation in the size of the drift gap on the order of 2mm/15.8mm = 12.7%. For a larger drift gap size, the relative variation would be proportionally smaller. If the drift is designed as a single, contiguous electrode, then the electric field in the drift gap will vary by the same amount of max. 12.7% around the azimuth if a single voltage is applied. This will in turn create a variation in drift velocity around the azimuth.

We conclude that the detector should be operated on a plateau of the v_{drift} vs. E curve to minimize the impact of the foil distortions. This will have consequences for the choice of gas and the high voltage to be applied. It could be an option to segment the drift electrode and apply slightly different voltages on the segments to compensate for the mechanical distortions if needed. Consequently, a detailed simulation study of geometry, electric field, drift velocity, and angular resolution of reconstructed track stubs using the mini-drift (μTPC) mode will be needed for moving towards a full technical design report for this subdetector.

4.2.2 Cylindrical μRWELL studies at TU

1. **Small planar μRWELL detector:** Although this project has and continues to face delays, we have made some progress. We have procured our 10 cm × 10 cm μRWELL from CERN. This detector is based on the standard μRWELL material budget, and is equipped with a Compass style readout boards. The detector will be operated in the μTPC mode with a drift gap of 15mm with no field cage. Figure 23 shows various assembly stages of the μRWELL detector in our class 1000 clean room. We plan to initially

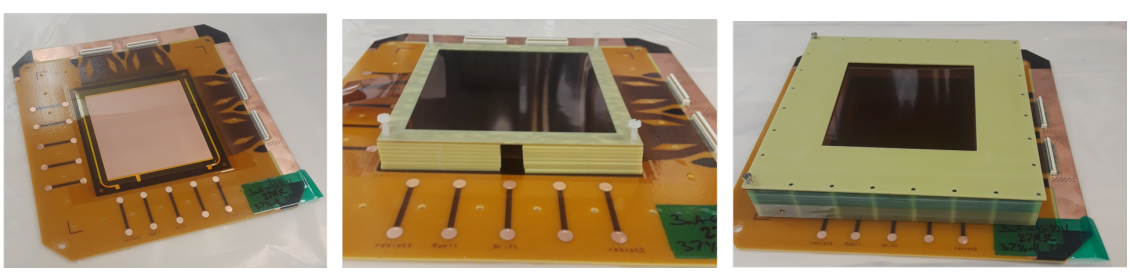

Figure 23: The figure shows various assembly stages of the μRWELL detector including the μRWELL (left), μRWELL with the 15 mm spacer stack, and HV cathode (center), and the full μRWELL with gas enclosure (right).

   assess the performance of the μRWELL using our detector lab at Temple University via cosmics and ^{55}Fe in combination with the SRS DAQ and APV25 chips. A 10 cm × 10 cm triple-GEM detector is being integrated into our setup to provide a direct reference for the μRWELL performance. Figure 24 shows our cosmics test stand setup. Calibration and QA of the system and GEM performance is ongoing.

2. **MPGD Simulation:** TU along with FIT have two new graduate students (Athira Kunnath Vijayakumar from TU and Merrick Lavinsky from FIT) who are becoming familiar with the EIC Fun4All simulation framework. One of their initial goals was to implement the GEM trackers found in EicRoot simulation framework, which have a realistic material budget based on SBS GEM tracker, into the Fun4All framework. They have now successfully imported this geometry into Fun4All and are verifying the material budget and proper integration into the simulation framework (see Sec. 5.2.2).

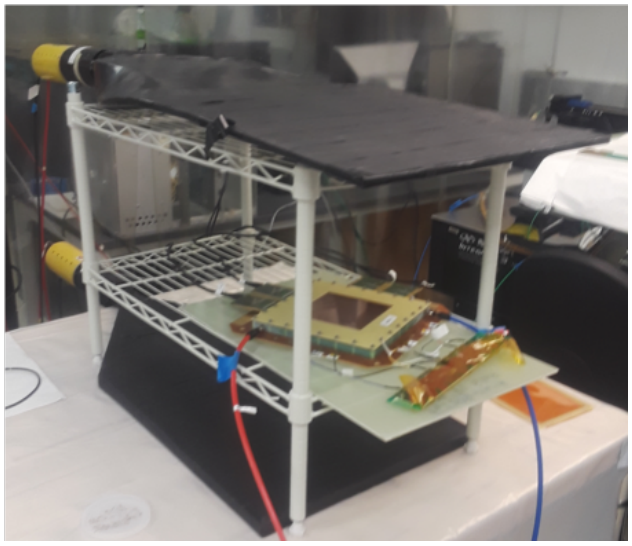

Figure 24: Shown is our cosmics test stand with two scintillator paddles to trigger on coincident cosmic events and a triple-GEM detector located between the two paddles.

4.2.3 Cylindrical μRWELL studies at UVa

Performance of large-pad capacitive-sharing readout

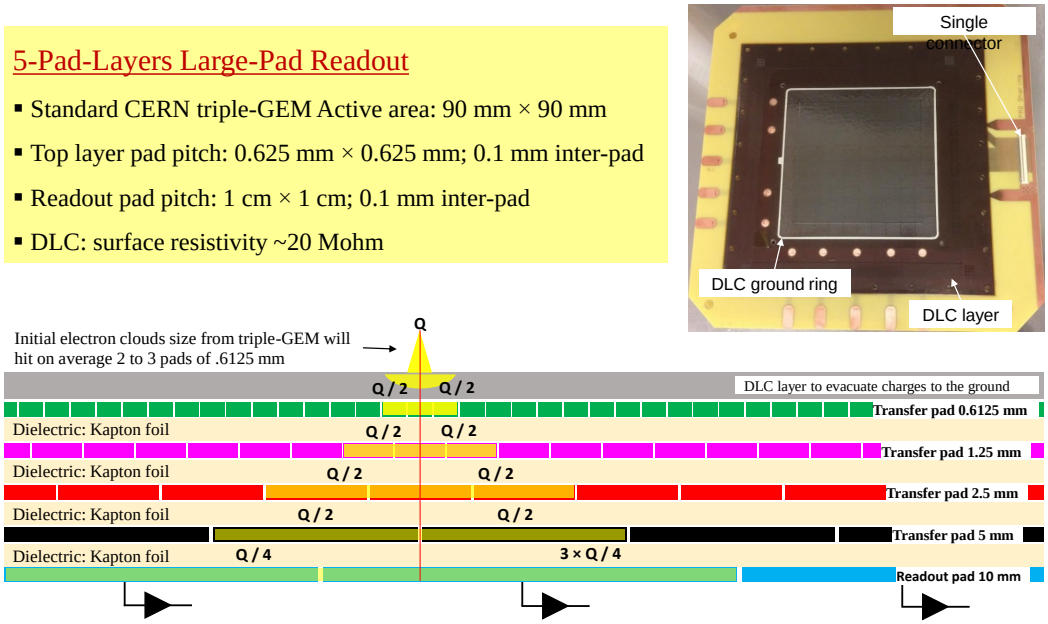

Figure 25: **Top:** Cross sectional view of large-pad capacitive-sharing readout prototype under study at UVa. **Bottom right:** picture of the readout board before assembly in a triple-GEM detector

Beam test setup in Hall D at Jefferson Lab: We are pursuing the characterization of the GEM prototype assembled with the large-pad capacitive-sharing readout size shown on Fig. 25. The prototype with 1 cm × pad readout board have been installed in beam test in Hall D at Jefferson Lab in Fall 2020 to

study response linearity and spatial resolution performance of the board. The Hall D test setup consisted of a GEM trackers telescope with the large-pad capacitive-sharing triple-GEM prototype sandwiched between two pairs of standard X-Y COMPASS triple-GEMs providing high accuracy tracks information. The telescope was installed in the electron arm of Hall D pair spectrometer (PS) as shown on Fig. 26. The electron beam characteristics are shown on Fig. 54 and 55 in appendix B.1. The APV25-based Scalable Readout System

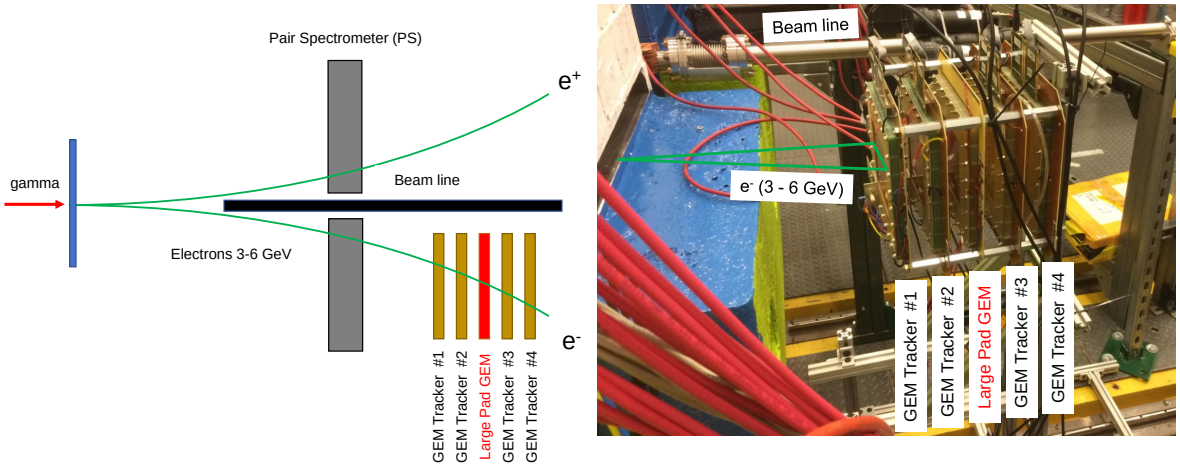

Figure 26: Setup of the capacitive-sharing pad readout prototype with 4-GEM trackers in the electron arm of Hall D Pair Spectrometer at JLab

(SRS), triggered with a NIM signal provided by HallD GlueX detector trigger system was used for the read out of all five GEM detectors. The trigger rate was limited to 400 Hz because of the limitation of SRS DAQ software running in a standalone mode a part from the general Hall D DAQ system. A significant amount of data were collected for HV scan runs to study efficiency, average cluster size and spatial resolution of the large-pad capacitive-sharing readout.

Detector efficiency vs. HV: HV scan was performed, varying the average voltage HV (V) across the GEM foils from 338 V to 374 V. Typical COMPASS triple-GEM operating at full efficiency with an average voltage equal to HV = 374 V. The efficiency is track-based, i.e. for each event, a track is reconstructed from hits in 3 COMPASS X-Y GEM trackers of the setup and we look for hit in the large-pad capacitive-sharing prototype within a 2 mm radius of the predicted hit from the reconstructed track. The efficiency is the ratio between the number of hits in the prototype and the number of predicted hits from the tracks for each HV run. The plot on the left of Fig. 27 shows the efficiency curves as a function of HV (V) with full efficiency plateau reached at 365 V. The red dots curve shows the efficiency when there is no requirements on the minimum number of pads used to form the event's cluster. For black dots curve, a minimum of 3 pads above threshold is required for a cluster to be valid. For high gain at at HV *geq* 360 V, the efficiency for both 1-pad minimum and 3-pad minimum data. This means that for this 1 cm $\times$ 1 cm size pad readout, even small signal created in the triple GEM from the MIP results to charges been shared by at least 3 pads on the readout. Charge transfer from the top layer to the readout pads of the bottom layer preserve charge sharing information even for low signal MIP event. This is a clear validation of the concept of capacitive-sharing scheme. Similarly, the study of the efficiency as a function of the threshold applied for pedestal cut on the right of Fig. 27 reveals that for low low level of threshold below 2 $\times \sigma_{\mathrm{rms}}$, there is no difference in the efficiency between the 3-pads minimum requirement and no requirement is applied to the pad cluster during the analysis. Above 2 $\times \sigma_{\mathrm{rms}}$, the efficiency starts dropping with the 3-pads minimum requirement on the cluster from 94% to 86% at 5 $\times \sigma_{\mathrm{rms}}$, while it remains as high as whereas it just drops slightly below 94% at

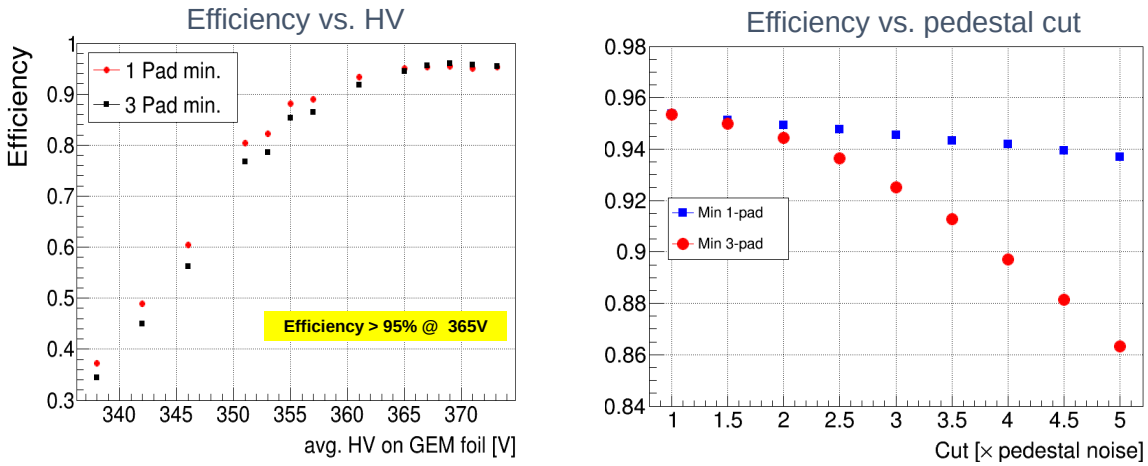

Figure 27: **Left:** Efficiency as a function of the average HV on the GEMs with a minimum cluster size requirement of 1 pad (*red*) and 3 pads (*black*). **Right:** Efficiency as a function of the zero suppression cut with a minimum cluster size requirement of 1 pad (*blue*) and 3 pads (*red*).

$5 \times \sigma_{\mathrm{rms}}$, when no requirement is applied to the cluster. This results is also expected as when the threshold for pedestal cut is higher, pads neighboring the central pad of the cluster with small ADCs are cut out of the cluster. More detailed studies of the pad cluster definition as well as the cluster size analysis are reported in appendix B.1. In the remaining part of this report, we are focusing our attention in the detector response and the spatial resolution performance of the large-pad capacitive-sharing readout prototype

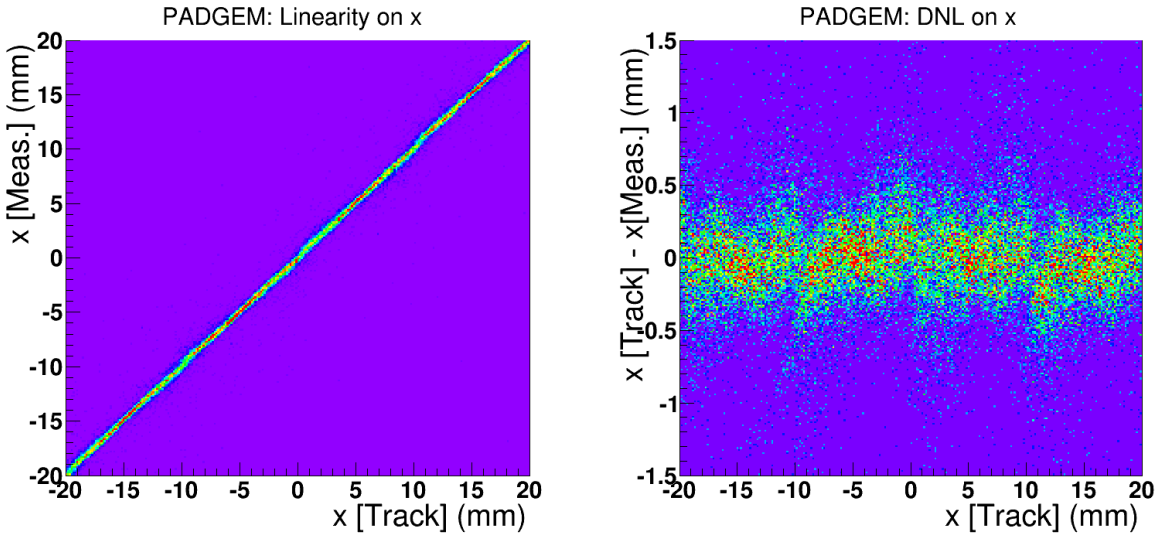

Figure 28: ***Left:*** Correlation between the position coordinate in x from the capacitive sharing prototype and the expected x-coordinate position from the track fit from the GEM trackers of the Fig. 26 setup; ***Right:*** Differential non linearity as a function of the position along x

Detector response linearity: The left plot of Fig. 28 shows good the correlation between the predicted x-coordinate of the particle position from the reconstructed track at the z location of the capacitive-sharing

pad-GEM prototype and the measured x-coordinate using the pad readout. The position correlation plot is shown here only on the x-direction because of the large spatial range of the electron beam as shown on 55 appendix B.1, however the same performance is expected in the y-direction. The differential non-linearity (DNL) in x-direction is shown on the right plot Fig. 28 showing a periodicity of 1 cm corresponding to the pad pitch of the readout structure. For the detector linearity response as well as the spatial resolution analysis, we have limited the range to [-20 mm, 20 mm] to eliminate the edge effects caused the large average cluster size $\geq$ ¿ 3 on large pad (1 cm $\times$ 1 cm pad size) readout structure that will distorts the detector response on the edge. This is because with such large pads (1 cm $\times$ 1 cm pad size) and cluster spread over more than 3 pads, the edge would affect the analysis. No other selection cut such as cut on the angle of the incoming particles was applied for the analysis. Moreover, we did not implement any correction algorithm in this analysis to compensate for the DNL. Improvement of the detector response linearity and spatial resolution could be expected by implementing additional cut and some algorithm corrections based on the DNL pattern information.

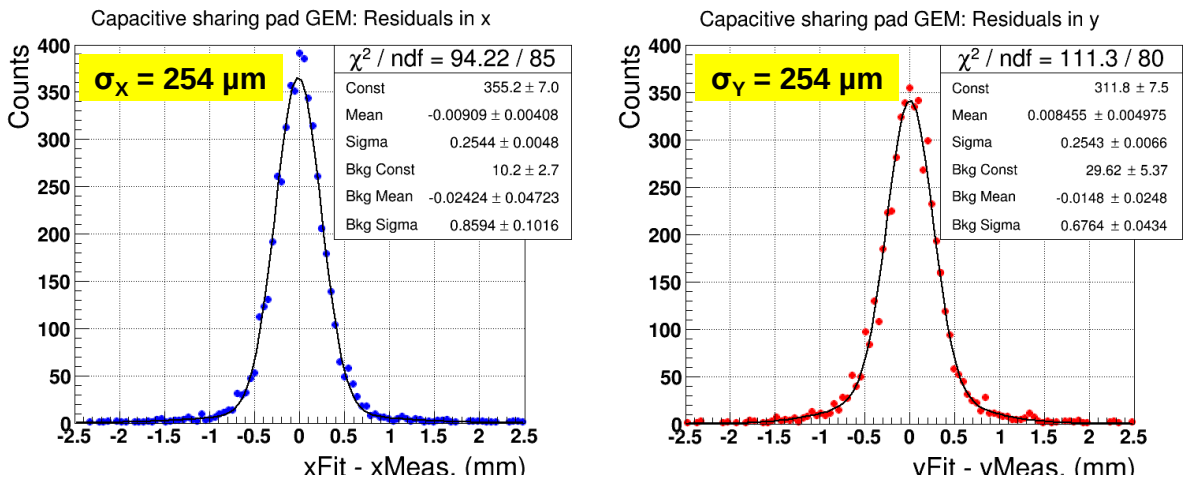

Figure 29: Spatial resolution in x (*left*) and y (*right*) for 1-cm pad readout prototype; no minimum ADCs requirements for the central pad.

Spatial resolution performance: We use simple 2D centre of gravity algorithm to calculated x and y coordinates of the particle position from the pad cluster as defined in appendix B.1. Track residuals in x and y from the hall D beam test data are shown on the plots of on the Fig. 29. The data are fitted to a double Gaussian function and spatial resolution is defined as the width ($\sigma_{x/y}$) of the main Gaussian distribution. Detailed studies of spatial resolution studies with the cluster pattern and HV on the GEM and pedestal cuts are reported in the appendix. Cluster pattern #3 as defined on Fig. 56 in B.1 was the one with the optimized resolution performances. The plots shows a spatial resolution of 250 μm for both x and y directions. These analysis was performed with no specific cut or offline correction to the data other than the one described in the section 4.2.3 above. The results are quite remarkable for 1 cm $\times$ 1 cm pad readout. Without charge sharing capability, 1 cm $\times$ 1 cm pad readout would yield a spatial resolution in the order of 1 / $\sqrt{12}$ $\sim$ 3 mm which is about 12 time higher than the results we obtained with the capacitive sharing using simple 2D centre of gravity algorithm without any additional correction. Moreover, this first capacitive-sharing pad readout prototype has some limitations with sub-optimized pad geometry design leading to higher capacitance noises and cross talk because of the large width ($\sim$ 100μm) of the traces connecting the pads to the readout connectors. We have already discuss way to significantly improve the readout design to minimize the noises and cross talk effect in order to achieve better spatial resolution performances with the large pad size. Fig. 30 shows better spatial resolution performances when a minimum charges of 1000 ADCs is required for the central pad of the cluster. We observe a clear improvement of the spatial resolution in both x and y with this requirement. The resolution improves from 254 μm to 212 μm in the x-direction. The improvement is even more pronounced for y-resolution from 254 μm to 187 μm.

The difference between the two x and y can be explained by the different angular distribution in x and y of the incoming tracks as shown on Fig. 55 in appendix B.1. We expect a degradation of the resolution performances with the larger angle of the incoming particle. The significant improvement resolution with the requirements on the central pads suggests that performances would be improved by operating the triple-GEM detector with large-pad capacitive-sharing readout at a higher gain. We will perform further studies in beam test to evaluate the best detector gain that provides the optimal spatial resolution for these type of readout. The studies will be repeated with μRWELL detector to optimize the readout specifications with μRWELL amplification structure which is quite different from triple-GEM.

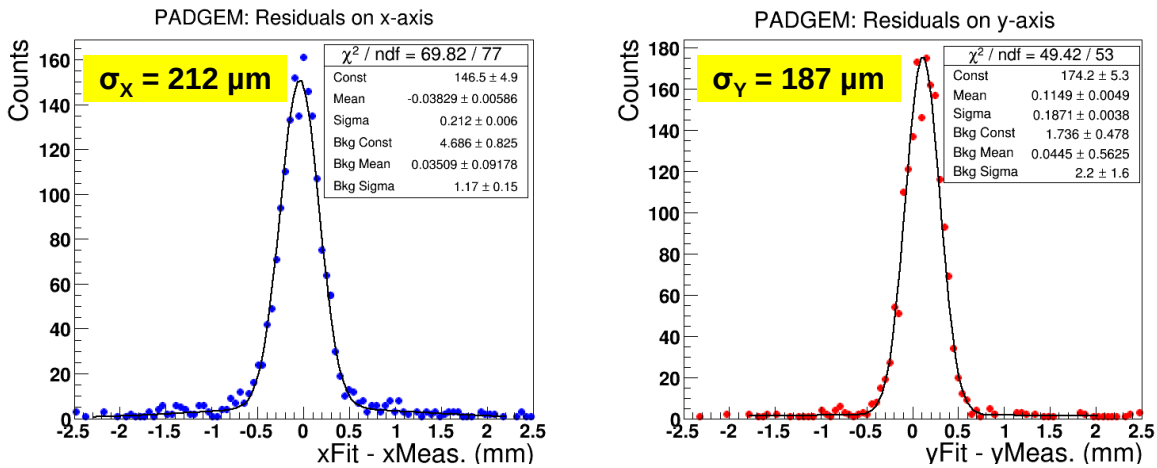

Figure 30: Spatial resolution in x (*left*) and y (*right*) for 1-cm pad readout prototype; minimum $\geq$ 1000 ADCs for the central pad.

Development of high resolution capacitive-sharing readout

We have developed a couple of capacitive-sharing readout PCBs in collaboration with CERN PCB workshops experts to extend further the studies of this new readout concept. We have already received to capacitive-sharing readout boards from the CERN we are in the process of assembling them into triple-GEM detector. The characteristics of the first PCB are shown on Fig. 31. It is a 5-layers large-pad readout board, similar to the first prototype tested (see section 4.2.3). The top pad layer has a pad pitch of 0.5625 mm $\times$ 0.5625 mm and the readout pad layer at the bottom a pad size of 9 mm $\times$ 9 mm. The board is segmented into four quadrants with a different inter-pad gap each varying (60 μm, 50 μm, 45 μm and 40 μm) as described on the cartoon of the lower right of the figure. In each quadrant inter-pad gap is the same for all 5 pad layers. This PCB will allow us to study the impact of the inter pad gap on the spatial resolution performance of the capacitive-sharing readout concept. The smallest gap between neighboring pads is expected to yield the best performances however technical limitation for the fabrication of these boards needs to be taken into account to keep these type of readout at low cost especially for large area applications The second PCB prototype is a X-Y strip readout using the same capacitive-sharing pad layers principle to spread charges over large pitch strips. The principle is illustrated on the cartoons of Fig. 32. For this first prototype, we are exploring a X-Y readout (bottom layer of the capacitive-sharing readout) with 800 μm pitch. Unlike the standard COMPASS X-Y strip readout where X and Y strips are etched on different polyimide (Kapton) layers separated by a 50 μm Kapton bridge gaps, both x-strips and y-strips are etched on the layer. The vertical strips (y-strips) are 400 μm wide straight strips with a pitch of 800 μm pitch meaning that the strips have a 400 μm gap between them filled with rectangular pads of 400 μm $\times$ 800 μm pads along the vertical direction. All the pads on each row are connected together into a single electrode in a pad-like strip configuration. This configuration ensures a perfect equal sharing between the straight vertical and the pad-like horizontal strips as each strips cover exactly the same area, which is another huge advantage over

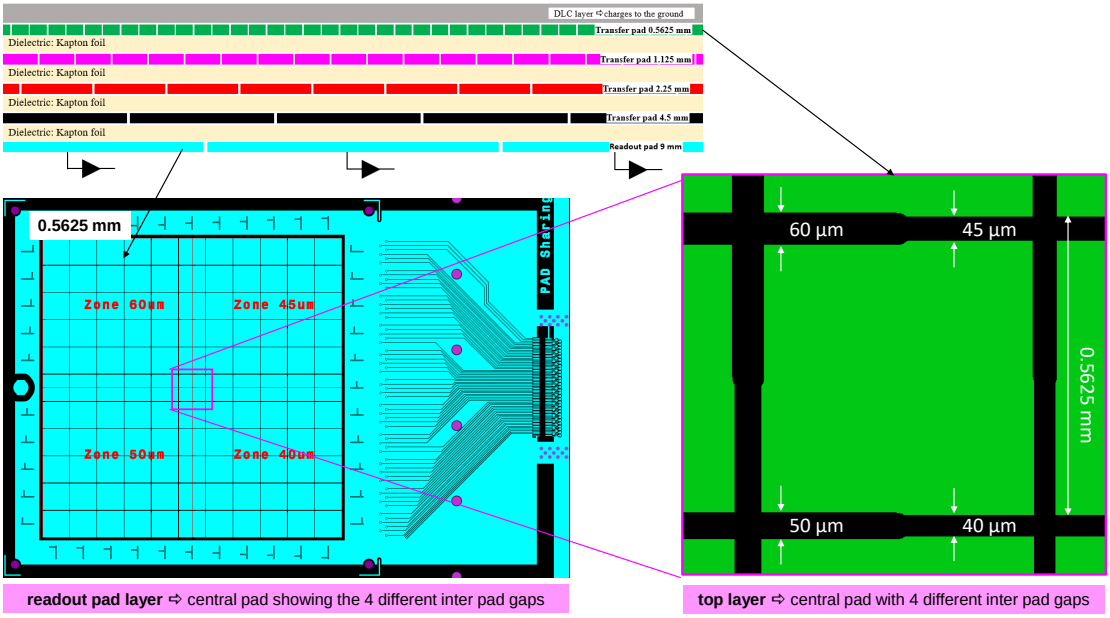

Figure 31: Our second large-pad capacitive-sharing readout prototype with 9 mm × 9mm pad size for triple-GEM amplification. This prototype has 4 pad layers for charge sharing with top layer pad size of 0.5625 mm × 0.5625 mm. The PCB is divided into 4 segments with different inter-pad gaps as indicated on the cartoon of the lower right of the figure

COMPASS readout where maintaining an equal sharing over large detector area is a serious challenge. In our readout prototype, the readout layers is coupled with 2-layers capacitive-sharing pads readout to operate at a spatial resolution performance in the order of 70 μm with a strip pitch of 800 μm double the size of the COMPASS strip pitch, meaning half the number of readout channels. The design of a 10 cm × 10 cm μRWELL prototype with strip capacitive-sharing anode readout has been finalized and is under production at CERN. We expect to have the prototype in hand in about one month. If required by a specific application, one could easily add one pad layer to increase the pitch to 1.6 mm and reduce by another factor two the numbers of channels. This option will be explored in our future plans for large area GEM and μRWELL detector prototypes.

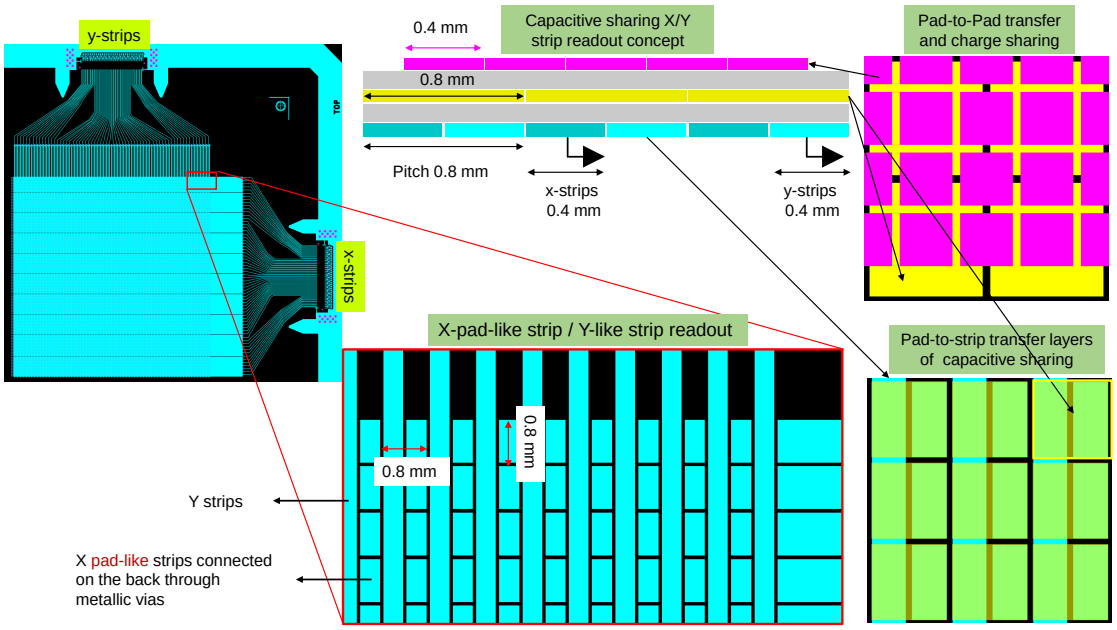

Figure 32: Capacitive-sharing readout prototype with X-Y strip readout. x-direction has pad-like strips where pads are connected together in each row into a strip readout and y-direction has straight strips

4.3 What was not achieved, why not and what will be done to correct?

4.3.1 Cylindrical μRWELL studies at Florida Tech

We have not yet produced mechanical components for a functional prototype.

4.3.2 Cylindrical μRWELL studies at TU

For this cycle, we were not able to successfully complete these planned activities:

1. **Build 10 cm $\times$ 10 cm planar μRWELL μTPC prototype:** This activity experienced an initial set back due to delays in transferring the awarded FY20 money to TU, which was needed to procure the CERN μRWELL kit. This activity was then further delayed to to the Covid-19 outbreak which left TU's detector lab inaccessible. Once we received our FY20 funding and completed the purchase of the μRWELL detector with CERN, we faced yet another delay as it took about a month for the detector to clear US customs. This project is now facing more delays as our FY21 funding has not yet been received.

2. **MPGD Simulation:** In the advent of the EIC Yellow Report meetings, we have adapted the Fun4All simulation and analysis framework, which is currently used by sPHENIX, to migrate our simulation work to. Although we have the cylindrical μRWELL detector implemented in the Fun4All simulation framework, the inclusion of realistic GEM trackers is still missing. These are needed to simulate a complete tracking system. We now have two graduate students(Athira Kunnath Vijayakumar from TU and Merrick Lavinsky from Florida Tech) working on implementing MPGD forward/backward detectors into this framework.

4.3.3 Cylindrical μRWELL studies at UVa

The COVID-19 pandemic situation, has significantly delayed the activities in the MPGD detector labs at UVa and priorities has been assigned to critical activities of our group at UVa. Commissioning and installation of SBS GEM for the Super Bigbite Experiment in Hall A at JLab scheduled to start this fall 2021 is taking up all the resources. In addition, we have also been involved and busy with the EIC Yellow Report activities all year long. Many of the eRD6 R&D activities that we planned for this year have been severely affected by these circumstances

SRS-VMM readout electronics: The small scale VMM-based SRS readout electronics is in our hand at UVa, the setting up of the system at UVa has been put on hold for the moment

Characterization of μRWELL prototype with X-Y strips: Team test at FNAL in March 2021 was planned to complete the spatial resolution studies of the prototype but was later cancelled because of travel restrictions due the pandemic. We are in discussion with FNAL test beam facility team to reschedule the beam test for Mai - June 2021.

Development of High-Resolution Capacitive-Sharing Anode Readout for MPGD detectors: The design of μRWELL prototype with large pad capacitive readout has been completed and the order of the parts have been issue at CERN. We expect the delivery of the parts in a couple of months.

Design and construction of a small size cylindrical μRWELL prototype: The designing of the μRWELL amplification structure and readout layer of small size cylindrical prototype has not yet started.

4.4 What is planned for the next funding cycle and beyond?

The ultimate goal of this joint effort between Florida Tech, Temple U. and UVa is to design and build a fully operational small cylindrical μRWELL prototype and test it in a beam at Fermilab by July 2022.

4.4.1 Cylindrical μRWELL studies at Florida Tech

The Florida Tech group will continue focusing on developing the mechanics for the first functional cylindrical μRWELL prototype. We plan to investigate what the most reliable way is for splicing the edges of the foils together to form continuous leak-tight cylinders. We plan to find the optimal material choice for the end-rings of the actual prototype detector in light of the required precision and with an eye towards minimizing the material in the end-rings.

4.4.2 Cylindrical μRWELL studies at TU

For the remainder of this funding cycle we plan to:

1. **10 cm $\times$ 10 cm μRWELL operating in μTPC prototype:** Complete the assembly and testing of our 10 cm $\times$ 10 cm planar μRWELL prototype operating in μTPC mode.
2. **MPGD Simulation:** Continue the implementation of MPGD (GEM, μRWELL) trackers in the central and forward/backward regions within the Fun4All framework. This includes implementing a parameterization for μTPC operating mode and continuing to iterate on the μRWELL support material as the cylindrical prototype evolves.

3. **Cylindrical μRWELL prototype:** Collaborating with FIT and UVa in designing, constructing and testing a cylindrical μRWELL prototype detector.

4.4.3 Cylindrical μRWELL studies at UVa

Characterization of capacitive-sharing readout planes with GEM amplification: We have recently received three capacitive-sharing readout planes, two with pad readout and the third with X-Y strip readout structures. These board will all be assembled into triple-GEM prototypes and tested both with cosmic and x-ray in the MPGD detector lab at UVa as well as later this summer in beam test at FNAL and / or at this fall JLab. We also plan to start simulation studies with PSPICE simulation tool to model the electrical properties of the capacitive-sharing readout scheme with MPGD detectors. We expect to be able to present some preliminary reports on these modelisation studies at the next EIC detector R&D meeting

μRWELL prototype with X-Y strip capacitive-sharing readout: The design of a 10 cm $\times$ 10 cm μRWELL prototype with strip capacitive-sharing anode readout has been finalized and is under production at CERN. We expect delivery the prototype in a couple of weeks from now and in time for the beam test at FNAL in May - June 2021. After the preliminary test results of the small prototype to validate the proof of concept of μRWELL prototype with X-Y strip capacitive-sharing readout, we will start the design of the μRWELL amplification + readout elements of the cylindrical μRWELL prototype that we are going to build together with our eRD6 colleagues from Florida Tech an Temple U.

5 End Cap Trackers with GEMs

5.1 What was planned for this period?

5.1.1 Florida Tech Large Carbon Fiber GEM Prototype with zigzag readout

We had planned to redesign the inner frames of the detector assembly to strengthen them for better taking up the forces exerted by the stretching screws and nuts and to make the entire inner frame stack from PEEK. If these final refurbishments proved successful in eliminating shorts between foils due to improved stretching, we would perform a full set of quality control tests on the refurbished low-mass prototype and characterize its performance. On the simulation side, new Ph.D. student Merrick Lavinsky planned to use the new Fun4all simulation environment to study track-hit residuals of forward tracks as a function of central tracker and forward tracker material.

5.1.2 UVa Large GEM Prototype with 2D U-V readout

We planned to resume and complete the study of the prototype signal response, to procure different types of zebra strips to test with the prototype in x-ray. Then, we planned to bring the to FNAL a beam test in 2021 and study the spatial resolution performances with 120 GeV proton beam.

5.2 What was achieved?

5.2.1 Florida Tech Large Carbon Fiber GEM Prototype with zigzag readout

We redesigned and produced the inner frames of the detector assembly and made the entire inner frame stack from PEEK as planned (Fig. 33). The rebuild went smoothly and the assembled detector did not have any

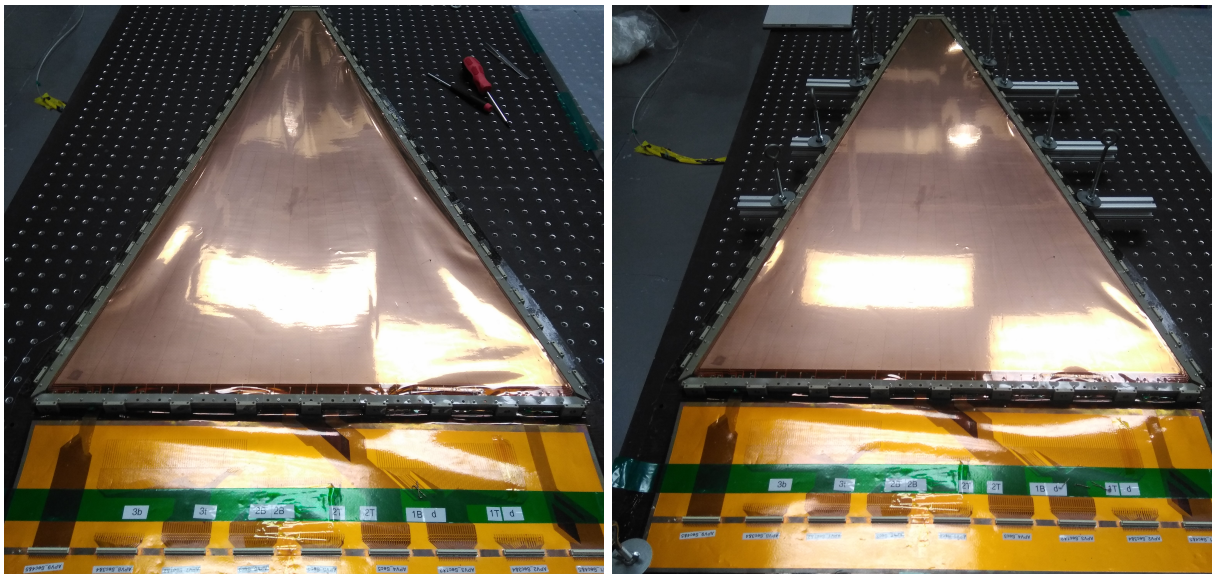

Figure 33: Left: Unsupported large GEM detector released from assembly bench showing loss in foil tension. Right: Detector fixed to a mobile 80/20 support structure with improved foil tension.

shorts between foils as long as the lower carbon fiber frame was fixed to the optical table. However, shorts occurred in every 2 mm transfer gap once the detector was released from the table (Fig. 33 left). Several attempts were made at building a mobile external support structure from 80/20 bars that the detector could be attached to. These had a clear positive effect on the tension of the foils (Fig. 33 right), but ultimately failed to permanently remove the shorts in a reliable way.

The cause of the tension loss appears to be warping in the carbon fiber frames that house the GEM stack. The sketch in Fig. 34 shows why the 80/20 structure had such a dramatic impact. While the frame rests unsupported, the foils are sagging. By pulling downward on the outer edges of the carbon fiber frame and using the heads of the pull-out screws that run along the center of the frame as a fulcrum, we could pull the pull-outs further apart and apply a significant amount of extra tension to the foils.

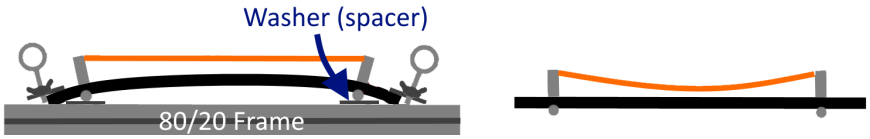

Figure 34: Sketch illustrating how the 80/20 support structure increases foil tension (left) relative to the unsupported configuration (right).

Based on these results, we believe that we have singled out the construction material and geometry of the carbon fiber frames as the current main point of failure. These carbon fiber frames were produced on site and over time they appear to have begun warping and are not capable of maintaining the necessary tension for the foils. Consequently, we have decided to replace them with new frames made from thicker, commercially manufactured quasi-isotropic carbon fiber plates (see also Fig. 39 below), which should deform much less.

We are currently designing the new frame assembly and are modeling the forces on this frame and the resulting deformation. As a first order approximation, a pressure of 1 MPa is applied to the outside edges of the frame to simulate the tension from the GEM foils. The pressure is shown as four clustered arrows in Fig. 35 (left) which represent a force that is distributed evenly across the area of the face to which it is applied. The greatest displacement (2.886 mm) occurs in the centers of the longest sides of the frame as one would expect. To reduce this deformation, a single 3 mm wide central support "rib" is added to the design

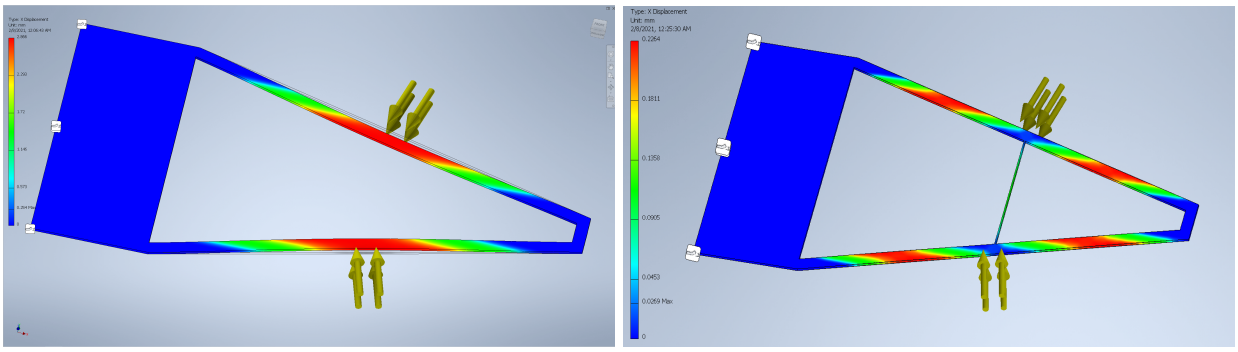

Figure 35: Simulation of strains in a single new carbon fiber frame with pressure uniformly applied to outer surfaces. Left: Open trapezoid. Max. resulting strain is 2.886 mm (red zone). Right: Trapezoid with an additional 3 mm wide central support rib. Max. resulting strain is 0.226 mm (red zones).

in the region of greatest displacement which leads to substantial improvements. The greatest displacement in this new configuration is only 0.226 mm (Fig. 35 right), i.e. more than an order of magnitude less than in the frame without the rib.

The pull-outs are then added to the model of the new frame, along with the top carbon fiber frame (Fig. 36 top). To model the deformation of this complete assembly more accurately, a force of 4.45 N (1 lbf) is applied to each pull-out individually to simulate the tensioning. With the top frame removed, as it will be when assembling the detector and tensioning the foils, the simulation shows that most of the deformation occurs in the vertical direction at the narrow end of the detector (Fig. 36 center). This demonstrates why the lower frame must be firmly attached to the optical table during assembly. However, completing the assembly by adding the top frame stabilizes the assembly due to the restoration of vertical symmetry and reduces the max. deformation to a tolerable 0.08 mm (Fig. 36 bottom) before releasing the assembly from the optical table.

These deformation analyses show that the addition of one central rib to the frames and the use of thicker, professionally manufactured quasi-isotropic carbon fiber material should result in an assembly that will allow proper stretching of the foils in the prototype.

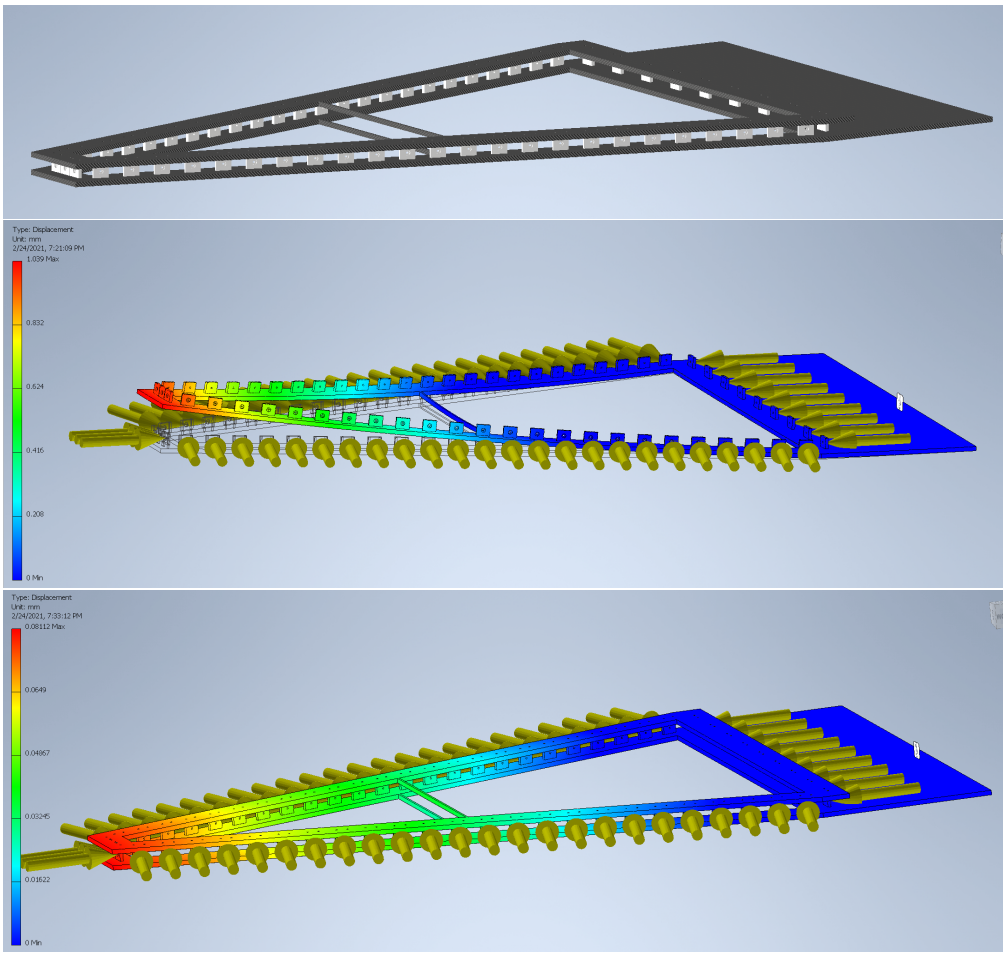

Figure 36: Top: CAD model of complete assembly with ribbed carbon fiber frames (black) and PEEK pull-outs (gray). Center: Simulation of deformation of bottom frame due to inward 4.45 N (1 lbf) forces on each pullout; red indicates the region of maximum deformation (1.039 mm). Bottom: Simulation of deformation for the complete frame assembly under the same forces; red indicates the region of maximum deformation (0.081 mm).

5.2.2 Florida Tech and TU Simulation of Forward Tracking

We are simulating a hybrid design for tracking in an EIC detector using gaseous and silicon trackers. We have implemented the new EIC 'Fun4All' simulation software suite based on GEANT4 that allows us to generate an EIC model detector with realistic materials and geometry in a modular fashion. The current model comprises beam pipe, vertex silicon tracker (VST), central Si barrel, central TPC including an instrumented endcap, Si disks (MAPS), and a forward GEM tracker (Fig. 37). Specifically, we have integrated A. Kiselev's earlier implementation of a forward GEM tracker and VST in the 'EICroot' framework with H. Wennlöf's recent Fun4All implementation of beam pipe, TPC, and Si trackers to create this model.

First preliminary η and momentum resolutions obtained with this hybrid detector model for 10 GeV pion tracks in the overall range $0 \leq \eta \leq 4$ are shown in Fig. 38. However, currently these tracks do not use hits in the Si barrel and disks (due to problems with geometric overlaps that still need to be resolved). This detector configuration produces good η and momentum resolutions of $\sigma_\eta/\eta = 8.4 \times 10^{-4}$ and $\sigma_p/p = 3.1\%$, respectively, when averaged over the full η range.

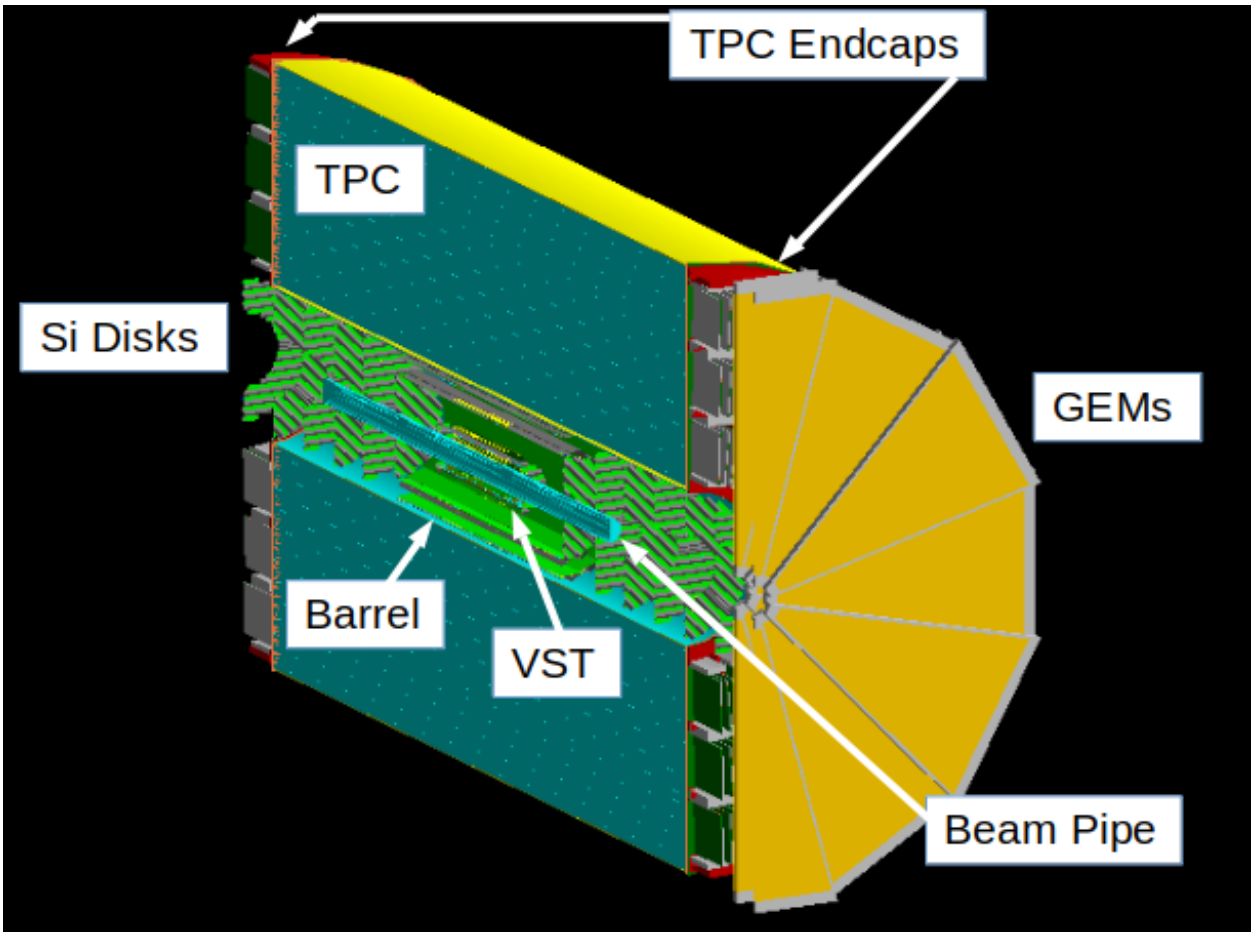

Figure 37: Fun4All model of a hybrid configuration of gaseous and Si detectors for tracking in an EIC detector.

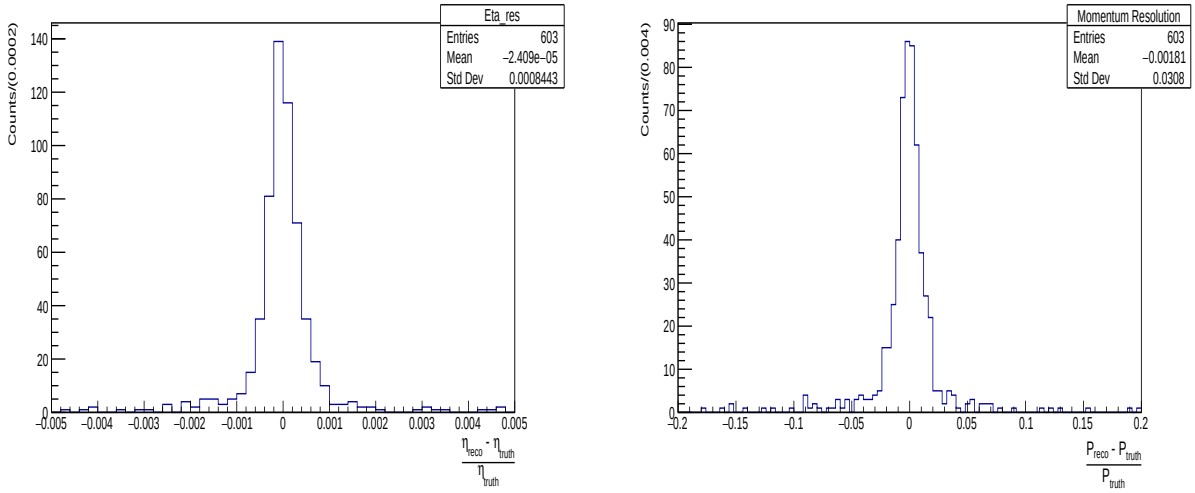

Figure 38: Resolutions in η (left) and momentum (right) for 10 GeV pions averaged over the range $0 \leq \eta \leq 4$ obtained from the Fun4All simulation of the hybrid detector model in Fig. 37, but without use of track hits in the Si barrel and disks (due to problems with geometric overlap).

5.2.3 UVa Large GEM Prototype with 2D U-V readout

Very little was accomplished this cycle around regarding the large U-V strips GEM prototype studies. Please refer to subsection 5.3.2 for more details.

5.3 What was not achieved, why not and what will be done to correct?

5.3.1 Florida Tech Large Carbon Fiber GEM Prototype with zigzag readout

Due to the ongoing detector refurbishment, we have not yet been able to commission the detector. In the Fun4all simulation, the Si barrel and disks could not be fully used, yet. While the material is present in the simulation, these subdetectors have so far failed to generate hits for the track reconstruction due to overlaps in their geometry that still need to be resolved. We also still need to extract information on interpolated track positions with the Fun4All simulation framework to calculate residuals as a function of detector material and position.

5.3.2 UVa Large GEM Prototype with 2D U-V readout

We planned to test different types of zebra connections on the prototype in the x-ray box at UVa in order to identify the best option for the APV25 signal. However, Because of restriction on activities in the detector lab at UVa due to the COVID-19 pandemic situation and priorities set for other looming projects, we were not able to pursue this activity. In addition, we planned to bring the prototype in beam test at Fermilab in March 2021 to finalise the spatial resolution studies of the U-V strip readout. Here again, the beam test has been cancelled because of travel restrictions due the the pandemic. We are in discussion with Fermilab test beam facility team to reschedule the beam test for June 2021.

5.4 What is planned for the next funding cycle and beyond?

5.4.1 Florida Tech Large Carbon Fiber GEM Prototype with zigzag readout

We will optimize the design for the carbon fiber frames with ribs and produce two such frames from the commercial carbon fiber plates that we have already procured (Fig. 39). Using these, we will re-assemble the detector and evaluate if the new frames finally allow proper stretching of the foils. If these refurbishments are successful in eliminating shorts between foils, we will perform a full set of quality control tests on the refurbished low-mass prototype and characterize its performance, e.g. gain curves, with X-rays at Florida Tech and prepare for a potential test beam effort at Fermilab in summer 2021.

On the simulation side, we will use the new Fun4all simulation environment to calculate track-hit residuals of forward tracks as a function of forward tracker materials. The results will guide the final design of the forward GEM tracker.

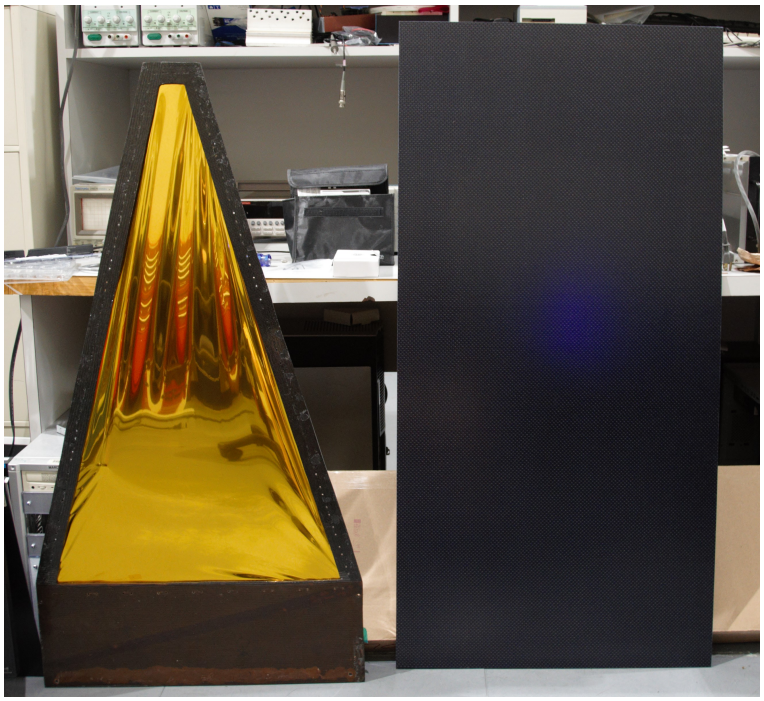

Figure 39: Original 4 mm carbon frame with metalized kapton window produced in-house (left) next to the new commercial quasi-isotropic 1/4-inch carbon fiber plate base material (right) to be used for producing new stronger frames.

5.4.2 UVa Large GEM Prototype with 2D U-V readout

We still plan to studies the spatial resolution performances of the large U-V strips GEM prototype in beam test at Fermilab this summer in order to complete the characterization of the detector. We are in discussion with Fermilab Test Beam Facility team to schedule a beam time this summer 2021 to perform the test. This will conclude the UVa generic R&D program for large area forward GEM tracker for EIC.

6 Developments for high momentum hadron identification at EIC

6.1 What was planned for this period?

6.1.1 MPGD sensors of single photons at INFN Trieste

The activity planned for year 2021 has to include a large fraction of the 2020 planning, that could not be performed due to the current emergency shutdown. The completion of the construction and characterization of the second version of the prototype is now foreseen for the year 2021. This prototype is also designed to make possible comparative studies of the current FE chip, namely APV25, and the newly considered one, namely VMM3. Initial comparative exercises are included in the 2021 planned activities. The present report is related to the initial part of the overall 2021 activity planning.
Related milestone
September 2021: The completion of the laboratory characterization of the second version of the photon detector with miniaturized pad-size.

6.1.2 New Photocathode Materials development at INFN Trieste

The activity planning for the whole year 2021 includes items proposed for the second half of 2020, that could not be performed due to the emergency shutdown, namely:

- The heat treatment, that allows recovering the required electrical rigidity of HND coated THGEMs, has been applied in air atmosphere. Some reduction of the QE is observed, most likely related to oxidation in air. The heat treatment protocol needs to be modified heating in inert atmosphere. Then, it will be verified if the effective QE is preserved.
- The measurements to establish the effective QE of HND photocathodes will be completed.
- The investigation of ND powder parameters influencing the QE performance will be continued.
- First measurements of HND radiation hardness will be performed in the ASSET setup at CERN.

. Moreover, a novel item is added: the realization of a complete small size prototype of a MPGD-based photon detector with hydrogenated nanodiamond power photocathode.

Related milestone
September 2021: Complete small size prototype of a MPGD-based photon detector with hydrogenated nanodiamond power photocathode.

6.1.3 Large mirrors development at Stony Brook

The installation and commissioning of mirror coating equipment was planned in the present funding cycle.

6.1.4 New Radiator Studies at Stony Brook

The continuation of studies towards meta-materials suited for the application of Cherenkov photon detection was planned. The focus for the period was to investigate a neural network framework with internal applications like the T-Matrix method.

6.2 What was achieved?

6.2.1 MPGD sensors of single photons at INFN Trieste

This development is fully based on laboratory activities, seriously affected by the restrictions imposed by the pandemic emergency (Sec. 6.3.1). Moreover, the construction of a new complex prototype has also been delayed by the limited availability of the technical services at INFN Trieste. Therefore, very limited activity could be performed after February 2020.

The detector principle and the basic concepts of its architecture are described in Appendix A, Sec. A.1. The present development stage requires (i) the realization and characterization of a second prototype version and (ii) the validation of the VMM3 front-end chip for single photon detection, where VMM3 has been selected because of its low noise figure and its architecture compatible with a streaming read-out DAQ approach.

In July 2020, we reported that the design of a new prototype of single photon detector based on MPGD technologies was completed. The new design has been optimized in order to overcome the limitations observed in the first prototype version. The MICROMEGAS stage of the new prototype is also designed with different connects that make possible to read-out the detector both with the traditional read-out based on SRS and APV25 front-end and with the MMFE1 board by ATLAS and VMM3 front-end in comparative

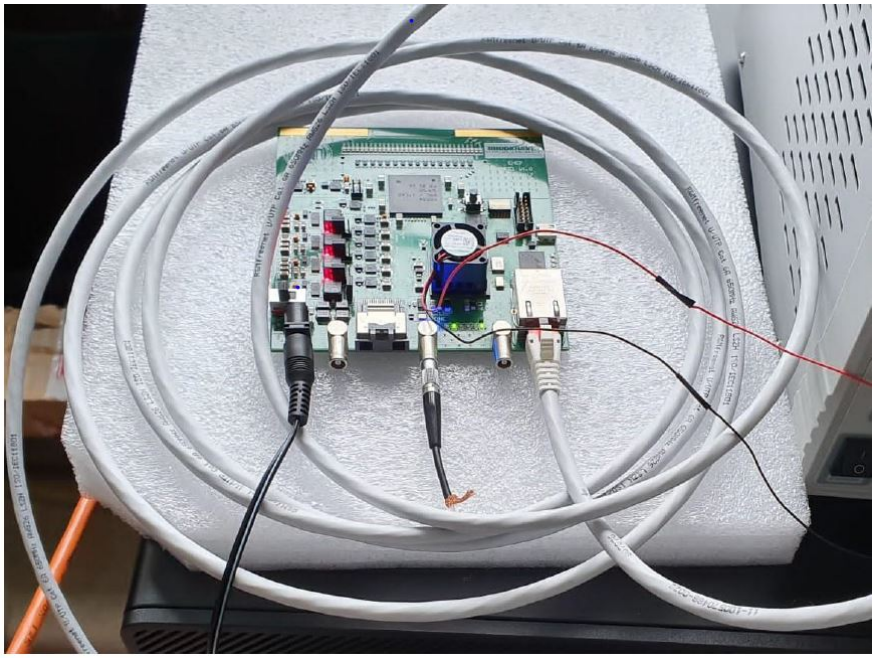

Figure 40: The MMFE1 board used during the preparatory exercises.

exercises. In particular, the delicate design of the anode PCB, which is also the support of the micromesh of the MICROMEGAS stage of the hybrid MPGD, was completed. In the following months, the PCB has been submitted for production, together with the other detector components. Nevertheless, the complete MICROMEGAS could not yet be built and, therefore, the detector is not assembled and equipped.

Concerning VMM3 studies, preparatory exercises could be performed (Fig. 40) to gain experience in using the MMFE1 board and the accompanying control software. The set of exercises includes threshold calibration, on-board pulse signal calibration (both polarities) and acquisition of the digital output signals.

6.2.2 New Photocathode Materials development at INFN Trieste

This activity consists in studies to understand the compatibility of an innovative photocathode material by Hydrogenated-NanoDiamond powder (H-ND) with the operation of gaseous detectors as well as in progressing in the characterization of the photoconverter itself. The R&D details are provided in Appendix A, Sec. A.2.

This development is fully based on laboratory activities, affected by the restrictions imposed by the pandemic emergency. Also traveling restrictions had a negative impact on the activity, in particular preventing common Bari and Trieste campaigns of measurements and the access to the facility ASSET at CERN. Nevertheless, substantial preparatory actions could take place, as illustrated in the following. They form a solid base in view of fulfilling the planned activity if the restrictions are released in the second part of the current year.

The activity is progressing along two development lines that, if both successful, will merge at the end in gaseous photon detectors equipped with new photocathode materials. The study of the QE properties of the H-ND powder (line i), namely the selection of the best powder among those commercially available and the identification of the powder parameters that affect the QE is performed coating small disc-shaped substrates. The compatibility of the H-ND powder with THGEMs as photocathode substrate is pursued in order to prove that this novel photoconverter can be successfully coupled with MPGDs (line ii).

A portable gas mixing system in view of well-controlled and reproducible measurements of the effective Quantum Efficiency (QE) in different gas atmospheres has been design. The relative amount of gas compo-

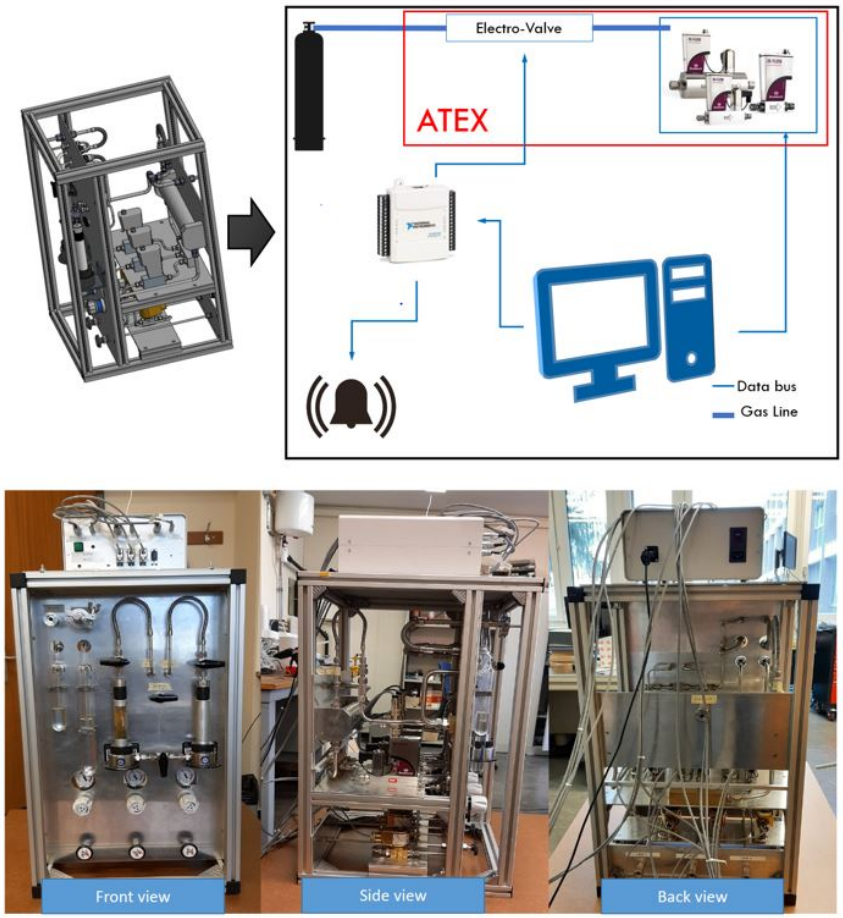

Figure 41: The portable gas mixing system for nanodiamond photocathode studies; top: the schematics of the control system; bottom: pictures of the gas mixing system.

nents in the mixtures in controlled by ATEX-compliant mass flowmeters: it is so possible to make use also of flammable gasses, as methane. The system includes the electronic control system. The system is now realized and tested, ready for usage (Fig. 41). This new tool will be used to progress in both development lines.

Twenty new THGEMs (Fig. 42) have been produced by industry and then submitted to the refinement protocol in Trieste. The protocol, optimized in the past for the COMPASS RICH upgrade, includes: polishing with pumish powder, high pressurized water cleaning, cleaning in ultrasonic bath with Sonica PCB solution, cleaning with distilled water and then drying for 24 hours at 180^0C. All the THGEMs have been completely characterized with a set of measurements that include drift scan, induction scan, scan of the biasing voltage and gain monitoring over 4-7 days, in order to obtain, for each piece, a complete characterization table as reference for performance comparison after coating with the photoconverter film. It is important to stress that all the characterization measurements have been accompanied by continuous monitoring of the temperature T and pressure P parameters. In fact, as also demonstrating in Fig. 43, without applying to the measured gain values the correction related to the P/T ratio, no reliable reference performance is obtained. The yield of good THGEMs is at the 90% level. These fully characterized THGEM are now ready for coating with the photoconverter film. The new set of THGEMs is essential for progressing in the development line (ii).

The construction of a small prototype of photon detector, including all the required MPGD multiplication

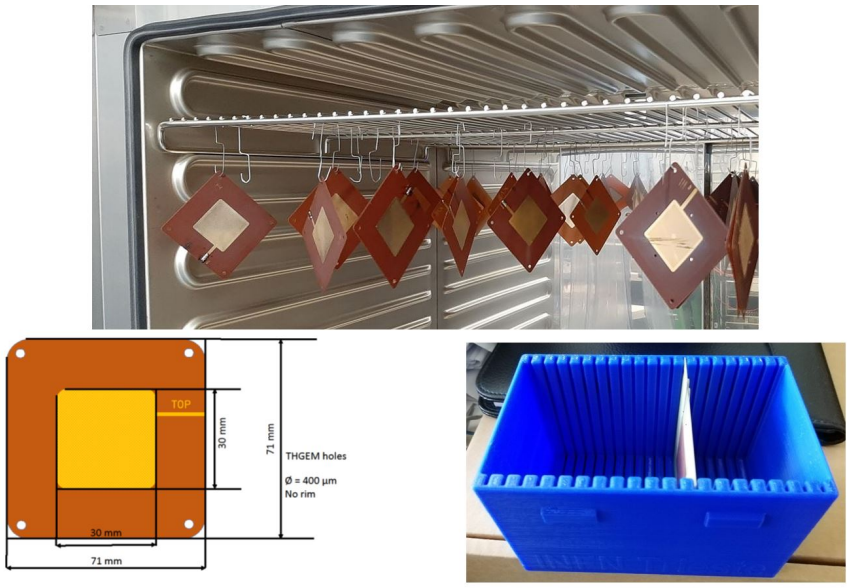

Figure 42: THGEMs produced for the nanodiamond photocathode studies; top: picture of the new set of THGEMs; bottom, right: geometrical dimensions of the THGEMs; bottom, left: picture of the box realized by 3D printing for THGEM storing and transportation.

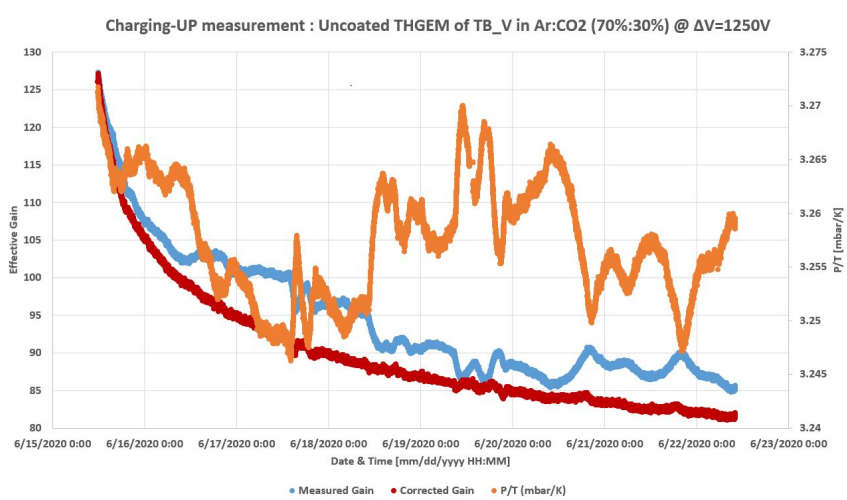

Figure 43: Effective gain of a typical THGEM measured over one week. The raw gain (in blue) is corrected according to the P/T values in order to obtain the effective gain independent from P and T variations (in red); P/T ratio is also plotted (in orange) with reference to the right vertical axis. The smooth trend of the corrected gain-values confirms the validity of the correction approach.

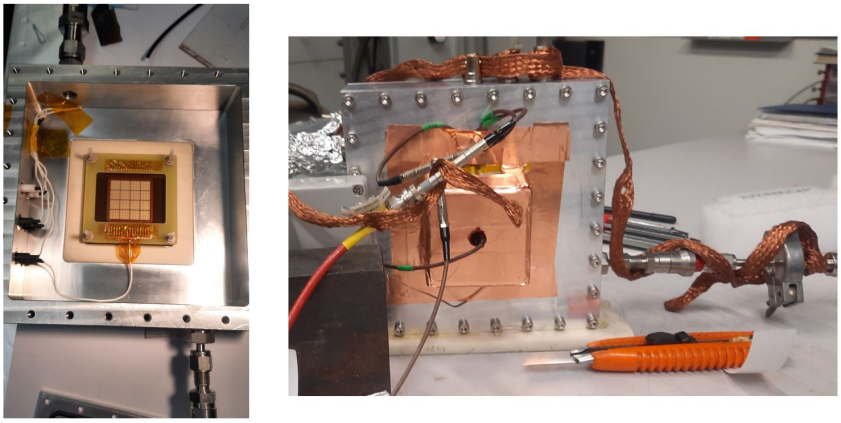

Figure 44: Prototype of a complete MPGD-based photon detector for H-ND powder photoconverter validation; left: picture of the MICROMEGAS, which is the most demanding component of the detector; right: the detector ready for the initial tests.

stages, which will be equipped with a THGEM coated with H-ND film, is also beneficial to the development line (ii). The prototype is now complete (Fig. 44) and it is presently been tested. Figure 45 present the very good gain scan of the MICROMEGAS stage of the prototype measured using a ^{55}Fe source. The following step consists in replacing the first THGEM layer with an H-ND coated one.

A complementary exercise is ongoing aiming at a precise comparison of the effective QE of the novel H-ND photocathodes and photocathodes by CsI. For this purpose, a set of disk-shaped substrates have been mounted on an appropriate support adequate for coating the substrate samples with CsI in the CsI coating setup at CERN (Fig. 46). In the CERN setup, the QE of the photocathodes is measured inside the coating setup itself immediately after coating. This measurement provides relative information about the QE, even if no absolute values can be obtained. In fact, no calibration of the response is available. Coated samples whose QE has been measured in the coating setup have been obtained. The comparative measurement of the absolute QE-value with the Bari facility could not yet be performed due to the present traveling restrictions. This exercise is part of the development line (i).

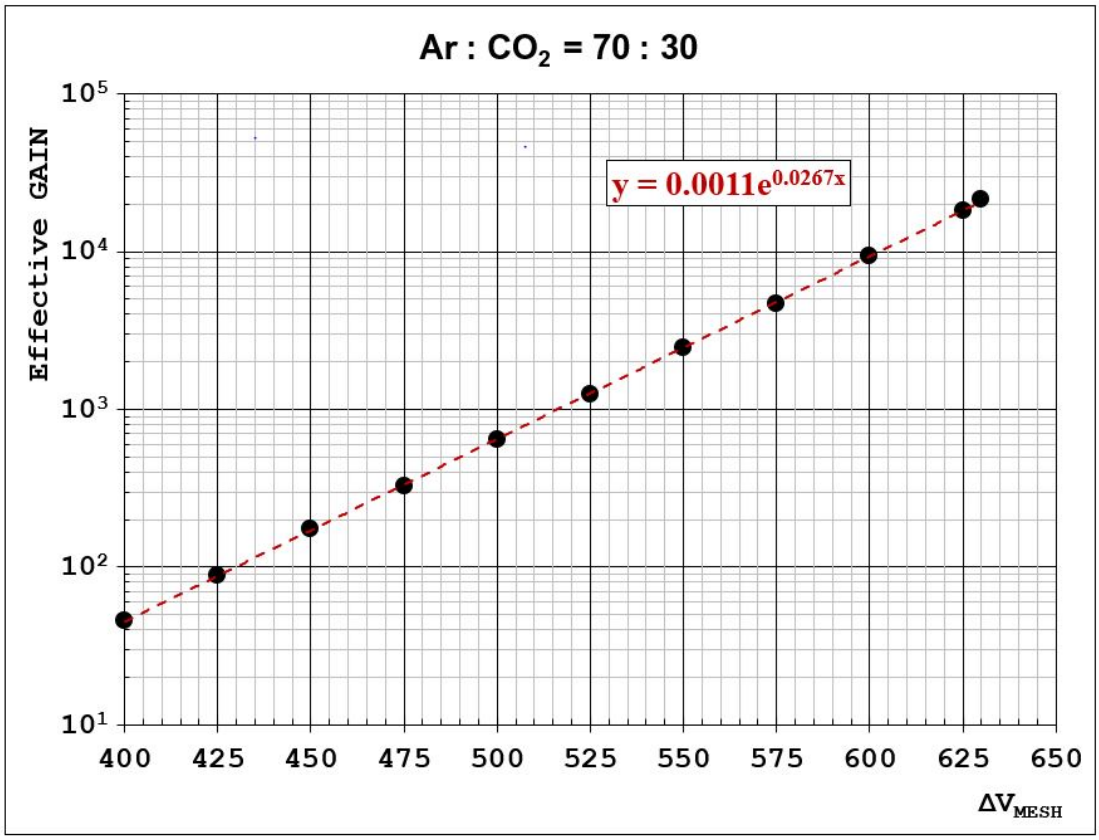

Figure 45: Gain of the MICROMEGAS stage of the prototype of a complete MPGD-based photon detector for H-ND powder photoconverter validation measured using Ar:CO_2=70:30 gas mixture and illuminating the detector with a ^{55}Fe source.

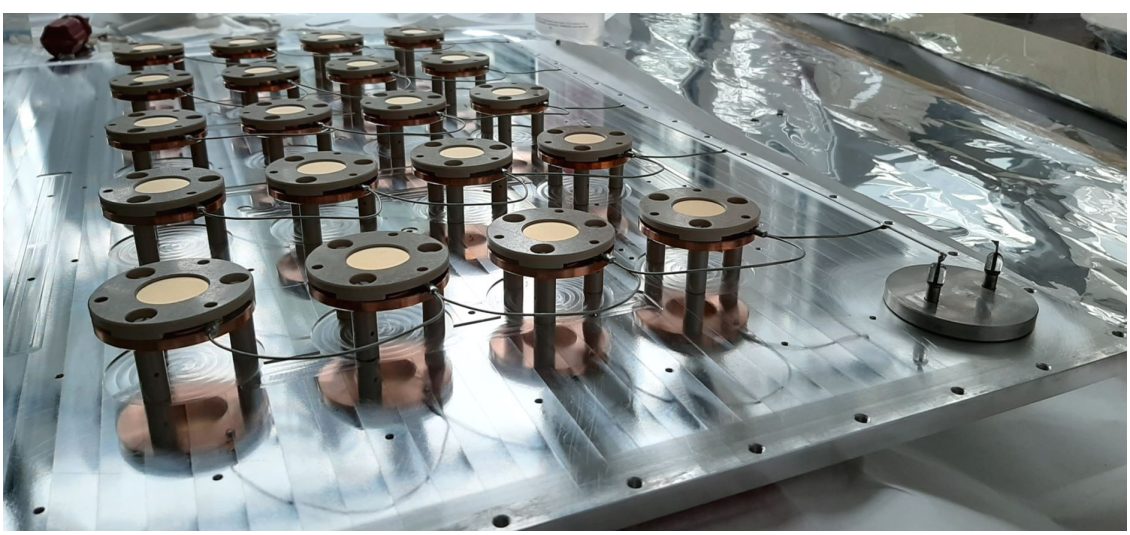

Figure 46: A set of disk-shaped substrates mounted on an appropriate support for CsI coating at CERN. The assembly includes the electrical connections that make possible the relative QE measurement inside the setup to be performed immediately after coating.

6.2.3 Large mirrors development at Stony Brook

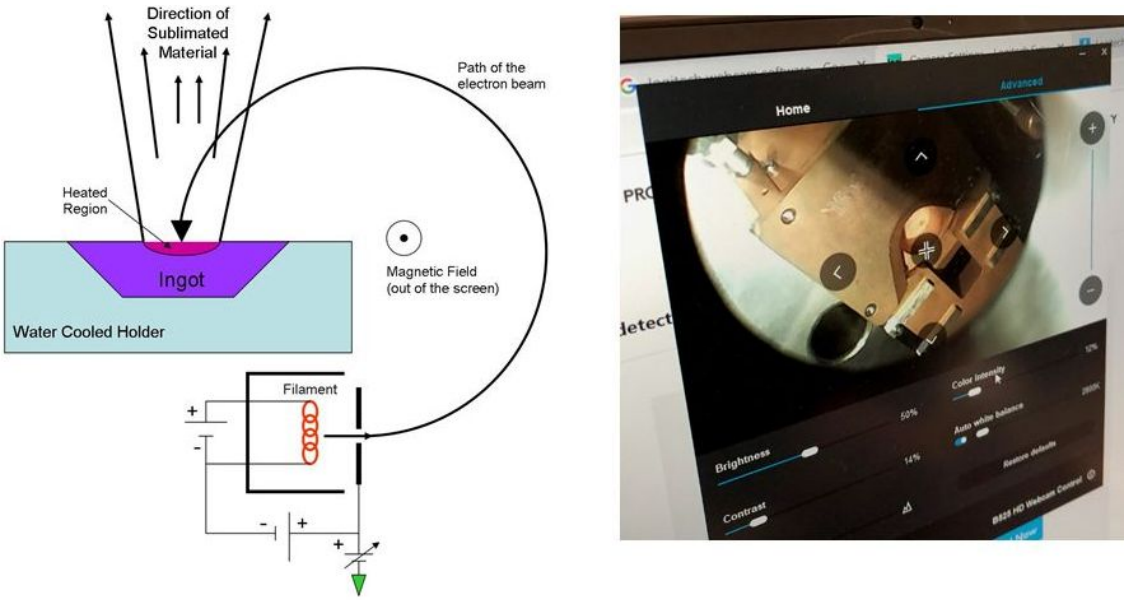

Figure 47: Left: principle of PVD with an electron beam device. Right: Real time camera picture focused on the ingot region.

The evaporator has been evacuated and is performing stable and well with respect to vacuum conditions. The vacuum generating device is three-staged, consisting of: scroll pump, turbo-molecular pump and cryogenic-pump. The successive implementation of these stages allows to generate high vacuum (HV) conditions, with remaining pressures down to a few 10^{-7} Torr. We anticipate to even reach ultra-high vacuum (UHV) conditions when tweaking the last stage, with pressures down to a few 10^{-8} Torr. Anyways, reaching HV conditions will enable us to comfortably proceed with PVD typical applications.
The commissioning of the physical vapor deposition (PVD) equipment has been finalized. We are using thickness monitor devices and a camera system to monitor the electron source (Fig. 47).
Our commissioning efforts were investigating the deposition behavior of Chromium and Aluminum as a function of applied power and time. We are preparing presently for an application specific setup. The first application will be the evaporation of Al-stripes on electroless nickel immersion gold (ENIG) surfaces. This will find an implementation in the calibration efforts in a TPC with space charge issues, amongst others. A well defined pattern will be produced by this procedure which allows to illuminate the central membrane of a TPC with a laser beam that forces the controlled emission of electrons. These electrons should be projected onto the readout modules in a 1:1 fashion and any distortions of the pattern can be used for calibration purposes. The production of the pattern will be achieved by hanging the individual petals on an assembly which will be rotated with in the evaporator (Fig. 49). The pattern requires multiple deposition materials: at first a thin layer of Cr which acts as an adhesion layer for the subsequent deposition of Al as the main ingredient. The electron beam device allows to work with up to seven different deposition materials due to a multi-channel crucible device within short time periods and without breaking the vacuum.
After a delay, mainly due to the scarcity of manpower and the Covid-19 lockdown, we consider the project of the construction of a device for large mirror coating purposes as accomplished. The device will be available to the for the production of equipment, for instance, large mirror coating for the SoLID experiment.

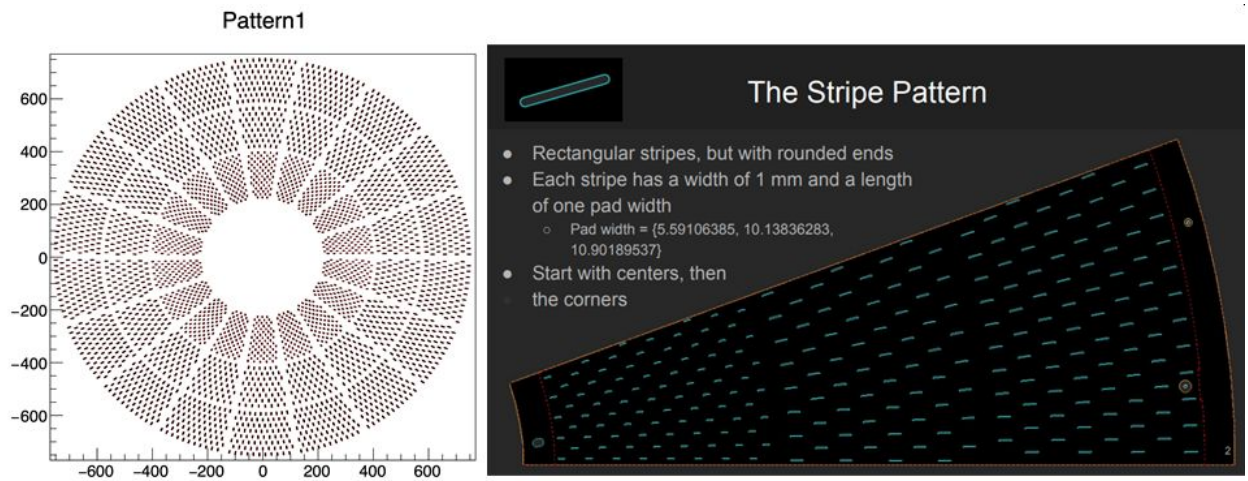

Figure 48: Left: projected cartoon of wedges which are equipped with GEM readout structures for the sPHENIX TPC. A defined pattern of Al-stripes will be attached to the HV-membrane. Right: details of the stripe pattern for one petal corresponding to one wedge seen at the left.

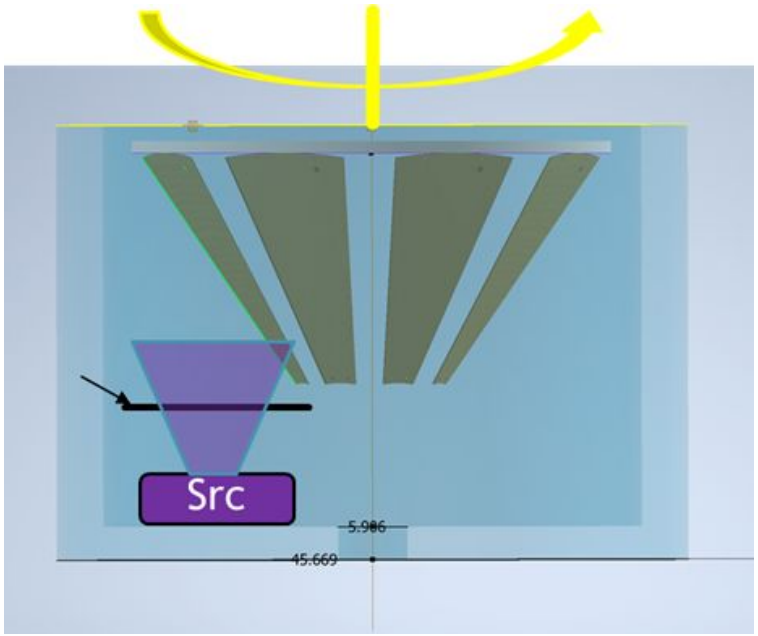

Figure 49: Sketch of the assembly structure in the evaporator that allows to deposit Al in a controlled way onto a surface. The arrangement has to be optimized such that a uniform deposition takes places all over the surfaces under consideration.

6.2.4 New Radiator Studies at Stony Brook

We are in the process to implement T-Matrix code to the application of a neural network framework. Fortunately, there are a variety of pre-existing codes of which we can choose to implement, e.g. [8, 9]. The task is now to verify that the computer-codes are applicable to our problem. As a refresher, the procedure we are going after is to seek appropriate materials that promise to provide the needed scattering and absorption properties toward photons generated by the Cherenkov effect. The next step is to investigate in which assembly form the structures of these materials provide the desired permittivity of the meta-material. This will be done by testing their properties with the T-Matrix methods to confirm or eliminate the configuration. Since the trial and error approach is prohibitively time consuming we are aiming to involve a neural network framework that makes use of the T-Matrix method for providing the training and validation data-sets.

6.3 What was not achieved, why not and what will be done to correct?

6.3.1 MPGD sensors of single photons at INFN Trieste

This development is fully based on laboratory activities, seriously affected by the restrictions imposed by the pandemic emergency. Laboratory activities have been stopped at INFN Trieste and at INFN Bari at the beginning of March 2020, partially restarted in September2020 and almost completely stopped again at the end of October 2020. Therefore, about 70% of the last 12 month period is of forced inactivity and the planned work has to be compressed in the remaining part of 2021.

In particular: the construction and characterization of the second version of the prototype is seriously delayed.

6.3.2 New Photocathode Materials development at INFN Trieste

In spite of the restrictions imposed by the pandemic emergency, no major delay is registered for this activity. In fact, substantial preparatory actions could take place. They form a solid base in view of fulfilling the planned activity if the restrictions are released in the second part of the current year. In particular, traveling restrictions are those more severely affecting the developments to establish novel photocathode materials for gaseous detectors.

6.3.3 Large mirrors development at Stony Brook

We consider the task accomplished and therefore do not assume any further reportable activity.

6.3.4 New Radiator Studies at Stony Brook

The task is set up as a long term task and therefore can not be considered as having no achievements.

6.4 What is planned for the next funding cycle and beyond?

6.4.1 MPGD sensors of single photons at INFN Trieste

In the second part of year 2021, the goal is to complete the activity foreseen for the current year, which is described in detail in Sec. 6.1.1.

Moreover, the new activity, recently started, dedicated to RICH simulation within the EIC Fun4All frame, will be continued with the goal to simulate a gaseous RICH with mirror/photon detector arrangement assuring the minimum spherical aberration.

6.4.2 New Photocathode Materials development at INFN Trieste

The activity foreseen for the second part of the current year is the completion of the planned actions illustrated in Sec. 6.1.2. The completion is possible on the basis of the relevant preparatory activity performed in the first part of the current year (described in Sec.6.2.2), if traveling restrictions are made less severe.

6.4.3 Large mirrors development at SBU

The goal was accomplished and future activities will be the production of equipment as needed.

6.4.4 New Radiator Studies at Stony Brook

The T-matrix formalism will be investigated and comparison between scattering/extinction spectra will be compared with already developed FEM models.

7 Critical Issues: Impact of COVID-19 pandemic

7.1 Brookhaven National Lab

7.1.1 How did the COVID-19 pandemic affect progress of your project?

BNL halted normal operations around March 20th and went into "min-safe" mode, effectively barring any scientific staff from entering the site until the summer. The lab started a gradual/phased reopening in mid-June, but members of our group were not be permitted to return to work until mid-July. Normal work schedules for our immediate group only resumed in the Fall. At this point we are almost back on track, however some of the R&D items that were not completed are related to these delays.

7.1.2 How much of your FY20 funding could not be spent due to the closing of facilities?

We received $37,500 in new funding in FY20 compared to our funding request of $75,000 (i.e., 50%). By the end of the FY, we have spent $16.5K of these funds on materials, PCB fabrication and technical support. We had intended to use the remaining $21K (which includes overhead, resulting in $14K in spendable funds) to partially support our test beam effort that was mostly covered by our MPGD LDRD in order to test some preliminary designs of readout boards for our TPC prototype. These funds will be carried over into FY21 to hopefully do these tests in 2021.

7.1.3 Do you have running costs that are needed even if R&D efforts have paused?

No. Other than pre-existing or newly placed orders we do not have any ongoing costs during the shutdown.

7.2 Florida Tech

7.2.1 How did the COVID-19 pandemic affect progress of your project?

As the occupancy of our high-bay laboratory is low, the hardware activity could mostly continue in a regular fashion. Since June 15 the university has allowed regular operations as long as social distancing measures and CDC guidelines are observed.

7.2.2 How much of your FY20 funding could not be spent due to the closing of facilities?

Most of the funding is for students and stipend payments were continued. Also procurement for the mechanical mock-up and the large forward GEM detector continued.

7.2.3 Do you have running costs that are needed even if R&D efforts have paused?

Student stipends.

7.3 INFN Trieste

The critical issues concerning the 2021 activities are related to the level of recovery of the standard working conditions at INFN during the current year. Any incompleteness in the restoration of standard working conditions can result in further delays.

7.3.1 How did the COVID-19 pandemic affect progress of your project?

The INFN-Trieste tasks are fully based on laboratory activity seriously affected by the restrictions imposed by the pandemic emergency. Laboratory activities have been stopped at INFN Trieste and at INFN Bari at the beginning of March 2020, partially restarted in September 2020 and almost completely stopped again at the end of October 2020. Moreover, traveling restrictions have also affected the activity, both preventing those laboratory studies in Bari that would require the contribution in presence of the Trieste team and stopping those laboratory measurements that had to be performed at CERN. These restriction have also caused a substantial manpower reduction. In fact, one of our postdocs was blocked for seven months in India, after having reached his Country for a short vacation in February 2020. Then, he had no way to come back in the following months due to banishment from both countries (Italy and India) and lack of flights. Summarizing, the large majority of the last reporting period is characterized by forced reduced activity and a large fraction of the planned work has to be moved to the remaining 2021 months.

In this context, it is relevant to underline that our activity could not follow a prioritization planing. In fact, the restrictions affect the activities in a patchy way. Therefore, activities continued as much as possible taking advantage of opportunistic options.

7.4 Stony Brook University

7.4.1 How did the COVID-19 pandemic affect progress of your project?

The COVID-19 situation created the shutdown of all lab activities starting from mid-March in 2020. The consequence was the stop of the start-up process for the evaporator as well as the planned commissioning activities.
The planning process for testing the gating grid structure was impacted, too.

The partial reopening of the lab in June 2020 was limited to senior personnel to enter the labs and only at a later stage students were allowed to support the work in the lab. This created at least a working situation and the commissioning of the evaporator setup could be finished.
The gating grid structure could be finalized and we have the devices ordered and in hand.

7.4.2 How much of your FY20 funding could not be spent due to the closing of facilities?

None of the spending of FY20 funding was paused. We were continuing the design of the gating grid and we are waiting to have access to the magnet test facility at ANL.

7.4.3 Do you have running costs that are needed even if R&D efforts have paused?

None.

7.5 Temple University

7.5.1 How did the COVID-19 pandemic affect progress of your project?

Due to the COVID-19 pandemic, Temple's labs were closed from mid March-August 2020. This closure led to the delay of the building of our μRWELL μTPC. Although Temple labs are now open and accessible, we are not able to carry out some of the beam tests that we had originally planned in coordination with others in eRD6 due to COVID related restrictions at national facilities.

7.5.2 Non-COVID related issues

Additionally, we have yet to receive our awarded FY21 funds, which includes partial postdoc support for our R&D activities.

7.6 University of Virginia

7.6.1 How did the COVID-19 pandemic affect progress of your project?

The COVID-19 pandemic situation, has significantly delayed our activities in the MPGD detector labs at UVa and priorities has been assigned to the critical activities of our group at UVa with the ongoing commissioning and installation of large area GEM layers s for the Super Bigbite Spectrometer Experiments (SBS) scheduled to start this fall 2021 in Hall A at JLab. The continuation and completion of the activities related to the EIC detector R&D effort is undoubtedly affected by these exceptional circumstances. Moreover, critical aspects of the R&D efforts for this cycle would depend on our ability to schedule a few weeks of beam test time slots at FNAL this summer 2021 to study the performances of readout concept that we are developing for μRWELL detector technologies. Failure to secure the beam test time slot at FNAL will lead to a considerable delay of most of the R&D program.

7.7 Vanderbilt University

7.7.1 How did the COVID-19 pandemic affect progress of your project?

Due to pandemic VU MPGD lab was closed from beginning of March until August which delayed in procuring lab equipment for setting up MPGD R&D test bench. This also delayed in joining efforts with eRD6 group. Pre-pandemic we planned to finish performing characterization of MPGD based detectors (triple GEM, quad GEM, GEM + micromegas) for various gas mixtures which would have been helpful in having better understanding of proper gas mixture for PID in TPC.

7.8 Yale University

7.8.1 How did the COVID-19 pandemic affect progress of your project?

Due to the pandemic, non-essential staff have been asked to work remotely. Short-term visitors are not allowed on campus, meaning that we were unable to perform the search for a Senior Research Scientist to replace Dr. Majka. This significantly reduced the effort the Yale group could contribute over the past year.

8 Manpower

8.1 Brookhaven National Lab

Our total manpower effort on MPGDs for EIC, which includes eRD6 as well as other activities, is listed below. All scientific and engineering manpower is being supported by internal BNL funds. Funds are requested from eRD6 for technical support.

Total manpower effort for MPGD R&D

- 2 Senior Scientists: Martin Purschke (0.2 FTE), Craig Woody (0.2 FTE)
- 1 Scientist: Alexander Kiselev (0.4 FTE)
- 1 Physics Associate: Bob Azmoun (0.6 FTE)
- 1 Electronics Engineer: John Kuczewski (0.1 FTE)
- 1 Technician: Bill Lenz (0.5 FTE).

Manpower effort for eRD6 R&D

- 2 Senior Scientists: Martin Purschke (0.1 FTE), Craig Woody (0.1 FTE)
- 1 Scientist: Alexander Kiselev (0.2 FTE)
- 1 Physics Associate: Bob Azmoun (0.2 FTE)
- 1 Electronics Engineer: John Kuczewski (0.1 FTE)
- 1 Technician: Bill Lenz (0.3 FTE).

8.2 Florida Tech

- Marcus Hohlmann, Professor, 0.25 FTE, not funded under this R&D program.
- Jerry Collins II, physics graduate student (M.S.), 1.0 FTE, focusing on μRWELL mock-up hardware, partially funded in fall 2020 and spring 2021 by this R&D program.
- Jared Hadley, physics undergraduate student, 0.1 FTE, focusing on large forward GEM hardware, unfunded.
- Merrick Lavinsky, physics graduate student (Ph.D.), 0.25 FTE, focusing on simulations, partially funded in fall 2020 and spring 2021 by this R&D program.

8.3 INFN Trieste

From INFN Trieste:

- C. Chatterjee (postdoc), 0.2 FTE
- D. D'Ago (Trieste University and INFN, PhD student), 0.5 FTE
- S. Dalla Torre (INFN, Staff) 0.2 FTE
- S. Dasgupta (INFN, postdoc) 0.4 FTE
- S. Levorato (INFN, Staff) 0.2 FTE
- F. Tessarotto (INFN, Staff) 0.2 FTE
- Triloki (INFN, postdoc) 0.5 FTE

The contribution of technical personnel from INFN-Trieste is also foreseen according to needs.

From INFN BARI:

- Grazia Cicala (NCR staff and INFN) 0.3 FTE
- Giuseppe Casamassima (INFN, Staff) 0.3 FTE
- Teresa Ligonzo Teresa (Bari University and INFN, senior scientist) 0.4 FTE
- Antonio Valentini (Bari University and INFN, professor) 0.3 FTE

Globally, the dedicated manpower is equivalent to 3 FTE.
The effective FTE during the present reporting period is reduced to approximately one third due to the restrictions related to the pandemic emergency.

8.4 CEA-Saclay

All senior scientific and engineering manpower is being supported by internal CEA fund. Funds are requested from eRD6 for technical support. Post-docs and PhD students are not funded under the eRD6 program.

- Physicists: Francesco Bossù (0.3 FTE)
- Engineer: Stephan Aune (0.1 FTE), Maxence Vandenbroucke (0.1 FTE)
- PhD students: Aude Glaenzer (0.2 FTE), Maxence Revolle (0.5 FTE)

8.5 Stony Brook University

- K. Dehmelt, Research Associate Professor, 0.2 FTE
- T. K. Hemmick, Professor, 0.1 FTE
- P. Garg, Research Assistant Professor, 0.1 FTE
- S. Park, Postdoc, 0.1 FTE
- V. Zakharov, Grad student, 0.5 FTE
- A. Zhang, Research Assistant Professor, 0.1 FTE

None of the personnel is funded under this R&D program.

8.6 Temple University

- B. Surrow, Professor, 0.1 FTE
- M. Posik, Assistant Research Professor, 0.1 FTE
- A. Quintero, Post-doc, 0.1 FTE
- Athira Kunnath Vijayakumar, graduate student, 0.1 FTE

8.7 University of Virginia

None of the labor at UVa is funded by EIC R&D. The workforce is listed below:

- N. Liyanage; Professor; 0.1 FTE
- K. Gnanvo; Senior Research Scientist; 0.25 FTE

8.8 Vanderbilt University

None of the research personnal listed below is funded by this R&D programe

- Julia Velkovska , Professor, 0.05 FTE
- Vicki Greene, Professor , 0.05 FTE
- Sourav Tarafdar, Research Assistant Professor, 0.3 FTE

8.9 Yale University

None of the research personnel listed below is funded by this R&D program.

- Helen Caines , Professor, 0.05 FTE
- Nikolai Smirnov, Research Scientist , 0.2 FTE

9 External Funding

9.1 Brookhaven National Lab

All scientific and engineering manpower is being supported by internal BNL funds. However, technical support for our eRD6 activities requires support from eRD6 funds.

Additional work on R&D on Micropattern Detectors for EIC is also being provided by a BNL LDRD in collaboration with Saclay and Stony Brook. This is supporting our continued work on zig-zag readouts with GEMs and Micromegas and we do not request any funding for this effort from EIC R&D funds. However, our proposed work on TPC R&D for EIC would not be covered under LDRD funds. It must be noted that our LDRD project ended in Feb. 2021 and we will no longer have any funding for the development of interleaved anode patterns specialized for a TPC.

9.2 Florida Tech

None.

9.3 INFN Trieste

A support of 20 keuro for the year 2021 has been granted by INFN. INFN has also provided the matching resources to extend the postdoc position to one full year.

9.4 Stony Brook University

There is no external funding for this R&D effort.

9.5 Temple University

As of this writing no external funding has been used for eRD6 related projects.

9.6 University of Virginia

None.

9.7 Vanderbilt University

All the tasks performed so far for this R&D has been supported by Vanderbilt research grant.

10 List of all EIC publications from the eRD6 Consortium

BNL publications:

[1] C. Perez-Lara et al. "A Comparative Study of Straight-Strip and Zigzag-Interleaved Anode Patterns for MPGD Readouts". In: *IEEE Transactions on Nuclear Science* [Submitted for publication Jan. 2021] (2021).

[2] B. Azmoun et al. "Design Studies of High Resolution Readout Planes using Zigzags with GEM Detectors". In: *IEEE Transactions on Nuclear Science* PP (June 2020), pp. 1–1. DOI: 10.1109/TNS.2020.3001847.

[3] B. Azmoun et al. "Results From a Prototype Combination TPC Cherenkov Detector With GEM Readout". In: *IEEE Transactions on Nuclear Science* 66.8 (Aug. 2019), pp. 1984–1992. ISSN: 1558-1578. DOI: 10.1109/TNS.2019.2928269.

[4] M. Vandenbroucke et al. "A Study of "Zigzag" Strip Readout for Micromegas Detectors". In: Nov. 2018, pp. 1–4. DOI: 10.1109/NSSMIC.2018.8824702.

[5] B. Azmoun et al. "Design Studies for a TPC Readout Plane Using Zigzag Patterns with Multistage GEM Detectors". In: *IEEE Transactions on Nuclear Science* (July 2018), pp. 1–1. ISSN: 0018-9499. DOI: 10.1109/TNS.2018.2846403.

[6] B. Azmoun et al. "A Study of a Mini-Drift GEM Tracking Detector". In: *IEEE Transactions on Nuclear Science* 63.3 (June 2016), pp. 1768–1776. ISSN: 0018-9499. DOI: 10.1109/TNS.2016.2550503.

[7] Craig Woody et al. "A Prototype Combination TPC Cherenkov Detector with GEM Readout for Tracking and Particle Identification and its Potential Use at an Electron Ion Collider". In: 2015. arXiv: 1512.05309 [physics.ins-det]. URL: https://inspirehep.net/record/1409973/files/arXiv:1512.05309.pdf.

[8] B. Azmoun et al. "Initial studies of a short drift GEM tracking detector". In: *2014 IEEE Nuclear Science Symposium and Medical Imaging Conference (NSS/MIC)*. Nov. 2014, pp. 1–2. DOI: 10.1109/NSSMIC.2014.7431059.

[9] M. L. Purschke et al. "Test beam study of a short drift GEM tracking detector". In: *2013 IEEE Nuclear Science Symposium and Medical Imaging Conference (2013 NSS/MIC)*. Oct. 2013, pp. 1–4. DOI: 10.1109/NSSMIC.2013.6829463.

Florida Tech publications:

[1] Marcus Hohlmann et al. "Low-mass GEM detector with radial zigzag readout strips for forward tracking at the EIC". In: *2017 IEEE Nuclear Science Symposium and Medical Imaging Conference (NSS/MIC 2017) Atlanta, Georgia, USA, October 21-28, 2017*. 2017. arXiv: 1711.05333 [physics.ins-det]. URL: http://inspirehep.net/record/1636290/files/arXiv:1711.05333.pdf.

[2] Aiwu Zhang et al. "A GEM readout with radial zigzag strips and linear charge-sharing response". In: *Nucl. Instrum. Meth.* A887 (2018), pp. 184–192. arXiv: 1708.07931 [physics.ins-det].

[3] Aiwu Zhang and Marcus Hohlmann. "Accuracy of the geometric-mean method for determining spatial resolutions of tracking detectors in the presence of multiple Coulomb scattering". In: *JINST* 11.06 (2016), P06012. DOI: 10.1088/1748-0221/11/06/P06012. arXiv: 1604.06130 [physics.data-an].

[4] Aiwu Zhang et al. "R&D on GEM detectors for forward tracking at a future Electron-Ion Collider". In: *Proceedings, 2015 IEEE Nuclear Science Symposium and Medical Imaging Conference (NSS/MIC 2015): San Diego, California, United States*. 2016, p. 7581965. DOI: 10.1109/NSSMIC.2015.7581965. arXiv: 1511.07913 [physics.ins-det]. URL: http://inspirehep.net/record/1406551/files/arXiv:1511.07913.pdf.

[5] Aiwu Zhang et al. "Performance of a Large-area GEM Detector Read Out with Wide Radial Zigzag Strips". In: *Nucl. Instrum. Meth.* A811 (2016), pp. 30–41. DOI: 10.1016/j.nima.2015.11.157. arXiv: 1508.07046 [physics.ins-det].

INFN publications:

[1] J. Agarwala et al. "The MPGD-based photon detectors for the upgrade of COMPASS RICH-1 and beyond". In: *Nuclear Instruments and Methods in Physics Research Section A: Accelerators, Spectrometers, Detectors and Associated Equipment* (2018). ISSN: 0168-9002. DOI: https://doi.org/10.1016/j.nima.2018.10.092. URL: http://www.sciencedirect.com/science/article/pii/S0168900218314062.

[2] J. Agarwala et al. "Optimized MPGD-based Photon Detectors for high momentum particle identification at the Electron-Ion Collider". In: *Nuclear Instruments and Methods in Physics Research Section A: Accelerators, Spectrometers, Detectors and Associated Equipment* 936 (2019). Frontier Detectors for Frontier Physics: 14th Pisa Meeting on Advanced Detectors, pp. 565–567. ISSN: 0168-9002. DOI: https://doi.org/10.1016/j.nima.2018.10.185. URL: http://www.sciencedirect.com/science/article/pii/S0168900218314992.

[3] J. Agarwala et al. "A modular mini-pad photon detector prototype for RICH application at the Electron Ion Collider". In: *Journal of Physics: Conference Series* 1498 (Apr. 2020), p. 012007. DOI: 10.1088/1742-6596/1498/1/012007. URL: https://doi.org/10.1088/1742-6596/1498/1/012007.

[4] C. Chatterjee et al. "Nanodiamond photocathodes for MPGD-based single photon detectors at future EIC". In: *Journal of Physics: Conference Series* 1498 (Apr. 2020), p. 012008. DOI: 10.1088/1742-6596/1498/1/012008. URL: https://doi.org/10.1088/1742-6596/1498/1/012008.

[5] J. Agarwala et al. "Study of MicroPattern Gaseous detectors with novel nanodiamond based photocathodes for single photon detection in EIC RICH". In: *Nuclear Instruments and Methods in Physics Research Section A: Accelerators, Spectrometers, Detectors and Associated Equipment* 952 (2020). 10th International Workshop on Ring Imaging Cherenkov Detectors (RICH 2018), p. 161967. ISSN: 0168-9002. DOI: https://doi.org/10.1016/j.nima.2019.03.022. URL: https://www.sciencedirect.com/science/article/pii/S0168900219303213.

[6] J. Agarwala et al. "MPGD-based photon detectors for the upgrade of COMPASS RICH-1 and beyond". In: *Journal of Instrumentation* 15.09 (Sept. 2020), pp. C09063–C09063. DOI: 10.1088/1748-0221/15/09/c09063. URL: https://doi.org/10.1088/1748-0221/15/09/c09063.

[7] F.M. Brunbauer et al. "Nanodiamond photocathodes for MPGD-based single photon detectors at future EIC". In: *Journal of Instrumentation* 15.09 (Sept. 2020), pp. C09052–C09052. DOI: 10.1088/1748-0221/15/09/c09052. URL: https://doi.org/10.1088/1748-0221/15/09/c09052.

[8] S. Carrato et al. "A scalable High Voltage Power Supply System with system on chip control for Micro Pattern Gaseous Detectors". In: *Nuclear Instruments and Methods in Physics Research Section A: Accelerators, Spectrometers, Detectors and Associated Equipment* 963 (2020), p. 163763. ISSN: 0168-9002. DOI: https://doi.org/10.1016/j.nima.2020.163763. URL: https://www.sciencedirect.com/science/article/pii/S0168900220303016.

SBU publications:

[1] M. Blatnik et al. "Performance of a Quintuple-GEM Based RICH Detector Prototype". In: *IEEE Trans. Nucl. Sci.* 62.6 (2015), pp. 3256–3264. DOI: 10.1109/TNS.2015.2487999. arXiv: 1501.03530 [physics.ins-det].

TU publications:

[1] M. Posik and B. Surrow. "Construction of a Triple-GEM Detector Using Commercially Manufactured Large GEM Foils". In: 2018. arXiv: 1806.01892 [physics.ins-det].

[2] M. Posik and B. Surrow. "Construction of Triple-GEM Detectors Using Commercially Manufactured Large GEM Foils". In: *Proceedings, 2016 IEEE Nuclear Science Symposium and Medical Imaging Conference: NSS/MIC 2016: Strasbourg, France*. 2016, p. 8069743. DOI: 10.1109/NSSMIC.2016.8069743. arXiv: 1612.03776 [physics.ins-det].

[3] M. Posik and B. Surrow. "Optical and electrical performance of commercially manufactured large GEM foils". In: *Nucl. Instrum. Meth.* A802 (2015), pp. 10–15. DOI: 10.1016/j.nima.2015.08.048. arXiv: 1506.03652 [physics.ins-det].

[4] M. Posik and B. Surrow. "R&D of commercially manufactured large GEM foils". In: *Proceedings, 2015 IEEE Nuclear Science Symposium and Medical Imaging Conference (NSS/MIC 2015): San Diego, California, United States*. 2016, p. 7581802. DOI: 10.1109/NSSMIC.2015.7581802. arXiv: 1511.08693 [physics.ins-det].

[5] M. Posik and B. Surrow. "Research and Development of Commercially Manufactured Large GEM Foils". In: *Proceedings, 21st Symposium on Room-Temperature Semiconductor X-ray and Gamma-ray Detectors (RTSD 2014): Seattle, WA, USA, November 8-15, 2014*. 2016, p. 7431060. DOI: 10.1109/NSSMIC.2014.7431060. arXiv: 1411.7243 [physics.ins-det].

UVa publications:

[1] Kondo Gnanvo et al. "Large Size GEM for Super Bigbite Spectrometer (SBS) Polarimeter for Hall A 12 GeV program at JLab". In: *Nucl. Instrum. Meth.* A782 (2015), pp. 77–86. DOI: 10.1016/j.nima.2015.02.017. arXiv: 1409.5393 [physics.ins-det].

[2] Kondo Gnanvo et al. "Performance in test beam of a large-area and light-weight GEM detector with 2D stereo-angle (UV) strip readout". In: *Nucl. Instrum. Meth.* A808 (2016), pp. 83–92. DOI: 10.1016/j.nima.2015.11.071. arXiv: 1509.03875 [physics.ins-det].

Yale publications:

[1] S. Aiola et al. "Combination of two Gas Electron Multipliers and a Micromegas as gain elements for a time projection chamber". In: *Nucl. Instrum. Meth.* A834 (2016), pp. 149–157. DOI: 10.1016/j.nima.2016.08.007. arXiv: 1603.08473 [physics.ins-det].

References

[1] J. Agarwala et al. "The MPGD-based photon detectors for the upgrade of COMPASS RICH-1 and beyond". In: *Nuclear Instruments and Methods in Physics Research Section A: Accelerators, Spectrometers, Detectors and Associated Equipment* (2018). ISSN: 0168-9002. DOI: https://doi.org/10.1016/j.nima.2018.10.092. URL: http://www.sciencedirect.com/science/article/pii/S0168900218314062.

[2] M. Blatnik et al. "Performance of a Quintuple-GEM Based RICH Detector Prototype". In: *IEEE Transactions on Nuclear Science* 62.6 (2015), pp. 3256–3264.

[3] Luciano Velardi, Antonio Valentini, and Grazia Cicala. "UV photocathodes based on nanodiamond particles: Effect of carbon hybridization on the efficiency". In: *Diamond and Related Materials* 76.Supplement C (2017), pp. 1–8. ISSN: 0925-9635. DOI: https://doi.org/10.1016/j.diamond.2017.03.017. URL: http://www.sciencedirect.com/science/article/pii/S0925963516306999.

[4] C. Perez-Lara et al. "A Comparative Study of Straight-Strip and Zigzag-Interleaved Anode Patterns for MPGD Readouts". In: *IEEE Transactions on Nuclear Science* [Submitted for publication Jan. 2021] (2021).

[5] B. Azmoun et al. "Design Studies of High Resolution Readout Planes using Zigzags with GEM Detectors". In: *IEEE Transactions on Nuclear Science* (2020). Submitted to IEEE Transactions on Nuclear Science.

[6] B. Azmoun et al. "Design Studies for a TPC Readout Plane Using Zigzag Patterns with Multistage GEM Detectors". In: *IEEE Transactions on Nuclear Science* (July 2018), pp. 1–1. ISSN: 0018-9499. DOI: 10.1109/TNS.2018.2846403.

[7] *Simulations for sPHENIX TPC*. http://skipper.physics.sunysb.edu/~prakhar/tpc/HTML_Gating_RANDd/wires.html.

[8] *ScattPort is intended to be a Light Scattering Information Portal for the light scattering community*. https://scattport.org/index.php/light-scattering-software.

[9] *Electromagnetic Scattering by Particles and Surfaces*. https://www.giss.nasa.gov/staff/mmishchenko/related.html.

[10] T. Kawamoto et al. "New Small Wheel Technical Design Report". In: (June 2013).

[11] S. Aiola et al. "Combination of two Gas Electron Multipliers and a Micromegas as gain elements for a time projection chamber". In: *Nuclear Instruments and Methods in Physics Research Section A: Accelerators, Spectrometers, Detectors and Associated Equipment* 834 (2016), pp. 149–157. ISSN: 0168-9002. DOI: https://doi.org/10.1016/j.nima.2016.08.007. URL: http://www.sciencedirect.com/science/article/pii/S0168900216308221.

Appendices

A Appendix: MPGD sensors of single photons

Here, we present a brief introduction to two items related to INFN activity within eRD6, namely the principle and architecture of the MPGD sensors of single photons and the developments of new photocathode materials suitable for gaseous photon detectors.

A.1 The principle and architecture of the MPGD sensors of single photons and the related R&D

The concept of the hybrid MPGD detector of single photons has been developed in an eight-year R&D program; the requirements for the upgrade of the gaseous RICH counter of the COMPASS experiment at CERN SPS are the reference that guided this development. The resulting detectors have been successfully in operation at COMPASS since Spring 2016 [1]. The detector architecture (Fig. 50) consists in three multiplication stages: two THick GEMs (THGEM) layers, the first one coated with a CsI film and acting as photocathode, followed by a MicroMegas (MM) multiplication stage. The two THGEMs are staggered: this configuration is beneficial both to reduce the Ion BackFlow (IBF) and to increase the maximum gain at which the detector can be operated exhibiting full electrical stability. These photon detectors are routinely operated at gains of 1.5×10^4 and exhibit an IBF rate lower than 3%. The gas mixtures used are by Ar and CH_4, with a rich methane fraction in order to maximize the photoelectron extraction. An original element of the hybrid MPGD photon detector is the approach to a resistive MM by discrete elements (Figure 51), which has been triggered by the resistive MM developed for the ATLAS experiment at CERN LHC [10], even if there are substantial differences. The anode elements (pads) facing the micromesh are individually equipped with large-value resistors and the HV is provided, via these resistors, to the anode electrodes, while the micromesh is grounded. A second set of electrodes (pads parallel to the first ones) are embedded in the anode PCB: the signal is transferred by capacitive coupling to these electrodes, which are connected to the front-end read-out electronics. The advantages of the design shortly described above are several:

- As in ATLAS resistive MM, applying the HV to the anode instead of to the MM cathode results in

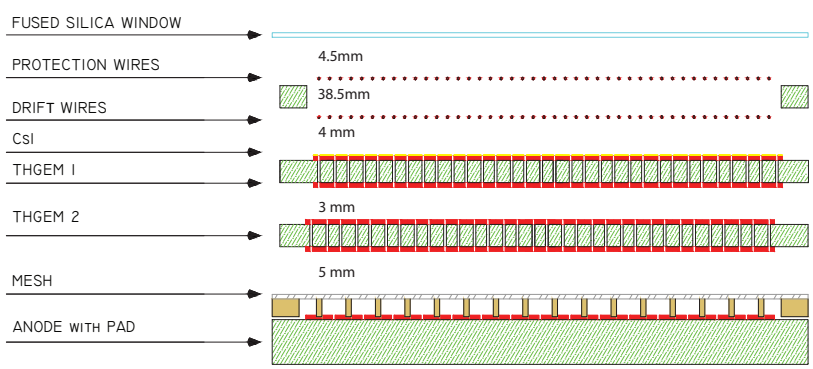

Figure 50: Sketch of the hybrid single photon detector: two staggered THGEM layers are coupled to a resistive bulk MM. Image not to scale.

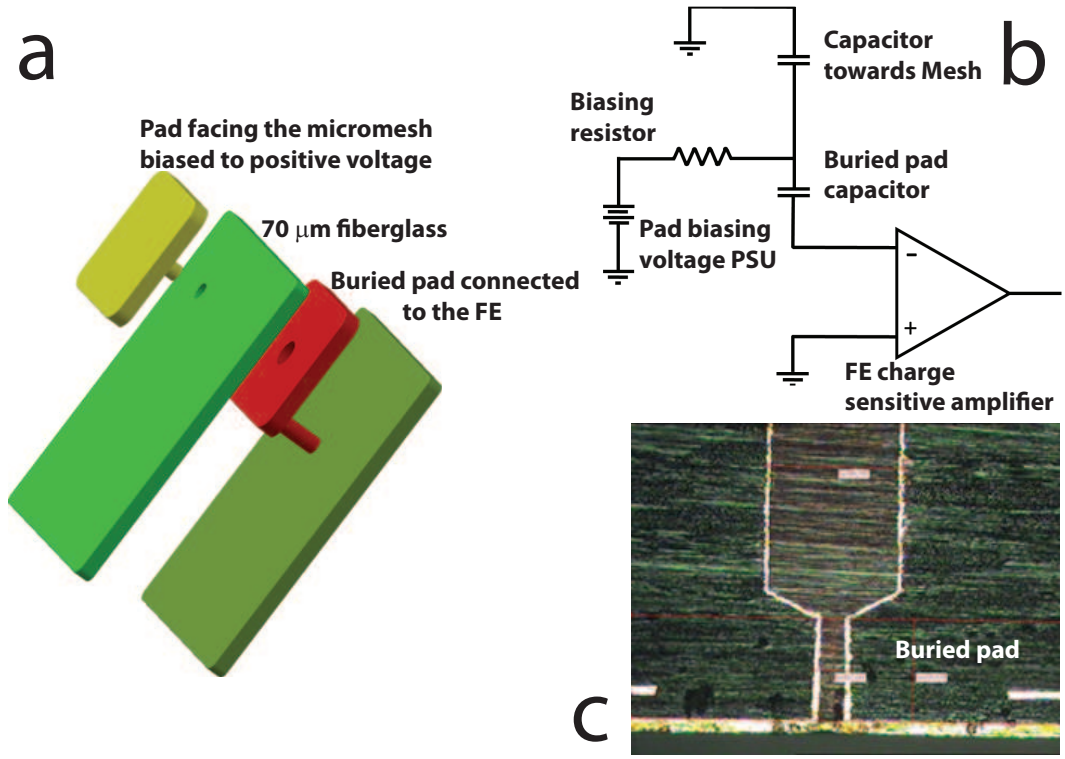

Figure 51: a) Sketch of the capacitive coupled readout pad. The biasing voltage is distributed via independent 470 MΩ resistors to the pad facing the micromesh structure (yellow pad in the sketch). The buried pad (red pad in the sketch) is isolated via 70 μm thick fiberglass and connected to the front end chip. b) Schematic of the capacitive coupled pad principle illustrated via discrete element blocks. c) Metallography section of the PCB: detail of the through-via connecting the external pad through the hole of the buried pad. The reduced diameter of the through-via reaching the external pad contributes preserving the pad planarity.

larger amplitude signals;

- In case of local defects of the MM, a single electrode can be isolated resulting in a dead area as large as the electrode itself, while the large majority of the detector is still active;
- No resistive coating is present inside the detector volume;
- The absence of a resistive layer on top of the anode electrodes is limiting the degradation of the dE/dx information in the collected signals.

The hybrid detector concept can be further improved in order to match the requirements of high momenta hadron identification at EIC; this challenging task requires:

1. Limited radiator length of the order of 1 m: here one of the most promising approaches is the windowless RICH concept [2];
2. Fine space granularity to cope with the modest lever arm related to the radiator length;
3. Control of the IBF rate in order to guarantee stable detector performance over time;
4. Further improvement in the engineering aspects in order to improve the detector robustness, simplify the construction and control the costs;

5. The comparison between hybrid detectors where THGEMs or GEMS in view of an overall optimization of the detector principle;
6. the identification and validation of an appropriate front-end ASIC for the use of these photon detectors in ten years from now.

The R&D program has progressed with the goal of matching the requirements listed above, while a summary of the performed activity is listed in the following.

- Test of novel materials for THGEM substrate to simplify the detector construction, increase the yield of valid large-size THGEMs and, thus, control the detector costs *(related to requirement 4)*;
- The development of resistive MM by discrete elements with miniaturized pad size in order to obtain finer space resolution *(related to requirement 1)*; a prototype has been built (Fig. 52), characterized by laboratory exercises and at a test beam data taking, where Cherenkov photons have been detected (Fig. 53); a dedicated DAQ system has been developed for the test beam studies, designed to increase the data bandwidth from the SRS read-out; a second version of the prototype aimed at improving its performance has been designed and it is ready for construction;
- The VMM3 ASIC is a novel chip designed for MPGDs with features promising for our application. In fact, the low noise figure and the capability of effective coupling with detectors in a wide capacity range are specifically beneficial to our single photon detection application, namely an application requiring single photoelectron detection, performed by a hybrid MPGD where the last multiplication stage is by a MICROMEGAS, namely a relatively high capacitance detector. Moreover, the chip architecture is designed for trigger-less operation, namely adequate for usage in up-to-date DAQ systems. We have acquired two pieces of the MMFE1 board, a VMM read-out board developed in the context of the ATLAS NSW project, design to exploit all the most relevant VMM3 features, including the good noise figures. In parallel, we have designed a dedicated MICROMEGAS prototype, designed according to our architecture of resistive micromegas changing the connectors so that part of the detector can be read with the MMFE1 board and part using an SRS-APV25 card in comparative exercises The PCB design is now ready for submission. This activity is *related to requirement 6*.

It is relevant to underline that the further development of the hybrid detector concept, in particular low IBF rate is **synergic** to another sector of activities within eRD6, namely the **read-out sensors for the TPC**. A hybrid MPGD approach to TPC read-out has already been proposed making use of traditional non-resistive MMs[11]; our approach to resistive MM can offer a detector which exhibits robust electrical stability while preserving a good dE/dx resolution.

A.2 The developments of new photocathode materials suitable for gaseous photon detectors

This activity consists in initial studies to understand the compatibility of an innovative photocathode material with the operation of gaseous detectors as well as in progressing in the characterization of the photoconverter itself.

The option of using innovative photoconverters in gaseous detectors is a strategic one. In fact, so far, the only photoconverter compatible with large-size, operative gaseous detector is CsI. Despite remarkable successful applications (for instance the read-out sensors of the ALICE RICH, the COMPASS RICH and the PHENIX HBD), the use of CsI in gaseous detector suffers from some intrinsic limitations: ageing, causing a severe decrease of the quantum efficiency after a collected charge of the order of some mC/cm^2 and long recovery time (about 1 day) after an occasional discharge in the detector. These limitations are related to the photon feedback from the multiplication region and to the bombardment of the CsI photocathode film by positive ions generated in the multiplication process. They impose to operate the detector at low gain, reducing the efficiency of single photoelectron detection. Alternatively, great care is required to reduce photon feedback

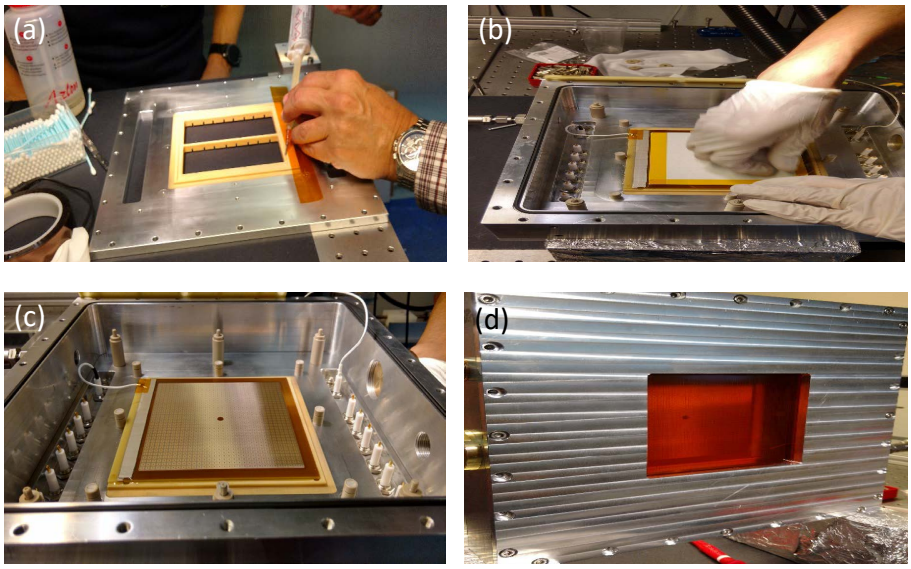

Figure 52: Prototype construction. (a) The fiberglass frame supporting the MM is glued onto the Al chamber structure. (b) The MM is glued onto the fiberglass frame. (c) The MM installed in the chamber and its power lines are visible. (d) The chamber is closed with a mylar window.

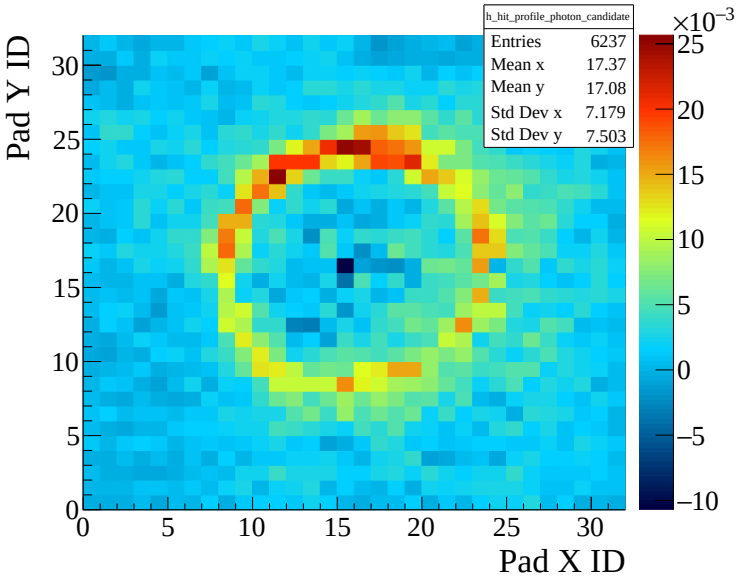

Figure 53: 2-D histogram of the difference between the 2-D histograms for events collected with the shutter between the radiator and the photocathode open and closed. The histogram population has been normalized with the ratio of the number of events in the two samples.

and ion bombardment. Moreover, CsI is chemically fragile: if exposed, even for short time, to atmospheres with water vapor, the molecule is broken and therefore the QE is lost. This feature imposes to assemble the photon detectors in clean, controlled atmospheres, making the overall detector construction tedious and complex. Therefore, the possibility of an alternative photocathode material adequate for gaseous detectors can represent a relevant step forward in the field of these sensors.

The Quantum Efficiency (QE) of photocathodes by NanoDiamond (ND) particles rich in graphite have been measured in vacuum [3]: when the photocathode is hydrogenized, QE as high as 47% at 140 nm has been measured; globally, the quantum efficiency is non-negligible in the VUV domain, below 210 nm. High QE-values have been measured both performing the hydrogen plasma treatment in situ, namely after coating the substrate with the photocathode film, and hydrogenated the ND powder before coating the substrate with the photoconverting layer. The latter option is of great interest for gaseous photon detectors: if fact, the hydrogen plasma treatment requires high temperature (> 850 ^{o}C), not compatible with the components of gaseous detectors. When the ND powder is hydrogenated before the cathode coating, the spray procedure by an ultrasonic atomizer used to form the photocathode does not require temperatures exceeding 120 ^{o}C: this is compatible with gaseous detector components. Preliminary tests of mechanical attachment of the photocathode and aging due to exposure to air indicate that this photocathode material is robust.

Two principle difficulties must be considered in the context of the ongoing studies:

- The ND powder provided by the producers is a cheap material not selected according to the graphite content or the grain size; therefore, several different samples have to be purchased and then the graphite-rich ones have to be selected by Raman spectroscopy; no exact reproducibility of the raw material from producers can be envisaged at the moment;
- using the present set-up for the formation of photocathodes by the spray technique, the maximum photocathode size is of about 4 cm^2.

This activity has been ongoing since year 2018. A short summary of the exercises performed is listed in the following.

- In 2018 and in 2019, two series of small-size (3×3 cm^2) THGEMs have been coated with ND powder films, both hydrogenated and not hydrogenated; these electron multiplications have been characterized before and after applying the coating to comparatively access the effect of the photocathode on their performance as multipliers; after initial difficulties, an after-coating protocol has been established and the THGEM performance in terms of gain and stability is largely unmodified when coated.
- The effective Quantum Efficiency (QE) is a key parameter for the performance of gaseous photon detectors. The effective QE in gas has been measured by several groups and reproduced in simulation studies where the back scattering by the gas molecules is taken into account. We have started exercises to measure the effective QE in gasses of interest when HND photocathodes are used. When the measurement campaign is completed, we will verify if the back scattering by the gas molecules is adequate to describe the effective QE also for the novel photoconverter. The preliminary measurements indicate an evolution versus the electric field in front of the photocathode similar to that observed for CsI. This campaign of measurement has to be continued.
- The production of THGEMs formed by two layers, each one of thickness one half that of the final THGEM has been attempted. The goals was the possibility to coat one of the two surfaces using only a half THGEM, then combining the two parts in order to avoid coating inside the hole that can create shorts between the two THGEM face. The exercise was not successful.
- The effective QE versus the number of spray shots has been measured: it saturates at 50 spray shots.
- The exploration of the characteristics of the ND powder used as photo-converters is ongoing. The QE obtained using powders with different grain size has been measured. For small grain-size (a few nm) the QE is low. It increases with grain size up to sizes of about 50 nm. It does not increase further for larger grain-sizes.

B Appendix: UVa

B.1 Performance of the large-pad capacitive-sharing readout in beam tests

Hall D Pair Spectrometer Electron beam

The PS electron beam has an energy range of 3 to 6 GeV. The spatial coverage of the beam is shown on the hit map plots of Fig. 54 with a wide angular coverage in the horizontal axis from 6.75 degree to 7.5 degree in the horizontal direction but a smaller angle of 2 degree with a narrower distribution in the vertical direction as shown on Fig. 55. The impact of the angular distribution on the spatial resolution performances in the horizontal (x-axis) and vertical (y-axis) directions is clearly seen on the data of Fig. 30 of section 4.2.3 with the spatial resolution is better in y than in x.

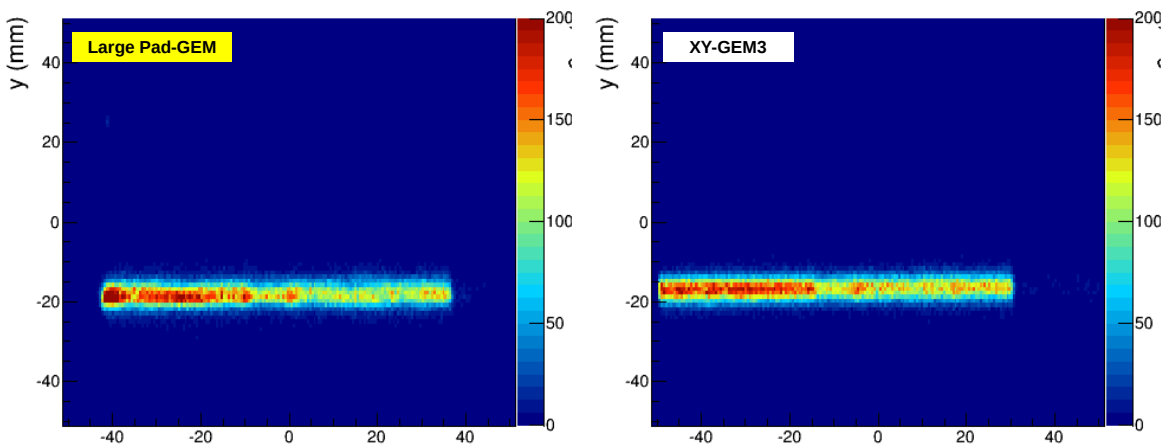

Figure 54: 2D beam profile of Hall D electron beam on the capacitive-couple large pad GEM and ***(left)*** and one of the GEM tracker ***(right)***.

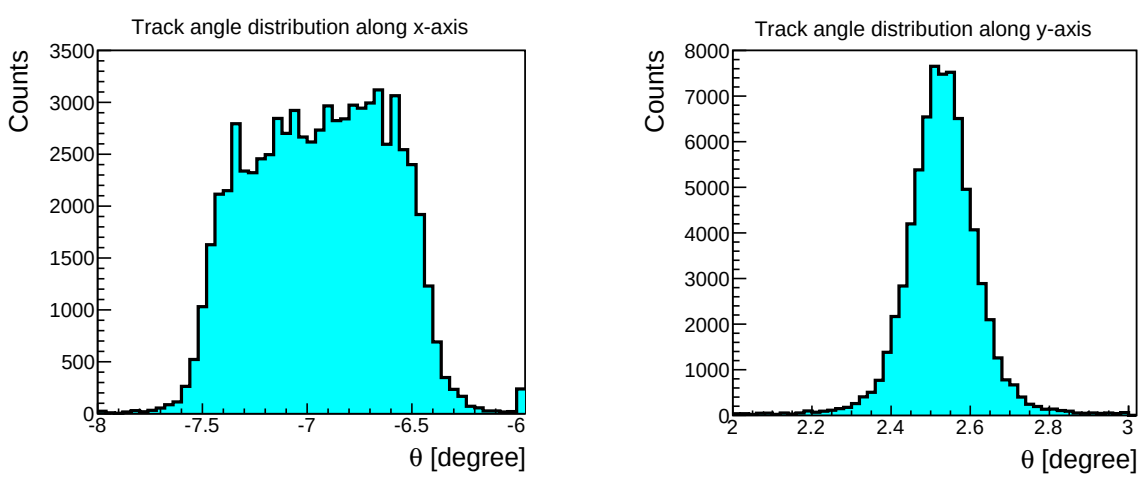

Figure 55: Angular distribution in horizontal ***(left)*** and vertical ***(right)*** directions of the reconstructed electron tracks from the 4-GEM trackers.

Analysis of beam test data

Definition of the cluster pattern: The way the cluster of pads for a triggered event is formed had a significant impact on the spatial resolution performances. As a consequences, we study the impact of different cluster patterns on the characteristics of the large-pad capacitive-sharing GEM prototype including cluster size and spatial resolution. Fig. 56 shows six the cluster patterns that we tested. For each pattern and for each triggered event, we first select the pad with the highest ADC values (shown in red on Fig. 57), which is defined as the central pad of the cluster, then, we form the cluster by selecting a set of neighboring pads around the central pad and with ADC value above pedestal threshold. The selected pad should be part of the given pattern. Each pattern then defines the maximum number of pads in the cluster for a given event starting from the simplest pattern #1 of Fig. 57), with the four immediate neighboring pads around the central pad, to the larger cluster pattern #6 with allow up to 25 pads to form the cluster. It is worth noting that the cluster pattern does not define minimum number of pads required to form the cluster good cluster but rather the maximum number of pads.

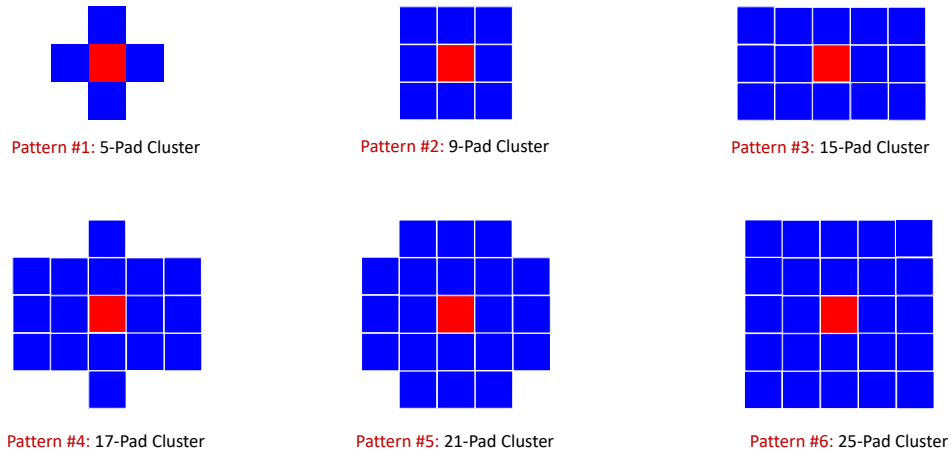

Figure 56: Different cluster patterns for the 2D position reconstruction for efficiency and spatial resolution analysis of the test beam data.

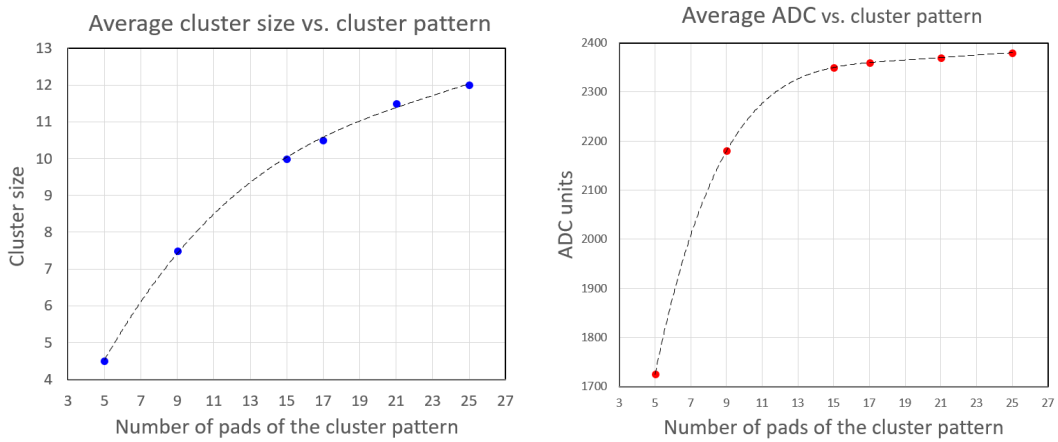

Figure 57: ***Left:*** Cluster size (average number of pads in the cluster per event) as a function of the maximum number of pads in cluster patterns as defined in Fig. 56; ***Right:*** Average cluster charges in ADC units as a function of the maximum number of pads in cluster patterns.

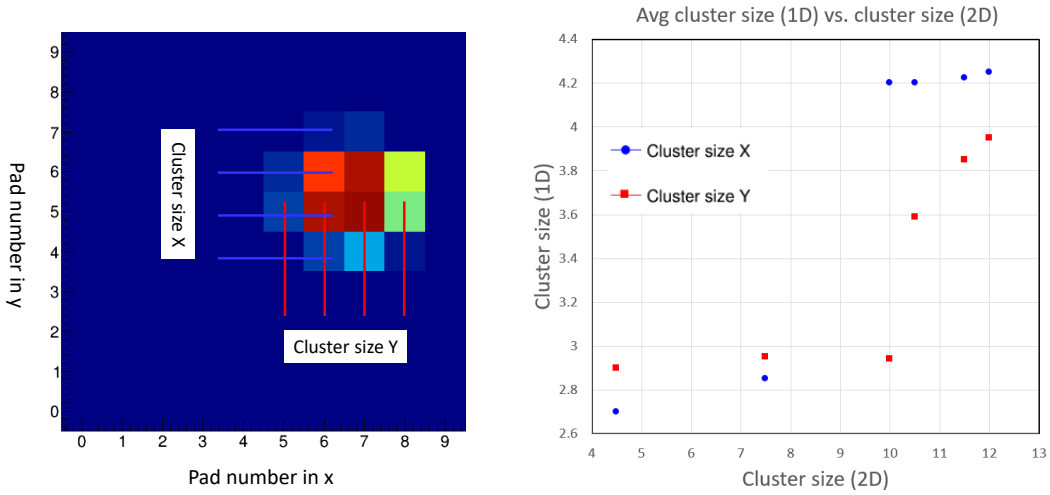

Figure 58: ***Left:*** Definition of the cluster size in x and y. ***Right:*** Cluster size in x and y as a function of the cluster size.

Cluster size vs. cluster pattern: The cluster size is plotted as a function of the maximum number of pads of the cluster pattern as shown on the left plot of Fig. 57. The cluster size is defined as the average number of pads above pedestal threshold. The cluster size obviously increases as the maximum allowed number of pads increases. This means that even for pad size as big as 1 cm $\times$ 1cm, the signal is spread in a large number of pads as expected for this R&D project. The cluster charges in ADC units as a function of the cluster size for different cluster pattern is shown on the right plots of Fig. 57. A plateau is reached for cluster size $\geq$ 10 for cluster pattern #3. For cluster pattern above pattern #3, we observe a 20% increase in the cluster size from an average 10 to 12 pads but just 3% increase in the cluster charge. This is an indication that the additional pads contributing to the cluster for patterns #4, #5 #6 compared to pattern #3 have negligible contribution to the total cluster's total charges and the source of this contribution is probably not from the detector signal but rather from cross talk or high noise pads. This observation is later confirmed by the degradation of the spatial resolution performances observed on the plots of Fig. 61 where the spatial resolution in both x and y increases significantly for cluster pattern $\geq$ #4 after reaching a minimum at cluster pattern #3 corresponding on the plots to maximum number of pads = 15 and cluster size = 10 on the the x-axis of both plots respectively. We also looked at the cluster size along x and y, defined as the average number of columns and rows with pads above pedestal threshold per event in x and y respectively (see cartoon on the left of Fig. 58). The dependence of the cluster size in x and y as a function of the cluster size is shown on the plot on the right of Fig. 58. As expected, the cluster size in x and y are strongly correlated to the maximum required pad columns or rows for each cluster pattern of Fig. 56. The cluster size in x is between 2.7 below 3 for the first two patterns when the requirements is limited to 3 columns and jumps above 4.2 for the last four cluster patterns when the requirements is set to 5 columns. In the y-direction, the average cluster size is around 2.9 for the first three patterns with a maximum required rows equal to 3 rows. However, the cluster size in y remained smaller to 4 even for the last three patterns which have a requirement of 5 rows. The overall smaller cluster size in y ($\leq$ 4) for patterns #4, #5 and #6 compared to the cluster size in x is due to angular distribution of the incoming electron beam in x and y (see Fig. 55). From the angle distribution in x and y, we expect the number of pads with signal above pedestal to be larger in the x direction than in y and poorer resolution in x than in y as observed on Fig. 30 of section 4.2.3 and Fig. 61 for cluster size $\leq$ 12 (or maximum number of in cluster pattern $\leq$ 15).

Cluster size vs. HV: The plots on the left of Fig. 59 show the average cluster size (total number of pads) and on the right, the cluster size in x and y as a function of the average voltage applied (HV) to the GEMs. We studied the the cluster size dependence on the GEM HV for different zero suppression threshold calculated from the pedestal noise4.2.3. Three threshold values ($0 \times \sigma$, $3 \times \sigma$ and $5 \times \sigma$) have been applied

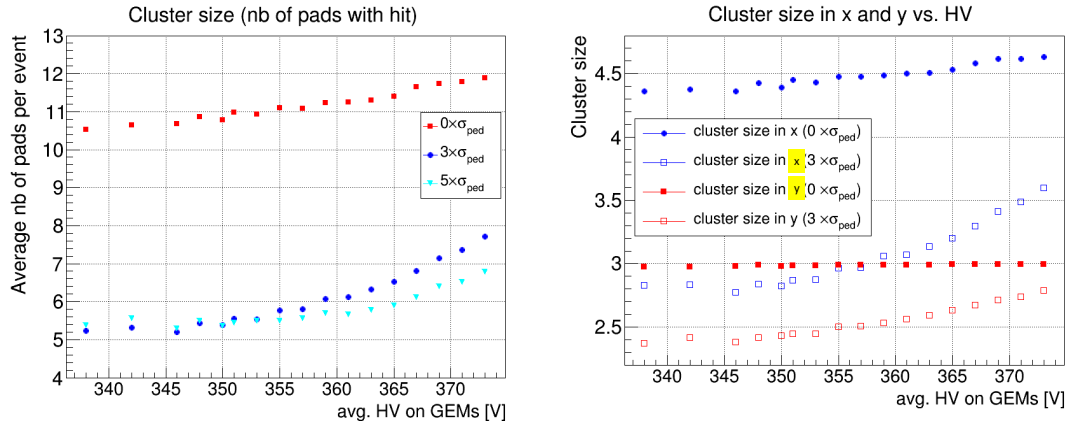

Figure 59: ***Left:*** Cluster size as a function of the average HV applied to the 3 GEM foils for pedestal cut: [0σ] ***(red)***, [3σ] ***(blue)*** and [5σ] ***(cyan)***. ***Right:*** Cluster size in x ***(blue)*** and y ***(red)*** direction as a function of the average HV on the GEM foils for [0σ] ***(full)*** and [3σ] ***(open)***.

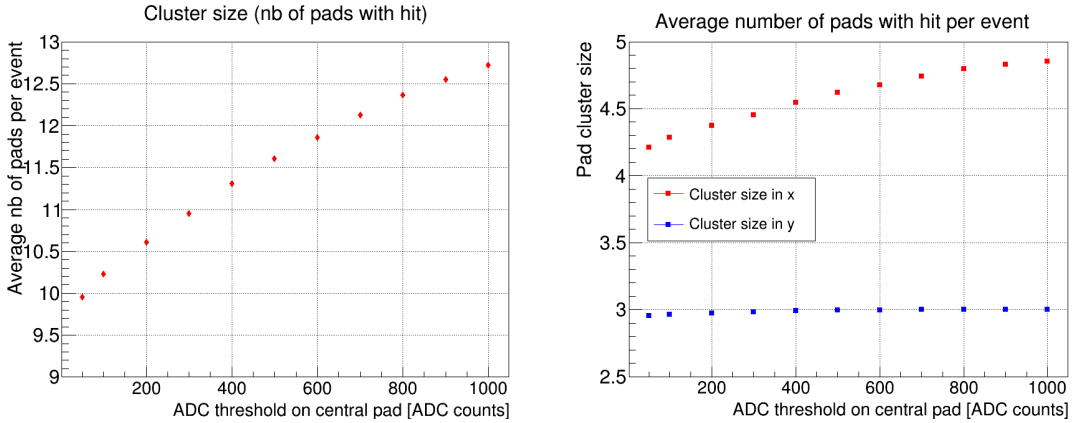

Figure 60: ***Left:*** Cluster size as a function of the minimum signal amplitude requirement (in ADC units) of the cluster central pad. ***Right:*** Cluster size in x ***(red)*** and y ***(blue)*** as a function of the minimum signal amplitude requirement on the cluster central pad.

for the cluster size as shown on the plots on the left. A threshold set to $0 \times \sigma$ corresponds to the case where only the pads with "negative" ADC value after the subtraction of the pedestal offset for each individual APV25 channel are removed from the analysis. As shown on the data plots of Fig. 59 the average cluster size is significantly higher for $0 \times \sigma$ threshold than for $(3 \times \sigma)$ or higher threshold as shown on the left plot for average cluster size (2D) on the right for the average cluster size in x and y. Moreover, the cluster size in y is quasi independent of the HV applied to the GEMs and increases only slightly in x direction with the HV when the threshold set to $0 \times \sigma$ is applied while it increases exponentially with the HV for $3 \times \sigma$ or higher threshold. Moreover, since the cluster size in y is independent from the HV applied to the GEMs for threshold set to $0 \times \sigma$, the cluster size (2D) dependence on the HV on the GEMs is dominated by the cluster size in x dependence on the HV on the GEMs. The difference in the average cluster size in x $\sim$4.5 and $\sim$3 respectively for threshold set to $0 \times \sigma$, is once again explained by the different angular distribution of the beam in x and y. Fig. 60 shows the average cluster size on the left plot and the cluster size in x and y on the right plot as a function of a ADC threshold requirement on the cluster's central pad. Imposing ADC threshold requirement on the central pad is another way to study the dependence of capacitive-sharing pad

readout properties with the detector gain in order to optimize spatial resolution of the readout structure. The plot of the left on Fig. 60 shows a steady increase of the cluster size from ∼10 pads to ∼12.5 pads when the minimum ADC requirement for the central pad varies from 50 to 1000 ADC units. The detector efficiency drops from ∼97% to ∼33% when we applied the 100 ADC threshold to the central pad because for the current test beam setup, prototype was not optimized to operate at such high gain. The plots on the right of Fig. 60 are the breakdown of the average cluster size in x and y. The plots shows once again that the dependence of the cluster size with the minimum ADCs requirement is dominated by its contributions along the x-direction and therefore by the incoming particle angle. The average cluster size in y is equal to 3 and is independent from the minimum ADC requirement on the central pad even for small charges released by the incoming particle. For a minimum 50 ADCs requirement on the central pad, the cluster size is equal to 9.9 on the left plots, hitting on average 4.2 pads columns in x and 3 pad rows in y. This is a validation of the capacitive coupling as a way to achieve charge sharing for large pad readout structure.

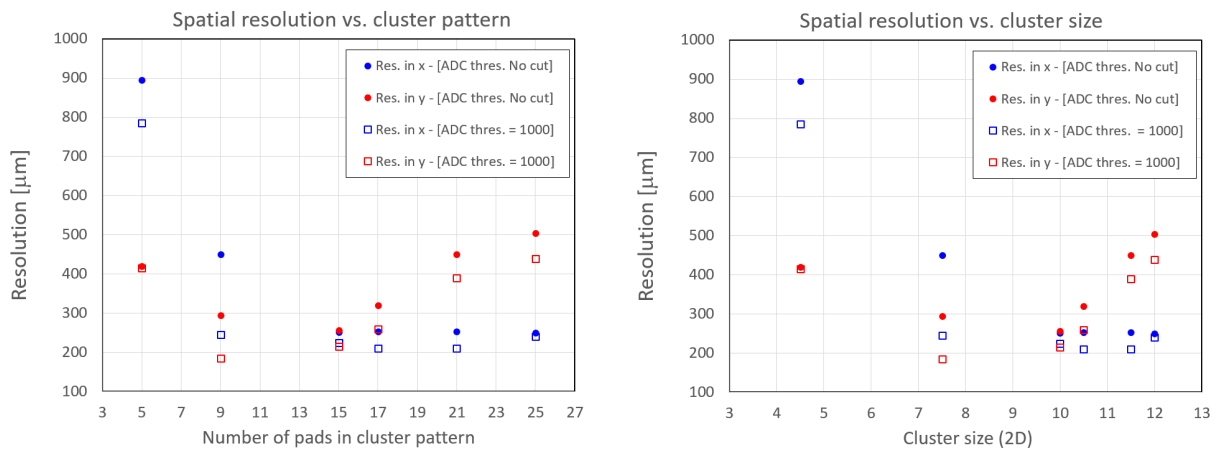

Figure 61: Spatial resolution in x (*blue*) and y (*red*) vs. the maximum number of pads of the cluster pattern ***(left)***; vs. the cluster size for each pattern ***(right)***. On each set of plots, data with: no requirement on the minimum ADCs of the central pad ***(solid circle)*** and minimum of 1000 ADCs requirements for the central pad ***(open square).***

Spatial resolution vs. cluster pattern: The dependence of the spatial resolution on the cluster pattern as defined in Fig. 56 is shown on Fig. 61. The left plots show the spatial resolution as a function of the maximum number of pads in the pattern and the left plots, as a function of the average cluster size associated to each defined pattern. Each set of plots shows the the spatial resolution in x (blue) and y (red) with no requirement on the minimum ADCs of the central pad *(solid circle)* and with a minimum of 1000 ADCs requirements for the central pad *(open square)*. The plots shows that the resolution in x and y are optimal (minimal) with cluster pattern 3 corresponding to a maximum number of pads equal 15 and an average cluster size ∼10 pads except for the resolution in y ∼187 μm for cluster pattern 2 with maximum number of pads equal 9 and an average cluster size ∼7.5 pads and in x ∼212 μm for cluster pattern 4 with maximum number of pads equal and an average cluster size ∼10.5 pads when the minimum requirements on the central pad charges is set to 1000 ADCs. The dramatic increases of the resolution in y with the cluster pattern when the maximum number of pad is $\geq$ 15 is explained by the fact when the number of pad rows is larger than 3, the contribution of the pads of the additional rows very likely comes from cross talk effect of noisy pads. Because of the size of the pads and the use of the centre of gravity algorithm for the calculation of the position coordinates, even a small contribution in ADCs of noisy pads or cross talk pads have a significant impact on the resolution. Conversely, when the cluster pattern fail to include some pads with ADC contribution to the signal as it is the case for the first two patterns, the negative impact on the spatial resolution performance is dramatic as one can see for cluster pattern 1 which includes only the direct neighboring pads of the central pads, the spatial resolution in x and y is equal to ∼900 μm and ∼420 μm respectively when no minimum ADCs requirements is applied. This is more than 4 times worse than the best results we obtain in x for

cluster pattern 4 where the resolution is ∼212 μm. The resolution in x is significantly worse than in y for the first two cluster pattern because of different angular distribution of the incoming track. Large angle in x means that the track spread on more pads and therefore a cluster pattern restricting the maximum allowed pads to be consider will results in significantly worse resolution performances.

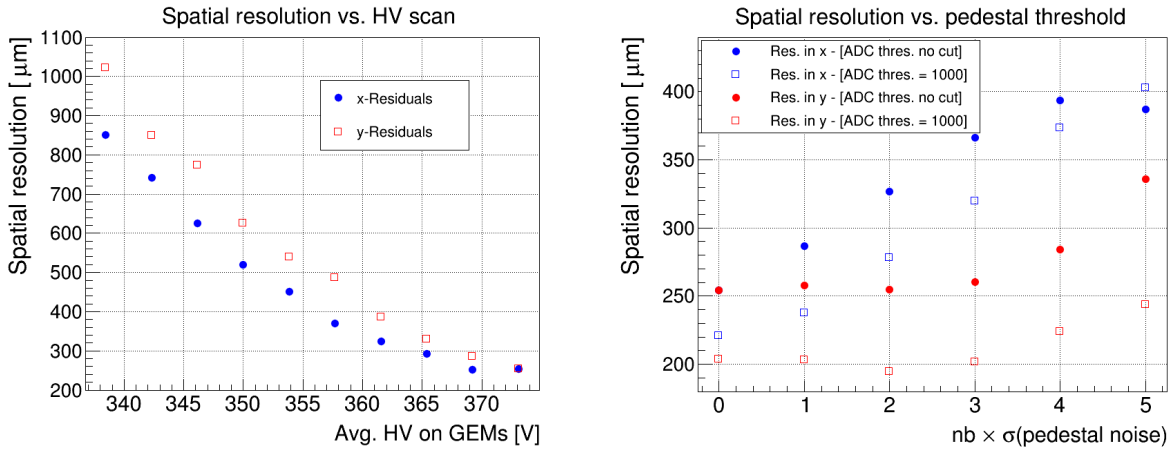

Figure 62: ***Left:*** Spatial resolution in x (*blue full circle*) and y (*red open square*) as a function of the average voltage applied to the GEM foils. ***Right:*** Spatial resolution in x (*blue*) and y (*red*) as a function of the zero suppression cut with: no requirement on the minimum ADCs of the central pad ***(open square)***; minimum $\geq$ 1000 ADCs requirements for the central pad ***(full circle)***.

Spatial resolution vs. HV on GEMs: The left plot of Fig. 62 shows the spatial resolution in x and y of the capacitive-sharing pad-GEM prototype as a function of the average HV applied to the GEMs. The resolution vs. HV plots was produced for the cluster pattern #3 at [0 × σ] pedestal cut. This is best configuration that yields the best spatial resolution in both x and y direction. The spatial resolution is around 250 μm in both x and when the detector is operating at full efficiency plateau corresponding to HV = 374V on average on the GEMs. This voltage on the GEMs correspond to a total amplification gain of around 8000 for a standard triple-GEM detector with single-mask GEM foils. As expected, the spatial resolution performances quickly degrade at lower gain, increasing to 0.86 mm and 1 mm respectively for x and y for the HV of ∼335V on the GEM foils. The right plot of Fig. 62 shows the variation of spatial resolution as a function of the zero suppression threshold expressed as number of the pedestals rms of the APV25 channels. Data corresponding to no minimum ADC requirement (solid dots) and 1000 ADCs minimum requirement for the cluster's central pad (open dots) are shown on the plots. For the y-direction, in both cases, the spatial resolution is independent of the pedestal cut up to 3σ around ∼250 μm for no minimum requirement and ∼187 μm with minimum requirement 1000 ADCs on the central cluster at 2σ cut. This is because, with particles incoming at smaller angle in y-direction, the cluster charges are mostly concentrated on 3 pads rows as shown on Fig. 59 and Fig. 60 with the average charge per pads high enough to be insensitive on the pedestal cut below 3σ. The resolution in y only starts degrading for pedestal cut $\geq$ 3σ when the cut start suppressing pads with signal. The situation is quite different for the resolution performance in x. In this case, because of the large angle of the incoming electrons, the cluster charges are spread om many more pads, 4.6 pads on average with the average charges per pads significantly smaller than in the y direction. In this case, the resolution in x is very sensitive to the pedestal cut even for smaller number of σ. The optimal results for the spatial resolution in x is obtain for 0 × σ reaching ∼250 μm for no minimum requirement and ∼212 μm with minimum requirement 1000 ADCs on the central cluster.

B.2 Development of capacitive-sharing large-pad anode readout

We have been developing a new concept of pad readout PCB as anode readout for MPGD technologies that, by design combine the advantages of providing excellent spatial resolution performances i.e. better than 100 μm with large side pad greater than a few cm^2 and therefore considerably reducing the number of electronic channels required to readout large area MPGD detectors such as the ones under investigations for EIC various tracking systems. The basic principle is illustrated on the sketch of Fig. 63 and is based on

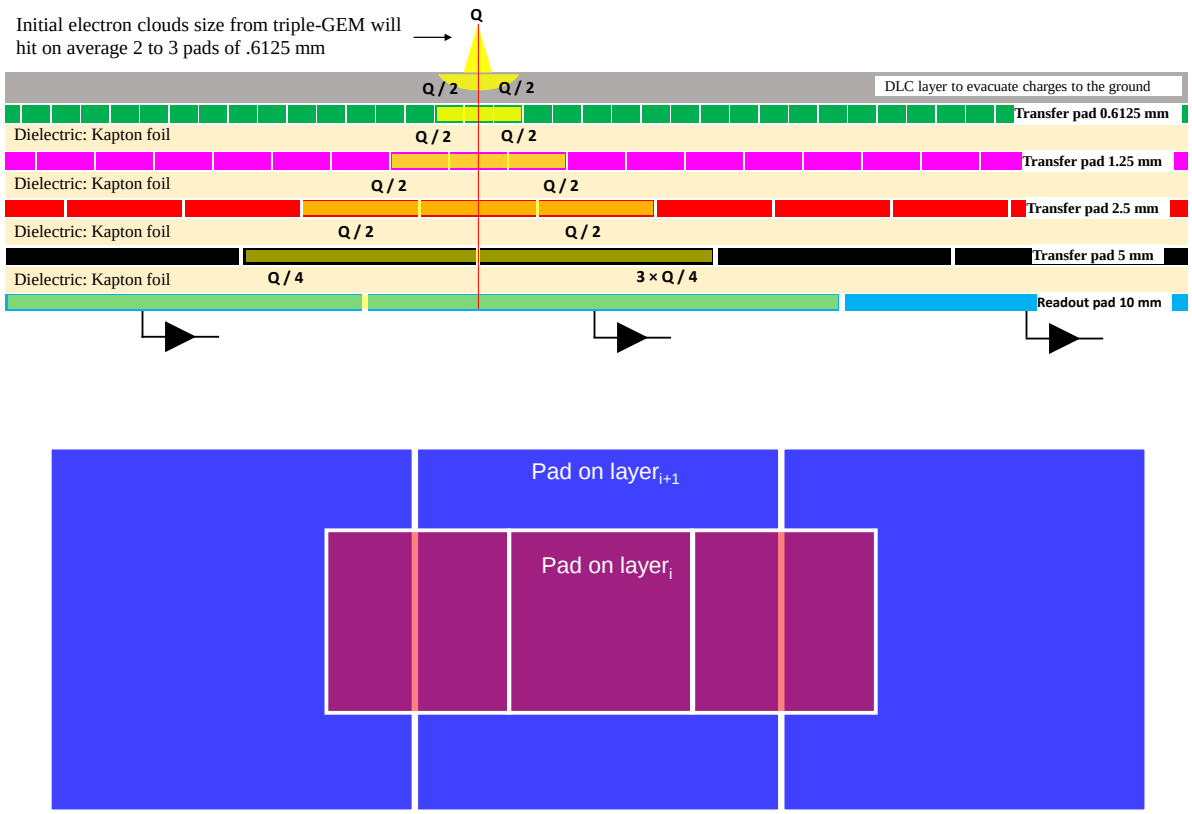

Figure 63: Principle of capacitive-coupling large-pads anode readout for MPGDs; *top:* cross sectional view of the 5-layers capacitive sharing readout board; *bottom:* principle of charge sharing between two layers of the 5-layers capacitive sharing readout board

vertical stack of square Cu-pad layers, separated by 50 μm thick kapton foils as dielectric to form a capacitor. The pad size doubles (and subsequently the area is multiplied by 4) from a one layer (layer layer[i]) to the layer[i+1] underneath it. Each pad of layer[i] is arranged is space so that its center is either always perfectly aligned with the center of a larger pad of layer[i+1] or with the boundary between of two adjacent pads of layer[i+1]. This space arrangement of the pads from one layer to the other ensured that the charges collected by two adjacent pads of layer[i] are always transferred to two adjacent pads of layer[i+1] no matter how the size of the pads of layer[i+1]. The charge are transferred between layers via capacitive coupling as two Cu-pad layers separated by the kapton foil acts effectively a perfect capacitor. The pads of the bottom layer[n], that we name here *charge-collection layer* are connected to the front end (FE) electronics readout, while all the other pad layers above, that we name here *charge transfer layers* just serve to transfer and spread the original charges through capacitive coupling. With such scheme the area a[n] of the pad of the

charge-collection layer (layer[n]) in a n-layer-stack readout board is equal to a[1]$\times 2^n$ with a[1] being the area of the pad of the top *charge transfer layer* (layer[1]) and the total number of pads of layer[n] is $1/2^n$ of the total number of pads of layer[1]. By design, the top layer pad size of this readout board basically defines the spatial resolution performances of the pad readout scheme and in effect which is transferred via capacitive coupling the bottom layer which pad size define the total number of channel count to be read out. With this scheme, in the first order, the spatial resolution performances is decoupled from the size of the readout layer pads connected to the FE readout electronics. So, for example, a 5-layers large-pad readout PCB with a pad size of 0.06125 cm $\times$ 0.06125 cm for the top layer will have a pad size equal to 1 cm $\times$ 1 cm for the bottom layer for the charge collection which will only require 100 channels to be read out in a standard 10 cm $\times$ 10 cm Triple-GEM detector configuration. This is **5 time less channels that the standard 2D X-Y COMPASS strips readout** which require 512 channels to achieve similar spatial resolution performance .

B.3 Minimization of capacitance noise and cross talk

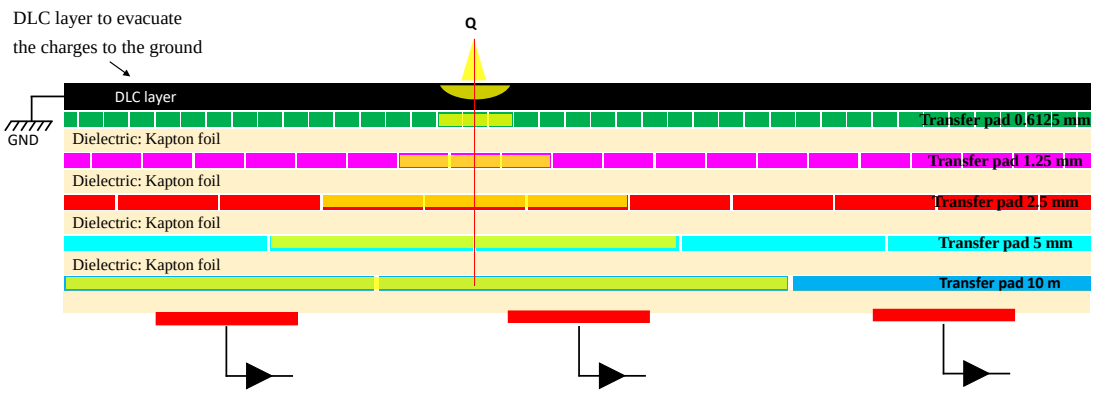

Figure 64: Sketch of a large-pad capacitive-coupling readout board with 4 quadrants, each with a different pad design to study the capacitance noise and cross talk effect.

We are also investigating ways to reduce the cross talk and capacitance noise induced by the large readout pads (inter-pad capacitance and cross talk) as well as between pads from different layers. This is crucial to maintain the spatial resolution performances as well as the efficiency of the detectors. The first study aims to address the inter-pad capacitance induced noise of the *charge-collection layer*. The idea is to add one additional pad layer to collect the signal but with smaller pads size as shown on the sketch of Fig. 64. This scheme will significantly decrease the inter-pad capacitance noise and cross talk between pads while we maintain the charge sharing capabilities therefore the spatial resolution performances. However the amplitude of the signal collected by the FE pre-amplifier will be significantly smaller, however we could easily compensate the signal to noise ratio by increasing the gain of the detector by increasing the GEM or μRWELL amplification gain. Another area is to actually study various pad design as shown on the right side of the cartoon of Fig. 65 with the spiral like square pad pattern to reduce the area of the large pads. This will help further with both cross talk and capacitance noise reduction. We plan to test on a single readout board 4 patterns with same pad pitch in 4 quadrants of the active area. the top left will be the standard readout large plain Cu-pad, the bottom will have the plain Cu pad but signal collected by the smaller pad size as descried on Fig. 64. On the top right, we will look at spiral pad design and on bottom right the same spiral pad but with smaller collection pad for the FE electronics.
The study of these four designs in a single readout board will allow us to perform a one-to-one comparison of the impact of the pad design both on the capacitance noise and cross talk performances to optimize the the signal to noise ratio which is a crucial parameter for achieving the requirements in term of spatial resolution and detector efficiency. In the second step of the study, we plan to propagate the select optimized pad pattern to the other *charge transfer layers* and perform a more comprehensive study of the overall impact

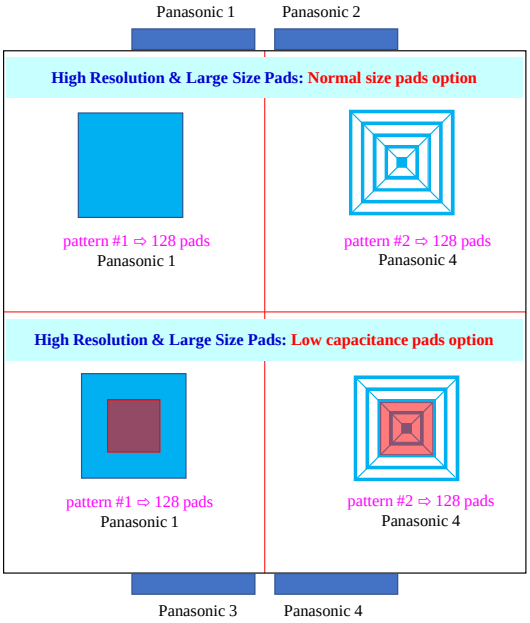

Figure 65: Sketch of a large-pad capacitive-coupling readout board with 4 quadrants, each with a different pad design to study the capacitance noise and cross talk effect.

on noise and cross talk improvement but also more importantly to help reducing the material thickness of the readout board.